

Final Technical Report

Project Title: “Technology Enabling Ultra High Concentration Multi-Junction Cells”

Project Period: (09/01/11 – 12/31/2015)

Reporting Period: (09/01/11 – 12/31/15)

Reporting Frequency: Final

Submission Date: (03/30/16)

Recipient: North Carolina State University

Recipient DUNS #: 042092122

Address: 2701 Sullivan Drive
Admin. Services III, Box 7514
Raleigh, NC 27695-7514

Website (if available) www.ncsu.edu

Award Number: DE-EE0005403

Awarding Agency: DOE EERE SETP CSP subprogram

Working Partners: Spectrolab Inc

Cost-Sharing Partners: North Carolina State University
Spectrolab Inc

Principal Investigator: S. M. Bedair
Professor
Phone: (919) 515-5204
Fax: (919) 515-5523
Email: bedair@ncsu.edu

**Submitted by:
(if other than PI)** Peter Colter
Research Assistant Professor
Phone: 919-515-4680
Email: pccolter@ncsu.edu

DOE Contracting Officer: Angela Crooks

DOE Project Manager: Daniel Stricker

Signature

Date

Project Objective: The project goal is to enable multijunction cells to operate at greater than 2000x suns intensity with efficiency above forty percent. To achieve this goal the recipients have developed a robust high-bandgap tunnel junction, reduce series resistance, and integrated a practical heat dissipation scheme.

Project Overview

A. Project background

The recipient proposed a research program to reduce the cost of solar modules by using high solar concentration (>2000x suns) and high efficiency multijunction solar cells (MJC). High concentration allows for the system cost reduction by reduction of solar cell area (the expensive part of the system) by optical components (lower cost). However, MJCs used at concentrations >2000x suns suffer lower efficiency due to several factors such as series resistance, tunnel junction performance, heat generation, and other factors. Such loss of efficiency may nullify the benefits gained from the adoption of high concentration.

The recipient has addressed these issues and offers solutions to achieve efficiencies at >2000x suns close to the peak efficiency of the MJC at low solar concentrations. Lack of reliable high-bandgap tunnel junctions suitable for 2000x has been a serious obstacle to a move to 2000x concentration operation. The recipient has taken a broader scientific approach to this problem, which has usually been addressed by empirical methods. Specifically, the recipient has addressed the contributions of both band-to-band tunneling and deep impurity levels that generate excess current. The presence of deep levels and their control adds to the robustness of the tunnel junction as-grown and annealed at high temperatures. The series resistance has been reduced by roughly a factor of two for the transition from 1000x to 2000x operation. The main contributors to series resistance include the 1) metallization type, 2) contact resistance of the metal to semiconductor interface, and the 3) top layer's conductivity. The recipient has worked to systematically address these issues. The main reduction was accomplished by reducing the emitter contact resistance and redesigning the grid and emitter structures. These metrics are listed in table 1, below, with associated targets.

B. Project scope

The project responds to the program announcement from the US Department of Energy Golden field office to address the Foundational Program to Advance Cell Efficiency (FPACE). The recipient will address fundamental issues such as series resistance, non-linear behavior in the MJC and heat generation, which limit the efficiency of multijunction solar cells at very high solar concentrations. This proposal does not deal with the design and performance of the optical concentrators; the recipient and only addresses the solar

cell components. The improved solar efficiency at high solar concentrations is believed to be the most effective way to reduce the cost of a PV system.

C. Objectives

The project goal is to achieve multijunction cells operating at greater than 2000x suns intensity with efficiency above forty percent. To achieve this goal the recipient will develop a robust high-bandgap tunnel junction, reduce series resistance, and integrate a practical heat dissipation scheme.

The main metrics the recipient has addressed in achieving this objective are given in table #1, below. The baseline values are those the recipient expects to achieve early in the program using existing technologies.

Table 1: Project Primary Metrics

Metric in the same lab	Physical Specimen Description	Current State of the Art	Baseline Value	Target Value
High bandgap, Tunnel peak current	Test Structure with cell equivalent temperature budget	45 A/cm ² (lower bandgap)	15A/cm ² (high bandgap)	50A/cm ² (high bandgap)
Tunnel junction, Specific Resistivity	Test Structure with cell equivalent temperature budget	2.0×10 ⁻³ Ω·cm ² (lower bandgap)	4.6×10 ⁻³ Ω·cm ² (high bandgap)	2.0×10 ⁻³ Ω·cm ² (high bandgap)
Emitter sheet resistivity	Top cell test structure	350 Ω/□	350 Ω/□	250 Ω/□
Front n-type contact resistance	Top cell test structure	10 ⁻⁴ Ω cm ²	10 ⁻⁴ Ω cm ²	10 ⁻⁵ Ω cm ²

The detailed project management plan to achieve these objectives is shown on the following page and a detailed discussion of the implementation and results follows

Task	Sub-Task	Part of Contact (POC)	Criteria	Tool/Method of Measurement	Milestone/Go/No Go/Metric	Demonstration	Month												Task Dates		Milestone or Go/No-Go Dates		Progress Notes								
							Q1	Q2	Q3	Q4	Q5	Q6	Q7	Q8	Q9	Q10	Q11	Q12	Planned	Actual	Planned	Actual									
Phase I																															
1	1.1	Salah Beddar (9/19/15-5/204)	Growth of heavily doped n+ and p+ films	MOCCVD growth, Hall Measurement	Milestone 1: n-type Carrier concentration - 1E9/cm3 Milestone 2: p-type Carrier concentration > 1E9/cm3 Milestone 3: Unannealed Tunneling current > 30 A/cm2 Milestone 4: Annealed Tunneling current > 10 A/cm2	Document	X	X	X	X												01/01/12	12/31/12	01/01/12	08/31/12	03/31/12	Milestone 1&2 have been completed.				
							X	X	X	X															04/01/12	06/30/13	10/15/12	06/30/13	04/30/13	milestone 3&4 achieved	
							X	X	X	X																01/01/12	06/30/13	01/01/12		11/30/12	See part one of this continuation report
							X	X	X	X																07/01/12	06/30/13			04/30/13	Go conditions achieved
2	2.1	Salah Beddar (9/19/15-5/204)	Sheet resistance, top cell	I-V, optimize thickness and doping	Milestone 6: Emitter Sheet Resistance ~ 325 Ω/sq Milestone 7: Front Contact Resistance ~ 7E-5 Ω-cm2 Milestone 8: Temperature Res ~ 20C for 1500x suns Milestone 9: Tunneling Model for > 60 A/cm2	Document	X	X	X	X												07/01/12	06/30/13				Ongoing				
							X	X	X	X														04/01/12	06/30/13	04/01/12		03/01/13	Go condition achieved		
							X	X	X	X															01/01/13	06/30/13	02/01/13		04/30/13	Milestone 8 has been achieved	
							X	X	X	X															07/01/13	06/30/14	07/01/13		04/01/13	Milestone 9 achieved. Further development ongoing.	
Phase II																															
3	3.1	Salah Beddar (9/19/15-5/204)	Heat Dissipation	Junction temperature measurement at high concentration	Milestone 10: TJ ~ 40 A/cm2 Milestone 11: TJ for Res ~ 15C for 2000x suns, non-uniform	Document	X	X													01/01/13	06/30/13									
							X	X															07/01/13	06/30/14	07/01/13		04/01/13	Milestones 10&11 met. Further development ongoing.			
							X	X																	07/01/13	12/31/14	11/31/13		03/31/14	Milestone 12 has been achieved	
							X	X																	07/01/13	03/31/14	06/30/14		03/31/13	Milestone 13 has been achieved	
4	4.1	Salah Beddar (9/19/15-5/204)	Diffusion barriers for tunnel junctions annealed	MOCCVD, SIMMS, I-V, TLM	Milestone 14: IFC ~ 0.82 Milestone 15: ITC ~ 40% Milestone 16: Temperature measurement Res ~ 15C for 2000x suns Final Milestone: Efficiency ~40% at 2000X	Document	X	X	X	X											07/01/13	12/31/14	07/01/13		05/15/14	Milestone 14 has been achieved					
							X	X	X	X													07/01/13	12/31/14	07/01/13		05/15/14	Milestone 16 achieved			
							X	X	X	X														07/01/13	12/31/14	07/01/13		05/15/14	Milestone 16 achieved		
5	5.1	Salah Beddar (9/19/15-5/204)	Sheet resistance, top cell	I-V, optimize thickness and doping	Milestone 12: Sheet Resistance ~ 250 Ω/sq	Document	X	X	X	X										07/01/13	12/31/14	11/31/13		03/31/14	Milestone 12 has been achieved						
							X	X	X	X													07/01/13	03/31/14	06/30/14		03/31/13	Milestone 13 has been achieved			
							X	X	X	X														07/01/13	12/31/14	08/15/14		11/15/14	Milestone 14 has been achieved		
6	6.1	Salah Beddar (9/19/15-5/204)	Heat Dissipation	Junction temperature measurement	Milestone 16: Temperature measurement Res ~ 15C for 2000x suns Final Milestone: Efficiency ~40% at 2000X	Document	X	X	X	X										07/01/13	12/31/14	07/01/13		05/15/14	Milestone 16 achieved						
							X	X	X	X													07/01/13	12/31/14	08/15/14		05/15/14	Milestone 16 achieved			
7	7.1	Salah Beddar (9/19/15-5/204)	MJC structure for 2000X	MJC structure for 2000X	Final Milestone: Efficiency ~40% at 2000X	Document & Sample														01/01/14	12/31/14	08/15/14									

Report: Discussion Breakdown:

1. Carbon doping task 1.1.
2. Tellurium doping task 1.2.
3. Work at Spectrolab tasks 2&5&7
4. Tunnel Junction Modeling tasks 1.3 & 4.1
5. Heat dissipation tasks 3&6
6. Tunnel junction fabrication and testing at NCSU tasks 1.2 & 4.2
7. Summary & Attachments

Section 1 Carbon doping

Carbon was the obvious choice for the p-type dopant for the tunnel junctions; it is known to have the lowest diffusion coefficient of the common p-type dopants and can be incorporated into GaAs and AlGaAs at high concentrations. Thus the task for this program was not to break new ground in this aspect of the project, but to incorporate a well developed aspect of existing technology into our process.

The selected carbon source, CBr₄ was procured. This was selected since it is not subject to the controls (for environmental reasons) that the commonly used CCl₄ is.

Modifications to MOCVD system were made including changing mass flow controller, pressure controller, and chiller; these enabled achieving p-type concentrations ranging ~10¹⁷ - 10¹⁹ /cm³. This doping range was achieved by varying the CBr₄ flow rate, bubbler temperature, V-III ratio and growth Temperature.

The newly installed Cbr₄ source was first calibrated for doping GaAs. The temperature and pressure of the bubbler were varied to find conditions under which the installed flow controller (200 sccm) and pressure controller (rated for 100 sccm) would be within their ranges while providing the desired doping levels of 10¹⁷ to 10¹⁸ /cm³ in GaAs. The other growth conditions were those typical for GaAs growth (640° C), the relation between the carrier concentration and the CBr₄ flow (expressed as sccm CBr₄ excluding carrier gas) is shown in figure 1-1.

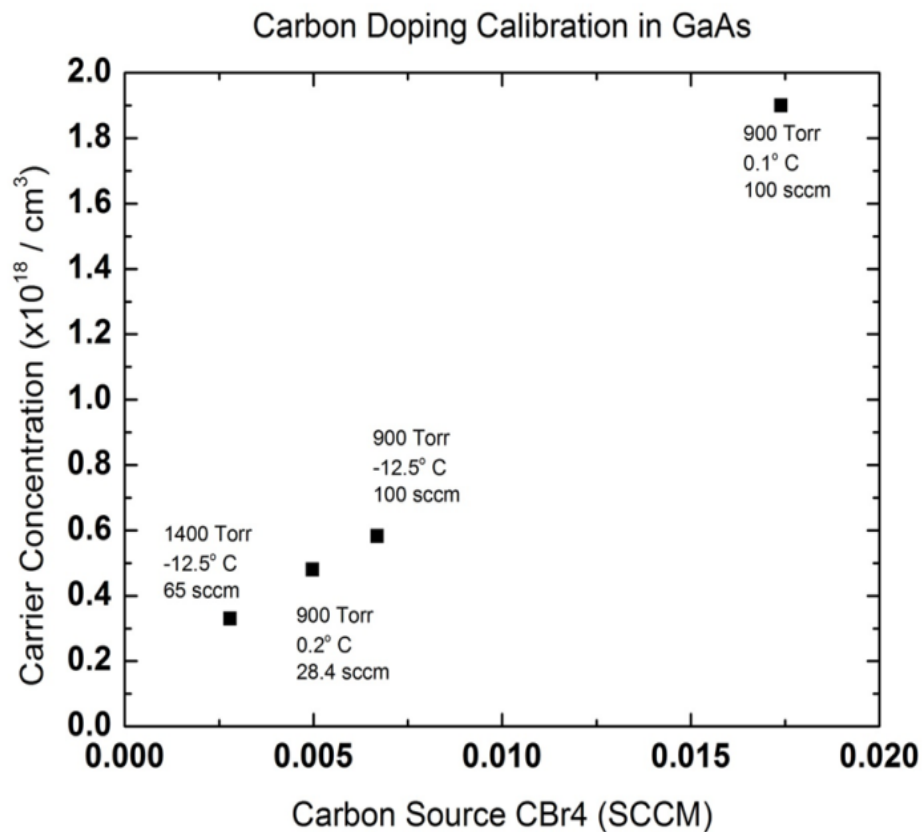


Figure 1-1: Carbon doping calibration plot for GaAs

Upon completion of the GaAs doping calibration, we began calibration of the AlGaAs doping for the tunnel junction structure. The AlGaAs was 54% Al and the growth temperature was 600°C chosen as a starting point for the tunnel junction growth; this is growth temperature was chosen to minimize impacts of the volatile behavior of the Te dopant planned for use in the InGaP layer. A high flow rate of CBr₄ (0.101 sccm CBr₄) was set and the V-III ratio was varied to find the maximum doping that would give acceptable morphology. The results are shown in figure 1-5.

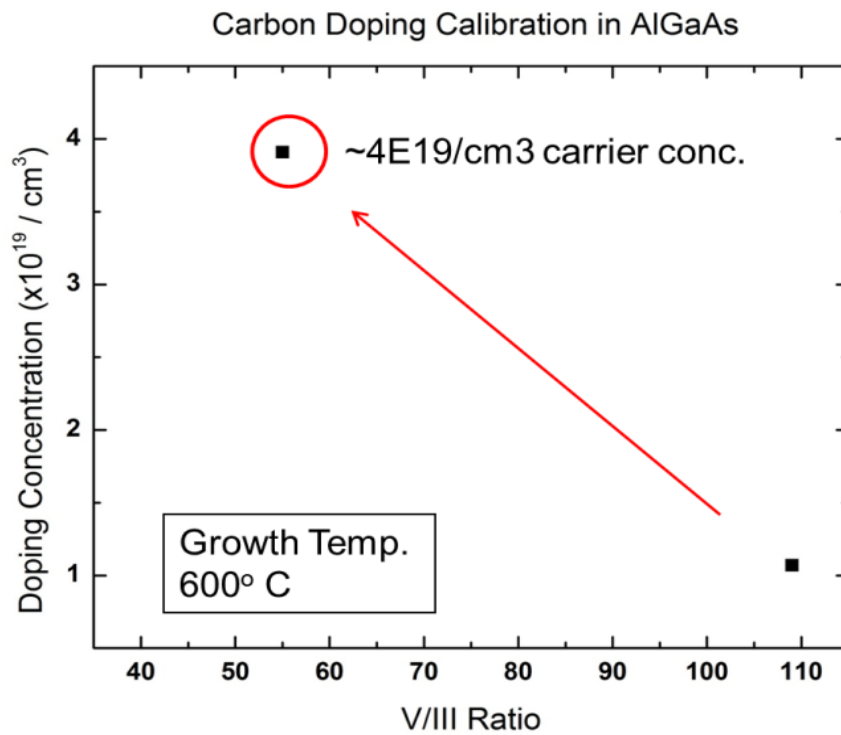


Figure 1 -2: Carbon doping calibration plot for AlGaAs (AlAs ~54%)

The $4 \times 10^{19} / \text{cm}^3$ carrier concentration achieved exceeds that specified by **Milestone #2: AlGaAs (AlAs~30%) with p-type doping concentration $> 10^{19} / \text{cm}^3$ (by month 10)**

While the tellurium source for n-type doping was being installed we conducted a more extensive study of the carbon doping characteristics of aluminum gallium arsenide in order to optimize the doping for tunnel junctions. Starting with the conditions which had given $4 \times 10^{19} \text{ cm}^{-3}$ we varied the growth temperature from 675°C to 560°C . These growths used a test structure consisting of a 0.4μ layer of undoped aluminum gallium arsenide, a 0.4μ layer of carbon doped aluminum gallium arsenide and a 0.2μ gallium arsenide cap layer which were grown on semi-insulating substrates.

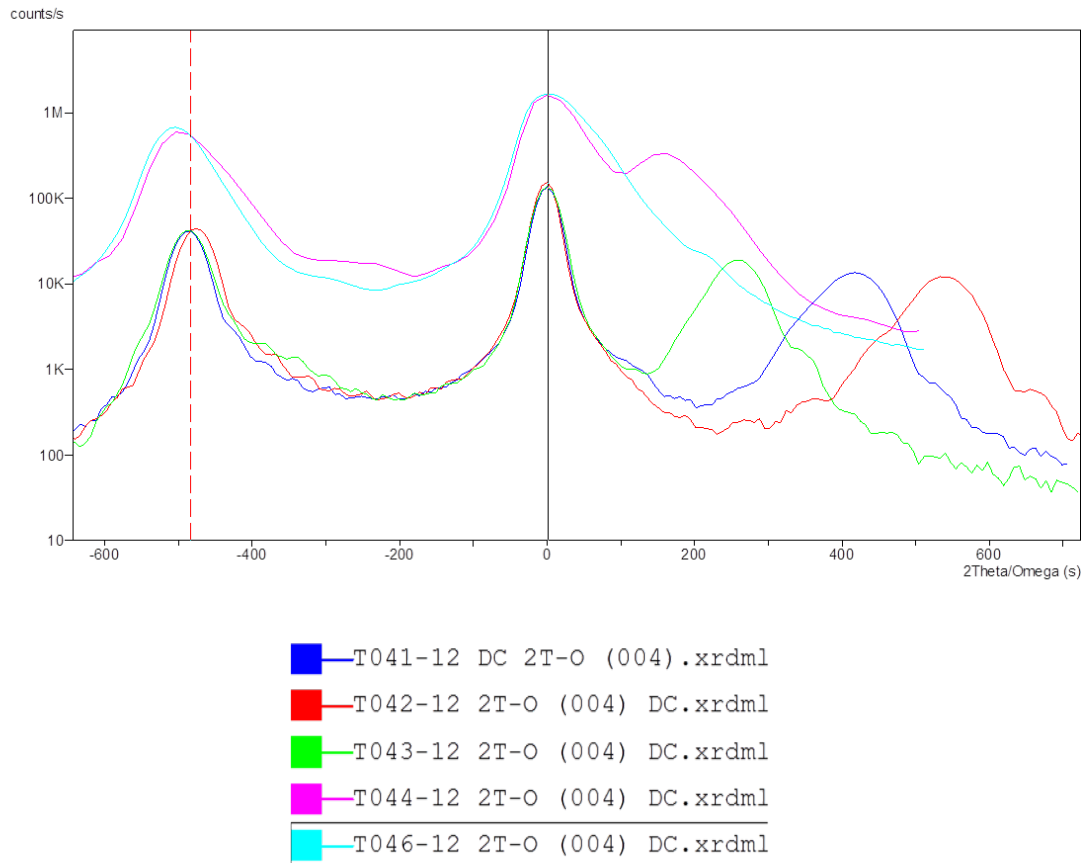


Figure 1-3: Carbon doping XRD data for AlGaAs (AIAs ~54%)

The structure allowed both the measurement of carrier concentration by Hall measurements and determination of the aluminum concentration and atomic carbon concentration by high-resolution x-ray diffraction measurements. X-ray diffraction is suitable for the measurement of the atomic carbon concentration since the carbon is on the arsenic site and has a shorter bond length which produces lattice contraction; the effect is well known in gallium arsenide and methods of compensating for it in highly doped HBT bases by the introduction of indium or antimony has been patented. The strain produced by 10^{20} cm^{-3} doping is equal and opposite to that produced by 2% indium. Figure 1-3 shows the high-resolution x-ray diffraction scans [004] of the aluminum gallium arsenide test

structures. The relation between the [004] scan and the [224] scans (not shown) show that the structures have not relaxed. Figure 1-4 shows both carbon concentration and hole concentration versus temperature for the aluminum gallium arsenide test structures.

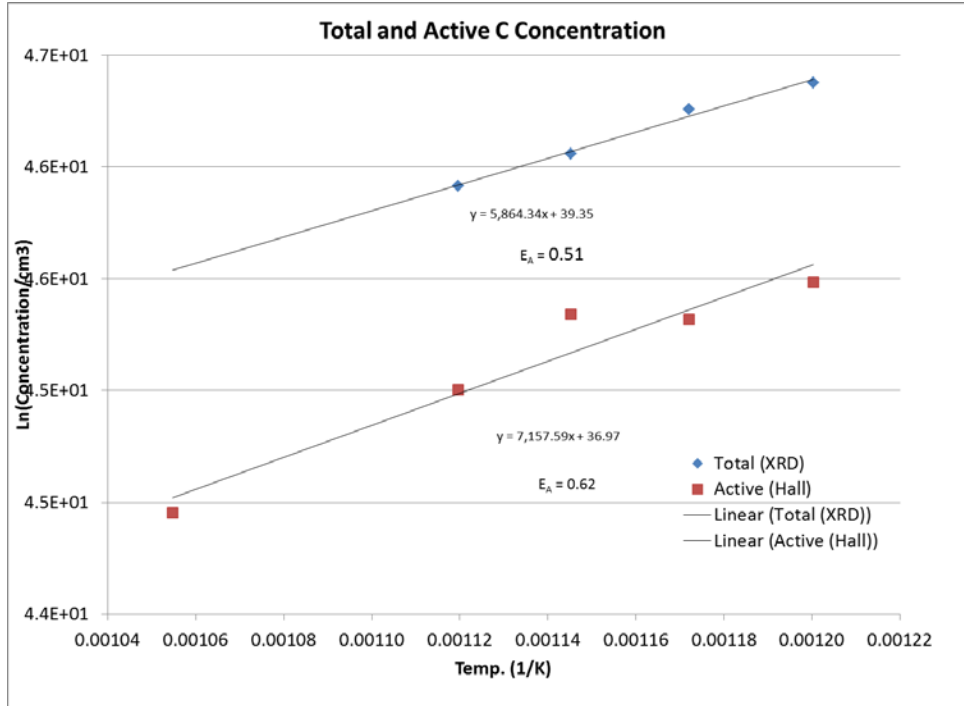


Figure 1-4: C- doping calibration linear plot for AlGaAs (AlAs ~54%)

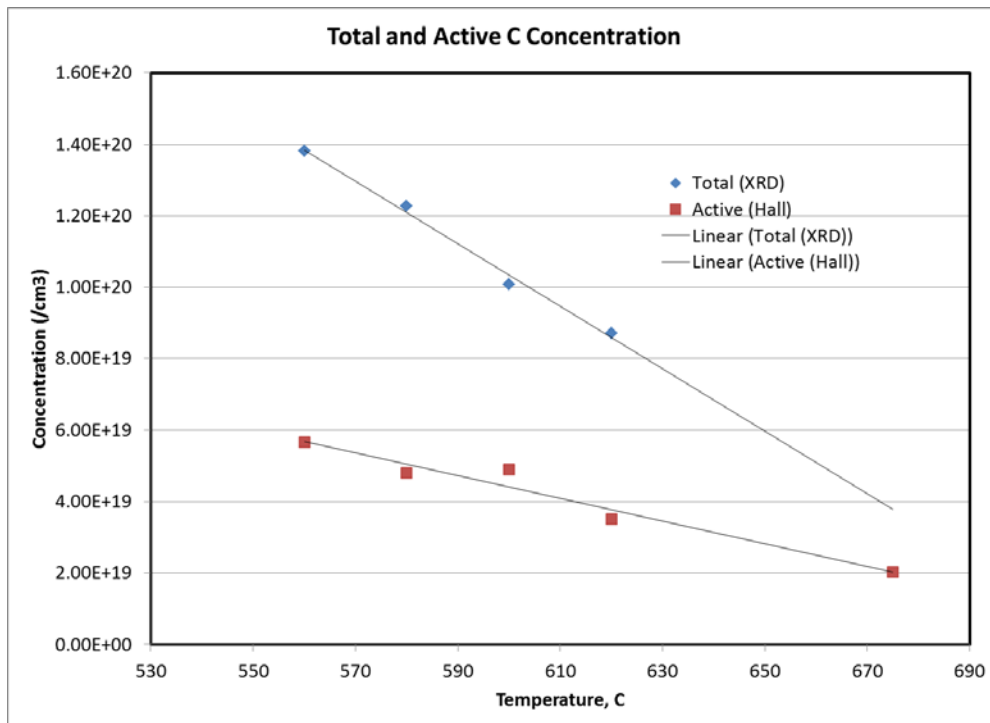


Figure 1-5: Carbon doping calibration plot for activation energy

The hole concentration is highest for the low temperature samples; however, the activation of the carbon is not quite as high with the low temperature structures. The higher concentration at low temperature shows that the desorption of carbon containing species from the surface of the growing sample is the limiting step rather than the decomposition of the carbon tetrabromide which apparently satisfactorily decomposes at all temperatures. Figure 1-5 shows the same data as in figure 4 but plotted as log concentrations versus reciprocal temperature; this allows determination of an effective activation energy for hole concentration and carbon. It does not show as great an activation energy as that reported elsewhere [1], but the other investigators used AsH_3 rather than the TBA arsenic source that we use

In order to get the maximum effective carrier concentration in the junction we explored increasing the carrier concentration on the p-side of the junction. The approach we took in this case was to see if we could find a way to cut the difference between the metallurgical carbon content is measured by XRD and carrier concentration measured by Hall effect on test samples.

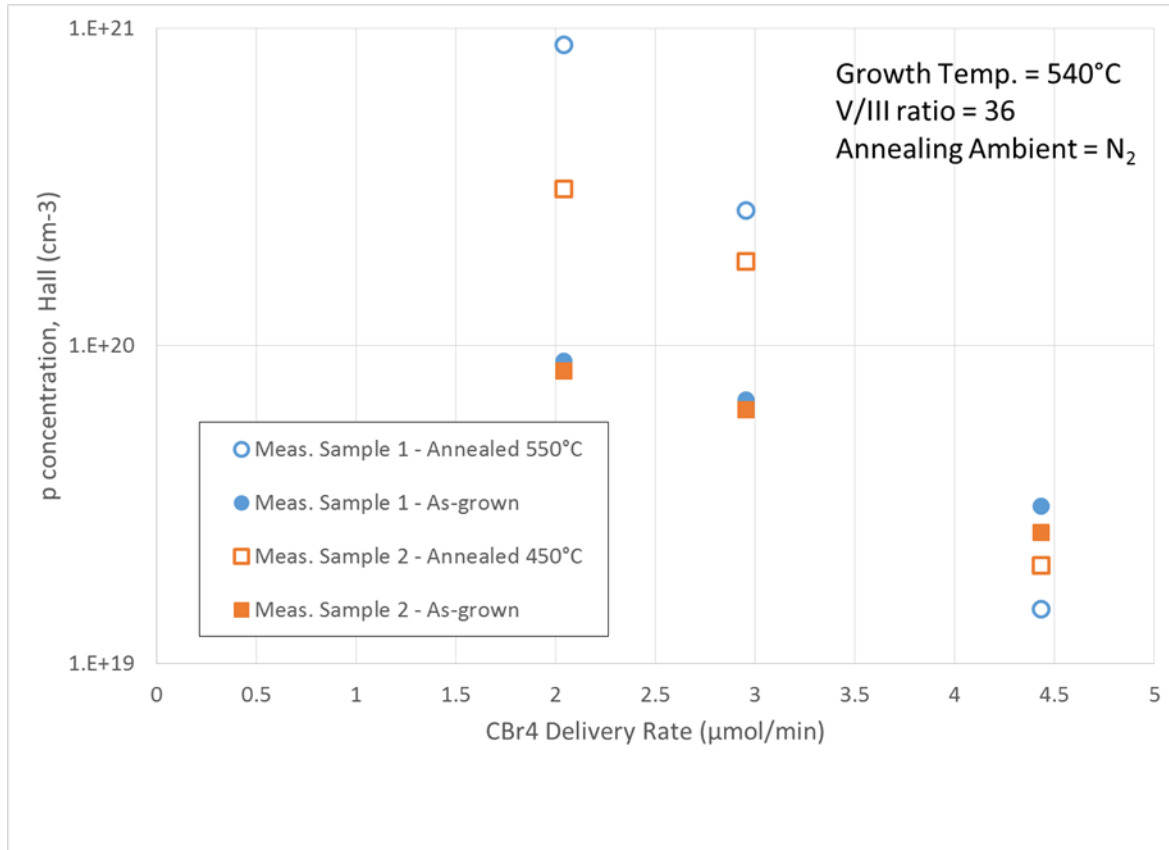


Figure 1-1: Hall concentration of p-type dopants in AlGaAs as a function of CBr₄ flow for samples annealed at 450 and 550 °C.

We concluded that one possible reason for the discrepancy was passivation by hydrogen at the relatively low growth temperatures, we decided that one approach to this problem would be to anneal the junction under such conditions that the hydrogen would escape. This was done by heating the just grown junction to a higher temperature immediately after growth of highly doped AlGaAs layer before the gallium arsenide cap was grown. The results of these experiments are seen in figure 1-5. This insight allows the growth procedure for a complete multijunction cell to be adjusted to take advantage of this phenomena.

Section 2 Tellurium Doping

Installation of Te doping manifold The inability to obtain a dilute gas source of tellurium made necessary the installation: manifold for a bubbler. The typical gas source of tellurium up to 200 sccm per minute at 5 ppm concentration thus needed to be duplicated by a liquid source. The lowest reasonable flow rate was felt to be 10 sccm which would imply a necessary concentration of about 100 ppm. With a typical bubbler pressure of 1000 torr this would imply a vapor pressure of about 0.1 torr is required. If diethyl telluride is used as a source this would imply a bubbler temperature of -40°C . The typical chilling baths used in metal-organic growth systems will reach a minimum temperature of -25°C . However baths are available which are rated from -40°C (a Neslab RTE 140 was obtained). A possible alternative would have been the construction of a dilution manifold type bubbler station. This would have the advantage of allowing a wider range of dopant fluxes, typically range of at least 1000 rather than the 50 which is available in a conventional bubbler station. However since the MOCVD reactor is equipped with a computerized control system the first consideration in installing liquid source type bubbler was compatibility with the existing computerized control system. The simple manifold utilizing a low temperature -40°C refrigerated bath is much more amenable to utilizing the existing computer-controlled control lines originally set up for gas source. Uses of a dilution manifold would have required the mixing of manual and computer-controlled components which has safety implications or considerable reworking of the control system.

An existing gas source consisting of a mass flow controller with control line and a single pneumatic control line controlling a pair of normally open and normally closed valves directing either nitrogen or reactant gas to the manifold, (this is shown in figure 1 upper) was converted to feed the manifold. The modified set up for use with the bubbler source is shown in figure 1 (lower). The control lines for the mass flow controller and the vent-run manifold are retained. The normally open isolation valve is retained and an additional normally open isolation valve was installed between the bubbler manifold and the newly installed pressure controller. This isolation valve is connected to the same control airline as the original isolation valve. The control air-line, which was originally connected to the pair of valves which sent a reagent gas for nitrogen into the system, was reconnected to a normally closed valve on each of the bubbler connections and a normally open valve bypassing these connections. This allows the same type of valve switching as in the bubbler manifolds originally in the system. While the original bubbler manifolds have independent control of the bypass valve, it is only used during maintenance procedures, particularly for leak-checking. In the new bubbler station we have used three manual valves to provide a somewhat more flexible leak-checking system than is available on the original manifolds. The new chiller and bubbler manifold are installed in a gas cabinet connected to the back of the system. This was necessary since there was no more room in the existing gas manifold cabinet. The new manifold assembly is constructed with the same

metal sealed fittings (VCR) and orbital welded stainless steel tubing as the rest of the system.

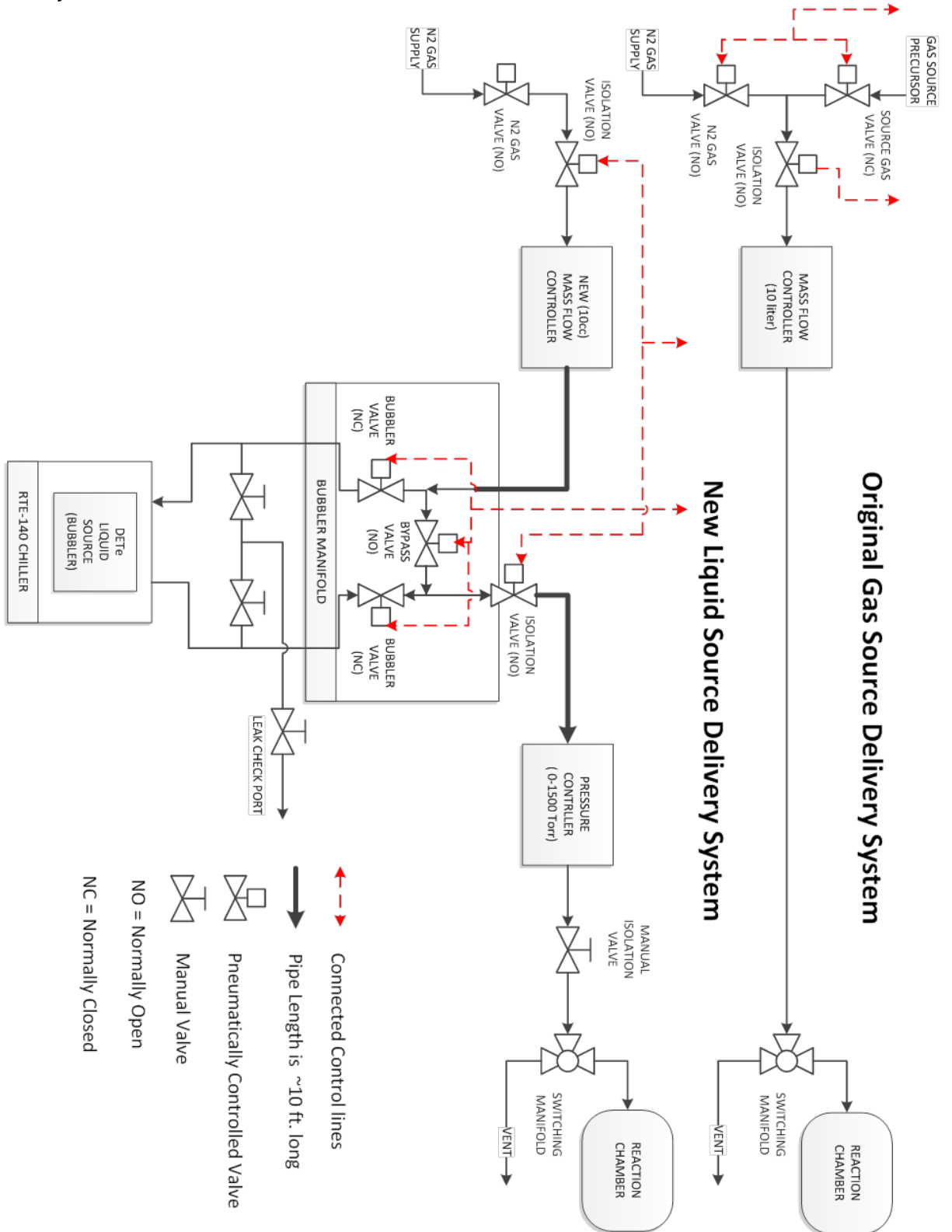


Figure 2-1: Tellurium doping manifold

Milestone #1: n-type InGaP and/or GaAs $\sim 1 \times 10^{19} / \text{cm}^3$ (by month 4). Status: Completed. The completion had been delayed as a result of unavailability of source material in gas form. After the Te liquid source manifold was installed we achieved a carrier concentration of 1.5×10^{19} in InGaP at a growth temperature of 580°C (nominal) with a V/III ratio 40. **Thus Milestone 1 is completed** Optimization of highly-doped InGaP and GaAs, preliminary to fabrication of tunnel junction test structures is continued.

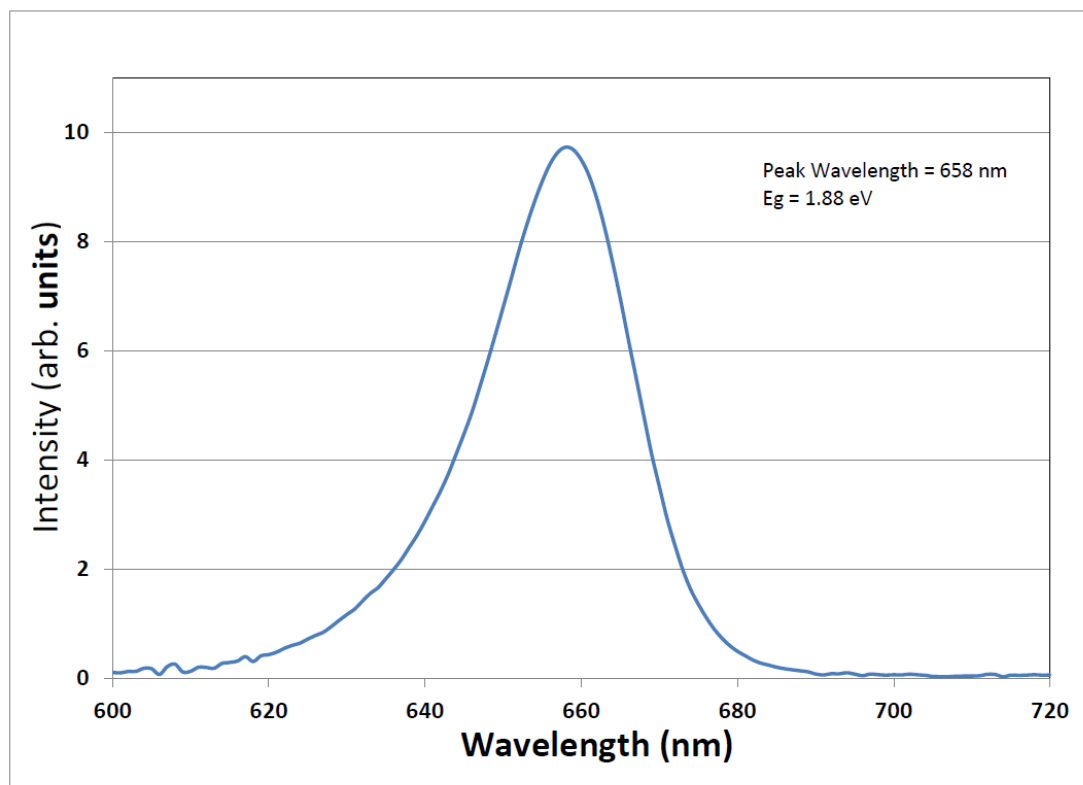


Figure 2-2: Photoluminescence spectrum of InGaP measured at NCSU

In order to improve the evaluation of material quality we set-up a photoluminescence apparatus with an inexpensive solid-state laser ($\sim 100\text{mW}$ at 532nm); this allowed materials with bandgaps in the $1\text{-}2.5\text{ eV}$ range to be effectively measured. It was found desirable to reduce recombination at the surfaces of InGaP samples by slightly lowering the In composition of the last 10nm or so. Figure 2-2 shows the photoluminescence signal of such an InGaP sample.

Impact of Tellurium doping in InGaP on tunnel junction J-V

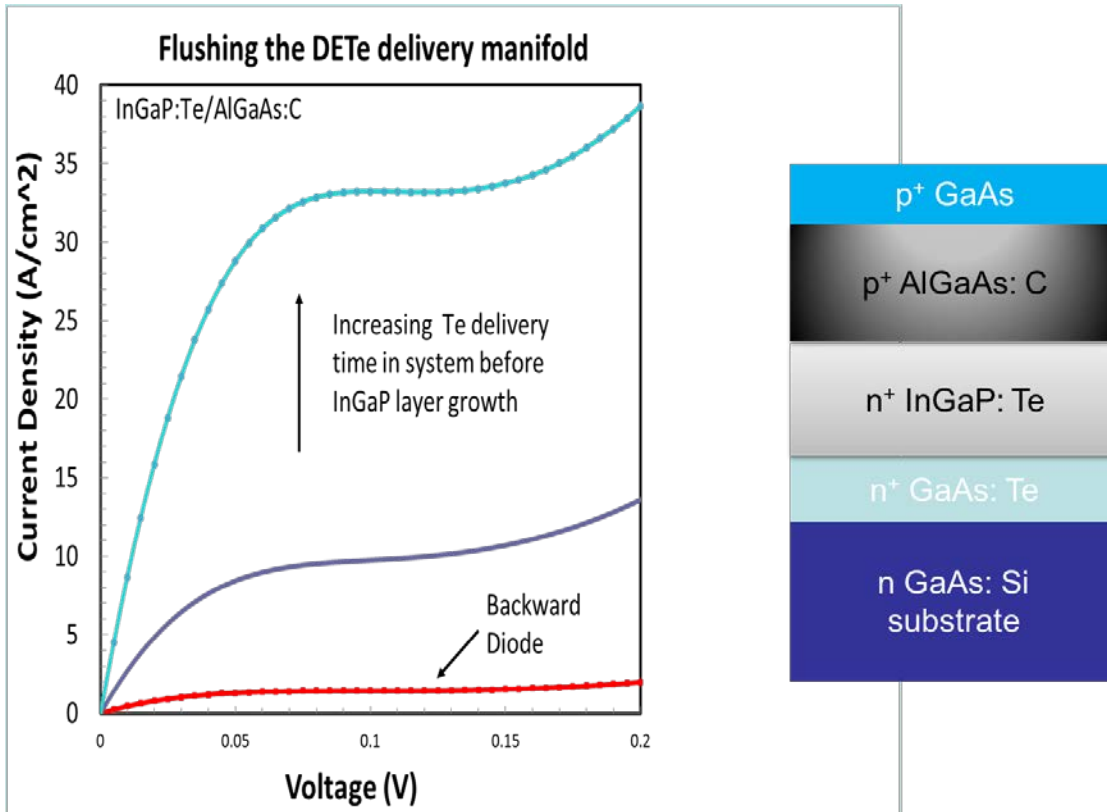


Figure2-3: Impact of Te source pre-flow time on tunnel junction J-V characteristic.

Details of the tellurium (Te) doping procedure in crystal growth have been found to significantly impact tunnel junction characteristics. Shown in Figure 2-3, tunneling current density is proportional to the length of time for flushing Te through the delivery manifold prior to growth of the Te doped indium gallium phosphide (InGaP) layer. This feature may be caused in part by the custom design of our laboratory growth system. Notably, the Te source “bubbler” and delivery manifold components, added for expanded capacity to our reactor, are externally located. This configuration has a longer delivery line, and when combined with a relatively low molar flow rate required for the Te source, sets a finite time to fully reach steady state delivery conditions. For ensuring consistency, growth procedures include sufficient pre-flowing (more than three line-volume exchanges) of the Te source through the delivery lines at the beginning of each process run.

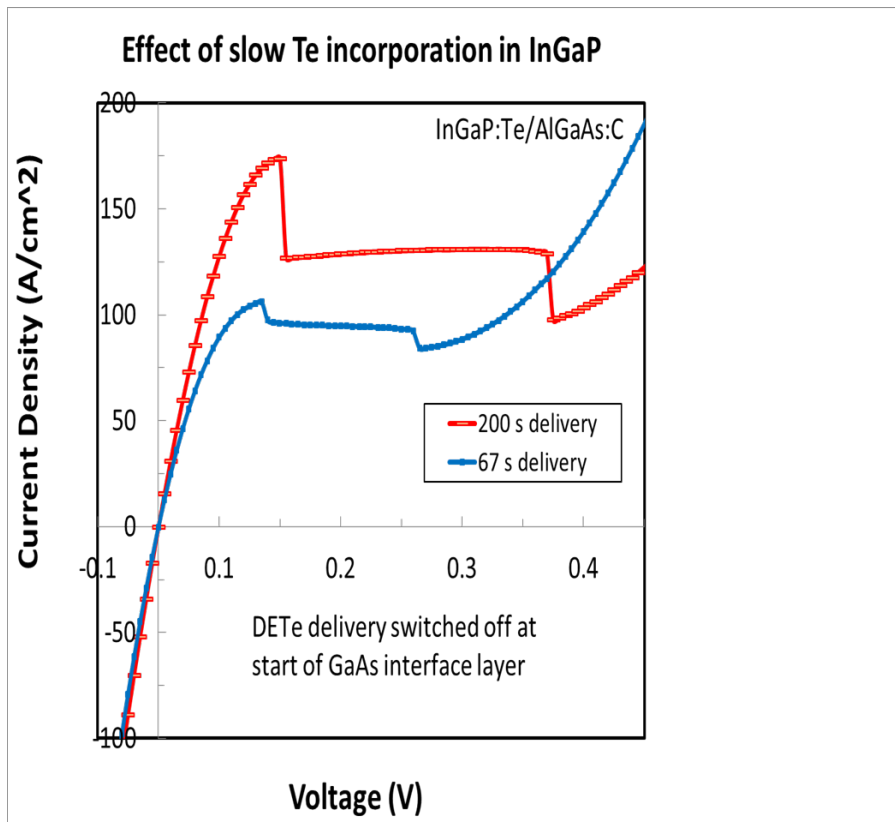


Figure 2-4: Impact of slow Te incorporation in InGaP.

While the flush time may be a peculiarity of the system there are other unique features in the Te doping of InGaP. For a given, consistent Te flow rate, there appears to be a time delay before achieving a full doping level in InGaP layers. This characteristic is distinct from the previously discussed effects for pre-flushing times of Te source into the system. In figure 2-4, the current density is plotted as a function of voltage for tunnel junction devices grown with different Te delivery times in the InGaP layer. For the 200 second delivery time sample, higher tunneling current density indicates a higher effective doping level at the junction. Note that the total time that Te flows into the system is identical for both samples; in the case of 67 second delivery sample, 133 seconds of doped gallium arsenide growth was added prior to growth of the InGaP layer. It thus appears that there is a surface segregation of Te in the growth of InGaP which is not present in the case of the growth of gallium arsenide.

Unique Tellurium behavior in InGaP material system

While most dopants either incorporate quickly upon absorption on the crystal surface or are quickly desorbed, there is a possibility that Te atoms also get attached to the step edges. This allows Te to remain at the surface after shutting the source off, thus providing the basis for a “Te Memory Effect.” The phenomena is illustrated in Figures 8a and 8b.

Figure 2-5a. Typical dopants (i.e. Si, Zn) either

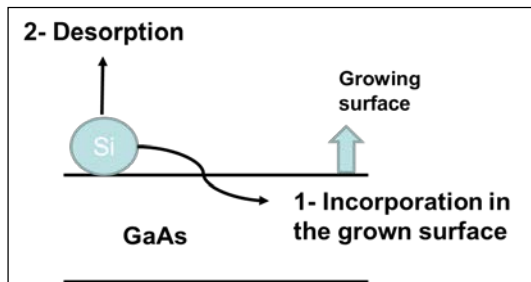
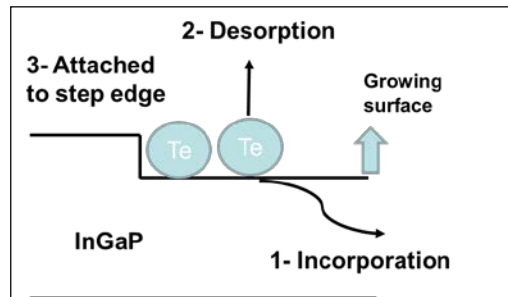


Figure 2-5b. Te in InGaP can be



are either 1) incorporated or 2) desorbed.

1) incorporated, 2) desorbed, or

3) attached to a step edge.

Considering the case of an abrupt ternary-ternary junction (Figure 2-5). Te atoms present at the step edges, after growing the (n+)InGaP layer, can lead to Te incorporation into the subsequently grown carbon doped (p+)AlGaAs layer. This leads to compensation of the C-doping ($N_A - N_D$) level resulting in a poor tunnel junction.

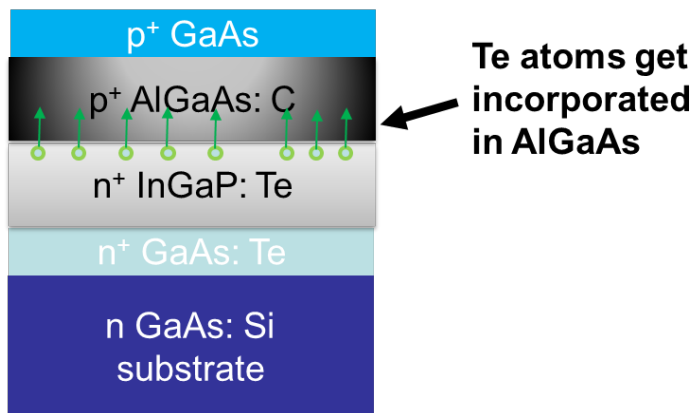


Figure 2-6: Impact of Te memory effect on tunnel junction

Some research groups are currently using an n+-GaAs/p+-AlGaAs binary-ternary tunnel junction to avoid the InGaP:Te memory effect (figure 2-6). In Figure 2-7, the J-V characteristic is shown for an NCSU (n+)GaAs/(p+)AlGaAs binary-ternary tunnel junction device. Peak tunneling current density was beyond NCSU’s measurement capability, and specific series resistance was $1 \times 10^{-4} \Omega\text{-cm}^2$. This excellent J-V performance

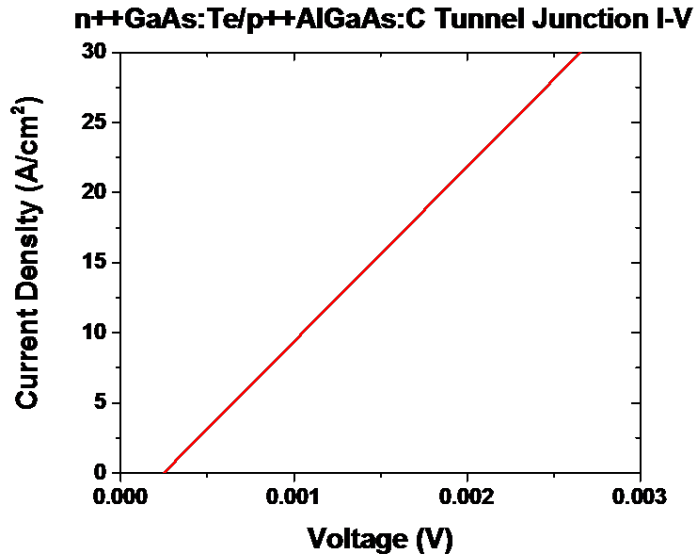


Figure 2-7: J-V characteristic of NCSU GaAs (n+)/AlGaAs (p+) tunnel junction

demonstrates lack of adverse conditions such as Te memory effects. However, using the binary-ternary approach can lead to a decrease in multijunction cell efficiency by 1-2% due to the optical absorption in the tunnel junction GaAs layer.

A further discussion of the effects of Tellurium surface accumulation is considered in the section on tunnel junction fabrication since is important in transient behavior at the interfaces in the tunnel junction structure.

Section 3 Spectrolab Project Objective:

The project is aimed at reducing the \$/W cost of the Multi Junction Solar Cell (MJC) by a factor of two from the reported state-of-the-art by enabling their operation at higher solar concentration. The project goal is to achieve multi junction cells operating at greater than 2000x suns intensity with efficiency above forty percent. To achieve this goal the recipient will develop a robust high-bandgap tunnel junction, reduce series resistance, and integrate a practical heat dissipation scheme.

The main metrics Spectrolab will address in achieving this objective are given in table #1, below. The baseline values are those we expect to achieve early in the program using existing technologies.

Project background

NCSU and Spectrolab proposed a research program to reduce the cost of solar modules by using high solar concentration (>2000x suns) and high efficiency multijunction solar cells (MJC). High concentration allows for the system cost reduction by replacement of solar cell area (the expensive part of the system) by optical components (lower cost). However, MJCs used at concentrations >2000x suns suffer lower efficiency due to several factors, series resistance, tunnel junction performance, heat generation, and other factors. Such loss of efficiency may nullify the benefits gained from the adoption of high concentration.

The research team has addressed these issues and offers solutions to achieve efficiencies at >2000x suns close to the peak efficiency of the MJC at low solar concentrations.

Project title: Technology Enabling Ultra High Concentration Multi-junction cells

Recipient: North Carolina State University

Lack of reliable high-bandgap tunnel junctions suitable for 2000 \times has been a serious obstacle to a move to 2000 \times concentration operation. The recipient will be taking a broader scientific approach to this problem, which has usually been addressed by empirical methods. Specifically, the research team will address the contributions of both band-to-band tunneling and deep impurity levels that generate excess current. The presence of deep levels and their control will add to the robustness of the tunnel junction as-grown and annealed at high temperatures. The series resistance needs to be reduced by roughly a factor of two to transition from 1000 \times to 2000 \times operation. The main contributors to series resistance include the 1) metallization type, 2) contact resistance of the metal to semiconductor interface, and the 3) top layer's conductivity. The research team is systematically addressing these issues. The main reduction will be accomplished by reducing the emitter contact resistance and redesigning the grid and emitter structures. These metrics are listed in table 1 with associated targets.

Table 1: Project Primary Metrics for Spectrolab First Period

Metric in the same	Physical Specimen	Current State of the	Baseline Value	Target Value
Emitter R_{sheet}	Top cell test structure	350 Ω/\square	350 Ω/\square	250 Ω/\square
Front n-type R_{contact}	Top cell test structure	$10^{-4} \Omega \cdot \text{cm}^2$	$10^{-4} \Omega \cdot \text{cm}^2$	$10^{-5} \Omega \cdot \text{cm}^2$

Front Side Contact - Round #1 Matrix

Based on initial literature review, two front metal designs were chosen. Many of the metallizations reported in the literature were intended for a cap structure that is lower in doping than standard multijunction solar cell structures for concentration photovoltaic (CPV) applications. An initial metallization plan was developed to establish baseline specific contact resistivity measurements for a control and experimental front metallization structures.

Table 2 summarizes the initial front metal experiment plan (front metal round #1). The first row is a standard semiconductor with typical surface clean, metals, and sinter as a control. Rows 2-4 are variants of the control and rows 5-7 are Pd/Ge-based. The Pd/Ge-based splits have the same design but different sinter conditions. It should be noted that all the splits are capped with the same thickness of Ag as the control.

Table 2 – Summary of Front Metal Experiment #1

No.	Surface Preparation	Metalization	Sinter Condition
1	Standard	Au-based	Standard
2	Type 1	Au-based	Standard
3	Standard	Au-based with barrier	Sinter condition 1
4	Standard	Au-based with barrier	Sinter condition 2
5	Standard	Pd/Ge-based	Standard
6	Standard	Pd/Ge-based	Sinter condition 3
7	Standard	Pd/Ge-based	Sinter condition 4

Source: Spectrolab Inc.

The wafers used in the experiment were purchased from Spectrolab inventory and are CUTJ type wafers (a design that is used for concentrator cells) and are of nominal performance.

The photomask is an experimental photomask consisting of concentrator cells (~ 8 mm x 8 mm) called CDO-064 (concentrator dual ohmic). The photomask also has a number of transmission line measurement (TLM) patterns along the top, bottom, left and right edges of the wafer. There are a number of TLM design variations. One “standard” design was used for all the measurements with a secondary design used as a check.

Measurement Methodology

For the specific contact resistivity measurement, the Transfer Length Method (TLM) methodology is used (as described in D. Schroder “Semiconductor Material and Device Characterization”, Chapter 3, 2nd edition). The methodology is summarized below.

Metal pads with increasing spacing between them are deposited on the GaAs contact layer. Fig. 1 shows a basic TLM design for determining sheet resistance and contact resistance used for the majority of the measurements shown in this report. The pad dimensions are 300 μm (W) x 1900 μm (L). The spacings (S_n) between pads are nominally; 50, 80, 100, 200, 400, 600, 800, and 1000 μm . The metal pads sit upon a mesa structure of width M .

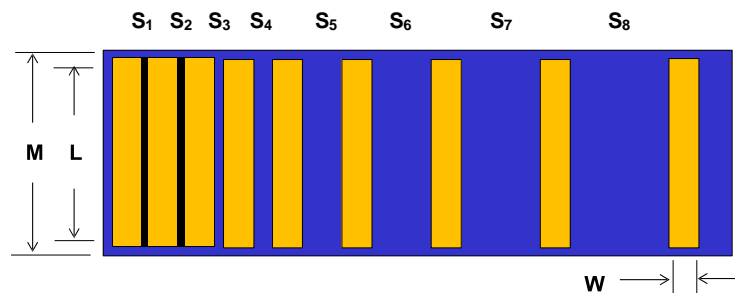


Fig. 3-1 Basic TLM design for determining sheet conductivity and contact resistance.

The resistance is measured between each adjacent pads and is used to determine sheet resistance, contact resistance and transfer length.

Graphically, the method is shown in Fig. 2, where the slope of the resistance (Ω) vs. spacing (cm) gives a value proportional to the sheet resistance (Ω/\square). Multiplying this value by the pad length (L) gives sheet resistance for the conducting layer. The y-axis intercept is equal to $2\times$ the contact resistance (of metal to semiconductor). The x-axis is equal to $2\times$ the transfer length (the fraction of the pad of width (W) of which the current transfers from the metal to the semiconductor or vice-versa. This is the methodology for which all the specific contact resistance numbers were derived from.

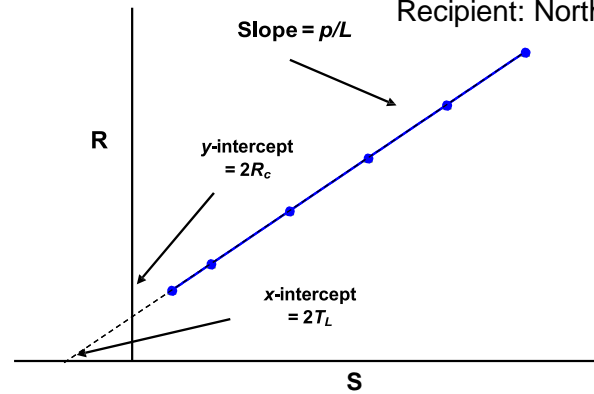


Fig. 3-2 TLM method for extracting sheet rho and contact resistance.

From the figure, the conductive layer sheet resistance (ohm/sq), the contact resistance (R_c) and the transfer length (L_T) can be extracted. The specific contact resistivity is calculated from (1),

$$\rho_c = R_c A \quad (1)$$

Where ρ_c is the specific contact resistivity (ohm-cm²), R_c is the contact resistance of metal to semiconductor (ohm), and A is the area of the contact (cm²).

The transfer length (L_T) is an important quantity as the current transfer from the metal pad to the semiconductor layer is over a small quantity of the transfer length and not the entire width (W) of the pad. Therefore the specific contact resistivity is given by;

$$\rho_c = R_c A = R_c Z T_L \quad (2)$$

Where Z is the length of the contact pad and T_L is the transfer length (cm) as determined from the TLM method shown in Fig. 2.

Preliminary results

Concentrator UTJ (CUTJ) wafers were processed on the front side using standard procedures except for the metal evaporation. Each split in Table 2 had two wafers at a minimum. The wafers had photolithographically defined gridlines and each metal split was performed separately. The photomask has both multiple TLM patterns along the periphery of the wafer along with CDO-064 sized solar cells (~0.64 cm²). The TLM patterns are used to characterize contact resistance and the cells allow subsequent electrical characterization. All the wafers had standard anti-reflective (AR) coating as well. The cells and TLM patterns were electrically isolated by saw dicing.

The resistance between two pads is measured with 4 probes ($\pm V$ & $\pm I$). In this case, the resistance was determined from a current sweep between ± 50 mA (source current) and the measured (sense) voltage. The resistance at each point of the sweep is calculated ($R = V/I$), with the zero point and the two adjacent points on each side of zero were deleted from the IV trace as zero crossing are especially noisy.

Fig. 3 shows a summary of the measured specific contact resistivity for the production (control) and six splits as outlined in Table 2. The four groupings on the left are the Au-based control, two Au-based based with additional barrier layer (to minimize

Project title: Technology Enabling Ultra High Concentration Multi-junction cells

Au diffusion), and a control with an alternate surface treatment prior to metal evap. The last three splits on the right are Ge/Pd-based metallizations at three different sintering conditions. Two of the sinter conditions are rapid thermal anneal (**RTA**) and one is a furnace sinter. The 18 month front contact metric ($1e-5 \Omega\text{-cm}^2$) is shown with the thick solid line for reference.

Four individual TLM patterns were measured across the wafer. Data was not used if too few points or the TLM pattern was not usable (due to scratch for example). The IV sweep was used to calculate an average R and a minimum and maximum R. Contact resistance (and hence specific contact resistivity values) were extracted from the data. The figures below show an average of the three to four TLM results per wafer. The max and min are the highest and lowest from each wafer and are not an average. This is done to show the range of resistivity, given the uncertainties in the measurement.

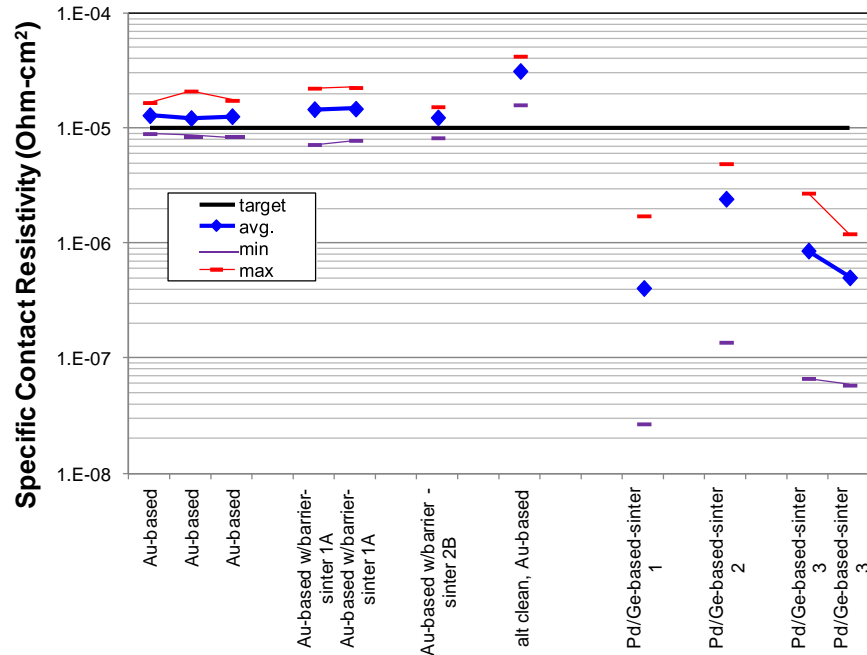


Fig. 3-3 Summary of measured specific contact resistances for front side metal with nominal pad spacings (S).

Because of the low statistics of TLM patterns on the wafer (one on the left, top, right, and bottom of the wafer), estimates of the range of fits to the TLM data were made to get a sense of the range of the specific contact resistance. The average resistance R (as determined from the IV sweep) and the minimum and maximum resistance (R) values were used to determine the range of fits.

The actual spacing between pads were measured for each TLM pattern and specific contact resistivity was recalculated. The nominal pad size is used. The measured spacings are approximate. The specific contact resistivity (with measured S) is shown in Fig. 4 vs. the same run splits as shown in Fig. 3.

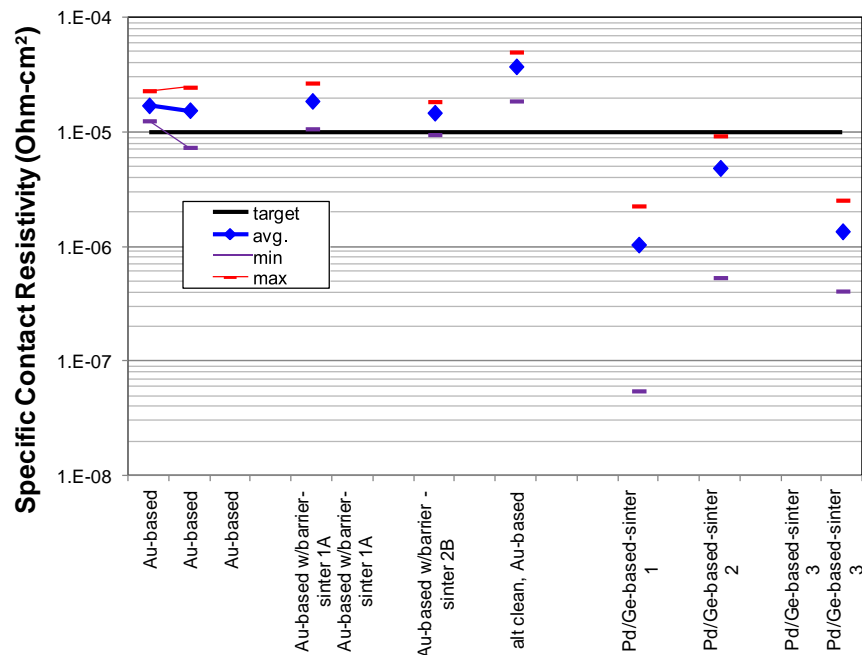


Fig. 3-4 Summary of measured specific contact resistances for front side metal with measured pad spacings (S).

As an additional check a secondary TLM pattern with different pad spacing and pad sizes were used to spot check.

Some of the wafers (at least one from each split) were then continued with processing with back metal and sintering to form completely processed cells. This report documents the TLM results, electrical results (LIV and EQE) of cell performance is to be presented at a later time.

Analysis & Discussion

In all cases of the TLM data, show results that have approximately the same order of magnitude. There are some differences that show depending on measured vs. nominal spacing and TLM design used. In all cases the Au-based metallizations and variations have specific contact resistances higher than the desired target. As mentioned above, this metal stack is based on a standard design and would be key to improve for overall simplicity. The second front metal round will investigate additional surface treatments as well as some alternate stack of this family in an attempt to reduce this resistance.

The second grouping of Ge/Pd-based metallizations show very encouraging results, with all the data sets below the desired target. These three stacks have the same metal thicknesses but different sintering conditions. The results show that the contact resistance is somewhat invariant to the sinter condition which will allow for some flexibility in exploring the back metal contact.

Another observation is that the range of the Ge/Pd-based (max to min) is wider than the Au-based metallizations. Additionally work needs to be done to determine if this is actually due to non-uniformity in the metal, or due to measurement error, as the

Project title: Technology Enabling Ultra High Concentration Multi-junction cells
Recipient: North Carolina State University
numbers extracted for the Pd/Ge-based metals are very small and much more sensitive to measurement and fitting errors.

Back Contact

Previous work at Spectrolab has been performed on the back contact metal. One constraint for front and back metallizations is to have the same sintering schedule for both sides as the first approach. It is not preferable to have an optimal sinter at one temperature for one side and a different optimal sinter temperature for the other side.

Sheet Resistance Modeling

Sheet resistance conduction losses will be key to minimize for the very high concentration levels of 2000x. Current state of the art for CPV is ~500-800x. As the trend continues to reach higher concentration levels, it is important to minimize resistive losses in the emitter conductive layer.

One important caveat to the sheet resistance values listed in table 1, is to achieve lower resistance layers with minimal or no loss to top cell response. Preliminary sheet rho modeling has been performed and is later reviewed.

Significant Accomplishments in first budget period**Task 2: Reduction of series and contact resistance**

On subtask 2.1 (emitter sheet resistance) we have achieved the target of $300 \Omega/\square$. The initial design is giving good voltages and efficiencies (similar to a control) even though there is some current loss. On subtask 2.2 (contact resistance) We have exceeded the 36 month goal of the front side metal contact resistance by about an order of magnitude having achieved 10^{-6} compared with a 36 month goal of 10^{-5} . On the backside metallization the result of 2×10^{-4} is about halfway between the 18 month and 36 month goals.

Task 2 Major achievement: Contact resistances are well ahead of schedule. Front metal is an order of magnitude beyond 36 month goal

Challenges in first budget period**Task 2: Contact and sheet resistance****Task 2.1: Sheet resistance**

Experiments were conducted to achieve the 18-month sheet conductivity target ($300 \Omega/\square$). A set of structures along with a repeat of the structures on a different MOVPE tool were grown. The sheet rho was determined from TLM measurements, however in this case, it is the slope which is proportional to the sheet rho. Wafers were submitted for standard terrestrial full processing to perform electrical characterization.

Top cell conductivity was determined from TLM measurements made on a wafer from the control and the split for both the 1st & 2nd growths and the results are averaged to determine the overall performance of the experimental design. The averaged results give $415 \Omega/\square$ for the control and $277 \Omega/\square$ for the design split #1.

The top cell current density was measured on representative cells (using a one sun gridline pitch and non-representative cell measurements removed). Table 3 summarizes the average top cell conductivity and the resulting top cell current density.

Table 3: Results of Top Cell Conductivity Experiment #1

	avg. sheet rho (Ω/\square)	avg. AM1.5D TC Jsr (mA/cm^2)
control	415	14.6
split #1	277	13.9

In this case, there is a loss in the average top cell current density. Wafers were also submitted for LIV testing under two LIV concentration levels (50 and 81 W/cm² incident intensity). Figure 5 shows the average V_{oc} for cells and yielded cells (>36.8%) for 3 different pitches. The two trials are from two different MOVPE tools.

The results show that V_{oc} is on par or slightly higher for the two trials. The photomask used is an experimental photomask with a range of gridline pitches. Results shown are for 81 W/cm² (900x, using 0.09 W/cm² as one sun intensity).

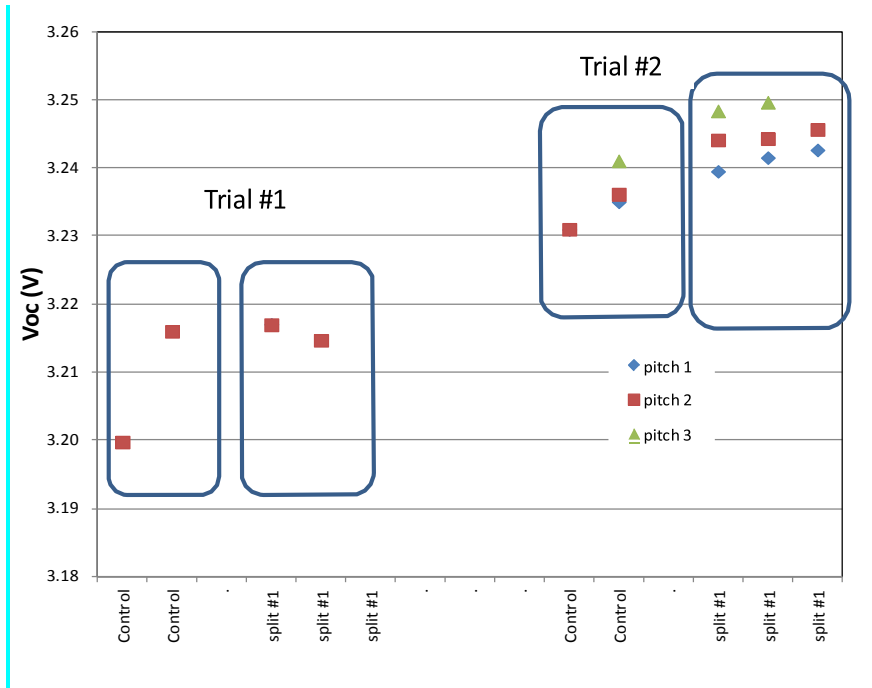


Figure 3-5: Yielded average Voc

Figure 6 shows the corresponding AM1.5 yielded average efficiency for the two trials. It should be noted that even with the top cell current loss, as mentioned above, the non-optimized experimental design is approximately on-par with the control for a range of gridline pitches. This is an encouraging result in that the initial design is giving good voltages and efficiencies that are similar to a control even with the current loss. Further effort would involve optimizing the design to recover the current loss which is expected to gain an efficiency boost.



Figure 3-6: Yielded average efficiency

Task 2.2: Contact resistance

Front-side Metal: The n-type contacts should have low work functions and high dopant concentrations in the n-type semiconductor in order to reduce the junction barrier height to achieve low resistance ohmic contacts. The metal work function should be less than or equal to the work function of the semiconductor. Because of the low statistics of TLM patterns on the wafer (one on the left, top, right, and bottom of the wafer), estimates of the range of fits to the TLM data were made to get a sense of the range of the specific contact resistance. The average resistance R , determined from the IV sweep, and the minimum and maximum resistance values were used to determine the range of fits.

The actual spacing between pads were measured for each TLM pattern and specific contact resistivity was recalculated. The nominal pad size is used. The measured spacings are approximate. The specific contact resistivity (with measured S) is shown in Fig. 6.

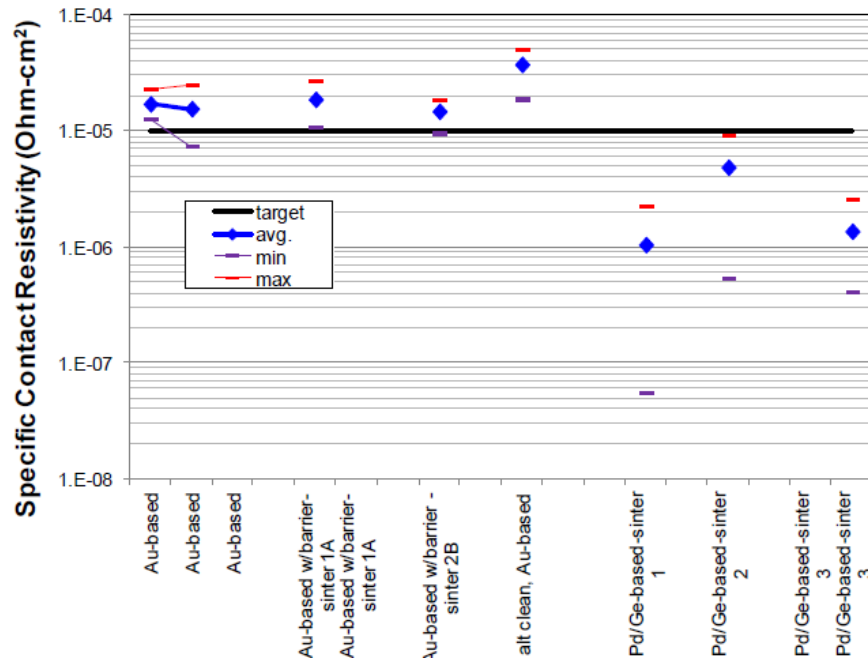


Figure 3-7: Summary of measured specific contact resistances for front side metal with measured pad spacings (S).

Analysis & Discussion

In all cases of the TLM data, show results that have approximately the same order of magnitude. There are some differences that show depending on measured vs. nominal spacing and TLM design used. In all cases the Au-based metallizations and variations have specific contact resistances higher than the desired target. As mentioned above, this metal stack is based on a standard design and would be key to improve for overall simplicity. The second grouping of Ge/Pd-based metallizations show very encouraging results, with all the data sets below the desired target. These three stacks have the same metal thicknesses but different sintering conditions. The results show that the contact resistance is somewhat invariant to the sinter condition which will allow for some flexibility in exploring the back metal contact.

Another observation is that the range of the Ge/Pd-based (max to min) is wider than the Au-based metallizations. Additionally work needs to be done to determine if this is actually due to non-uniformity in the metal, or due to measurement error, as the numbers extracted for the Pd/Ge-based metals are very small and much more sensitive to measurement and fitting errors.

Backside Metal: p-type germanium wafers were prepared so that the wafer backside surface would be as representative as possible of production-like wafers at the metallization step, given the wafers did not go through the entire fabrication process. For the experiment, two different wafer preparations and three metallizations, were explored. For p-type material, the metal work function should be equal to or greater than that of the semiconductor to form a good ohmic contact, therefore metallizations utilizing Pt, Ni, and Pd were chosen. Wafers were patterned on the backside of the wafer with the same mask as used for front side metallization optimization. The wafers all received RTA anneals.

Figure 8 shows the results of the initial back-metal experiment. The figure shows the most promising splits based on initial TLM measurement. The solid line represents the 18-month target. Based on initial measurements, there are a number of encouraging results that are lower than the 18-month target value. Since all the experimental splits includes one of the two pre-metal cleans, further work would need to determine if the clean alone would be sufficient, or if both are required to achieve the lower contact resistivity value. Additionally, it would be interesting to use some of the metallization splits without either of the two pre-metal cleans as well. The data shown is determined from nominal TLM pad spacing. More accurate values can be determined by using actual pad spacings; however they will not change the results significantly.

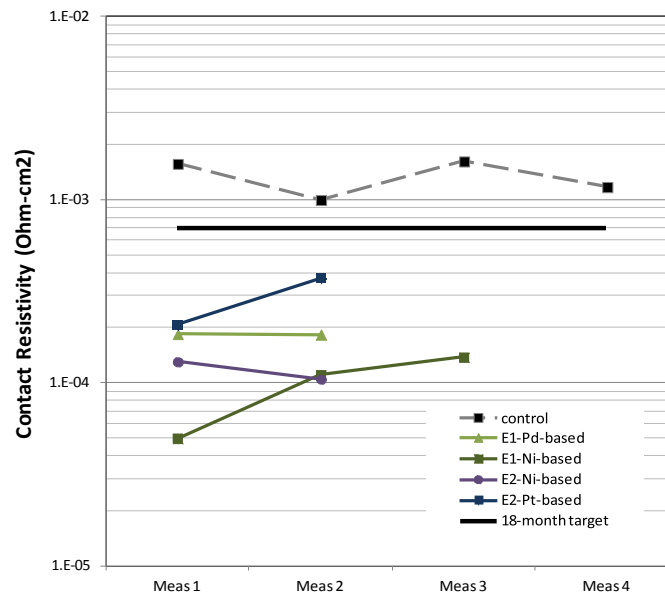


Figure 3-8: Summary of back contact resistivity experiment #1.

Final work on sheet resistance in second budget period Task 5.1&5.2

Spectrolab continued its effort on top layer conductivity experiments. MOVPE runs were performed to further achieve the sheet 36-month program target of 250 ohm/sq for top layer conductivity. Wafers from the MOVPE runs were processed with a quick turnaround process for characterization. As a figure of merit, the top cell spectral response @ 400 nm was chosen to compare designs. Figure 1 shows the spectral response @ 400 nm vs. top layer conductivity (as determined by TLM measurements).

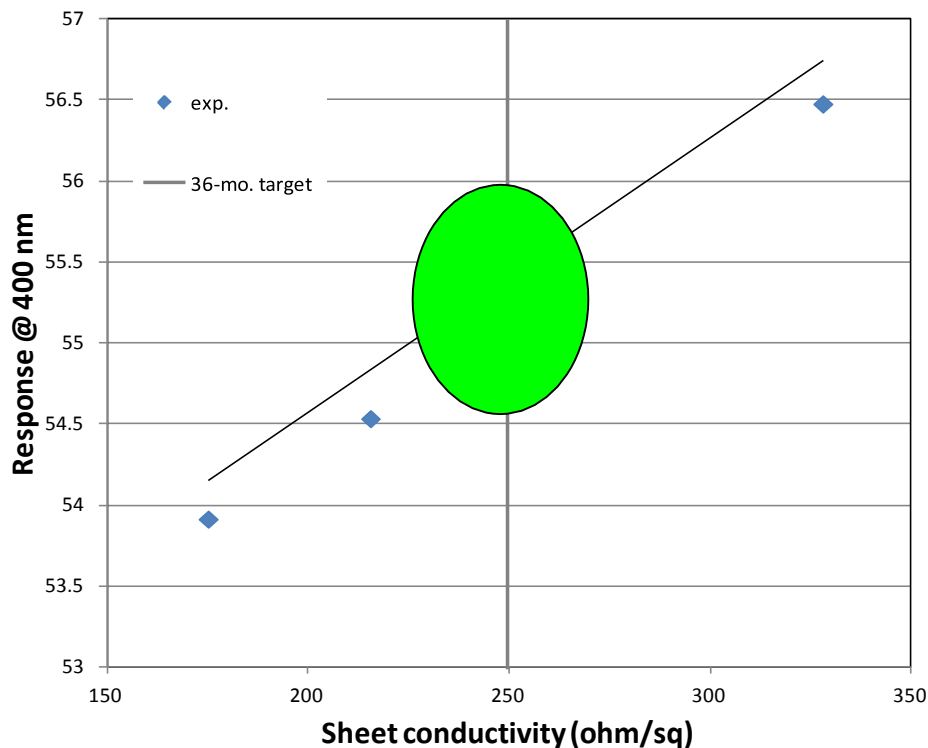


Figure 3-9 – Spectral response @ 400 nm vs. top layer sheet conductivity for experimental runs. Note: No AR coating on wafers.

The light blue oval in Figure 9 highlights the region of interest of the target sheet conductivity of $\sim 250 \Omega/\square$. It should be noted that even at values less than $250 \Omega/\square$, the response is in approximately the same range. It should be noted that there is no AR coating on these cells and do not have terrestrial grids. The AR coating should increase the response by $\sim 30\%$.

Figure 10 shows the quick turnaround V_{oc} for a control and two experimental designs. The average V_{oc} for the two experimental runs are shown relative to the control.

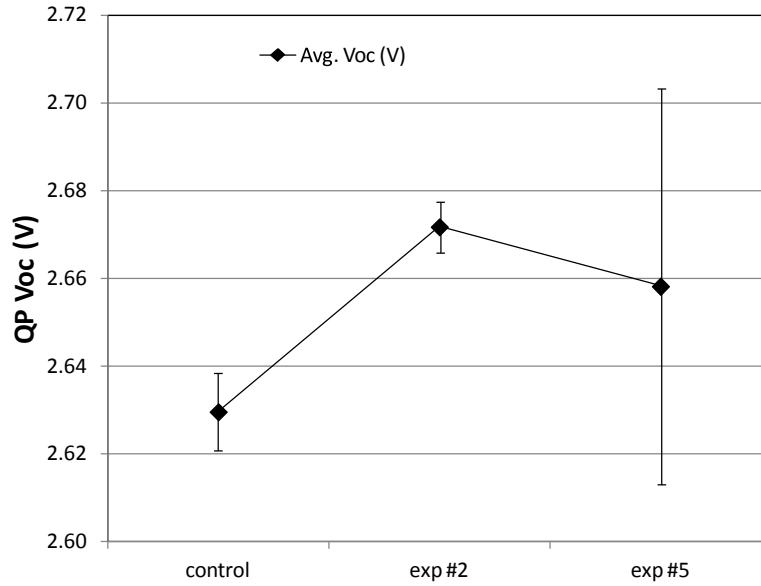


Figure 3-10 – QP V_{oc} for sheet conductivity experiments.

Figure 11 shows the quick turnaround FF for a control and two experimental designs. The average FF of the two experimental runs are on shown relative to the control.

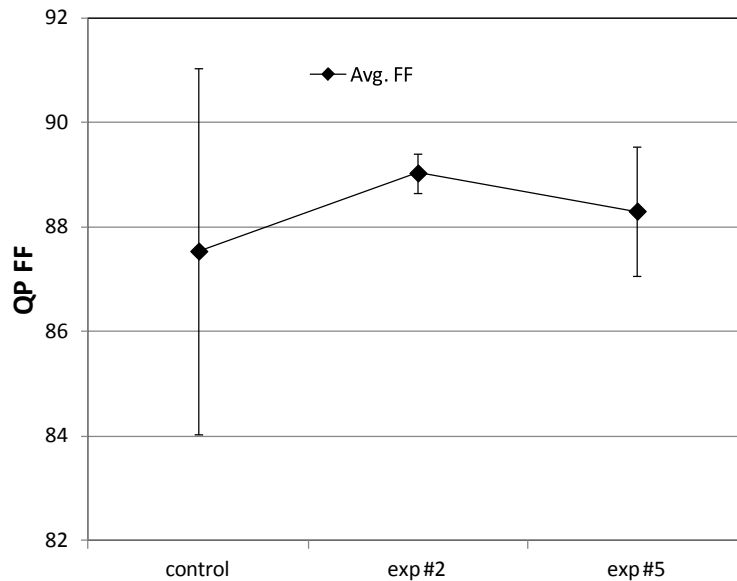


Figure 3-11 – QP FF for sheet conductivity experiments.

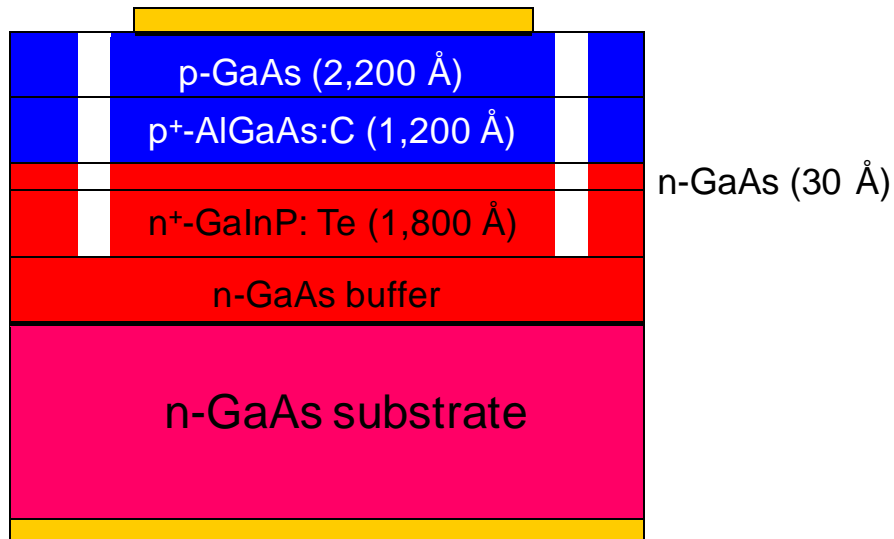
It should be noted that the cells are tested at 1 sun AM0 intensity. Further effort is needed to more fully characterize under terrestrial spectrum and intensity levels. The initial data analysis shows the sheet conductivity is in the range desired with nominal performance relative to a control based on initial characterization.

The next step for this portion of the experiment would be to process wafers at the full process level for high concentration LIV testing and additional characterization.

Next: Spectrolab investigated the NCSU tunnel design task 5.3.

Spectrolab investigated the growth of the tunnel junction design NCSU recommended to demonstrate the tunnel junction (as described in APL 103, 103503, Samberg, *et. al.*) in production type reactors.

Figure 12 shows a cross section schematic of the NCSU tunnel junction device (note: figure is not to scale) as is the same as described in the paper.



NOTE: not to scale

Figure 3-12 – Cross sectional device schematic for NCSU tunnel junction as described in APL 103, 103503, Samberg, *et.al.* Note: not to scale.

Results from these experiments were as follows:

Experiments on GaAs substrates showed a drastic improvement in peak current confirming effects seen by NCSU; initial results are shown in figure 13

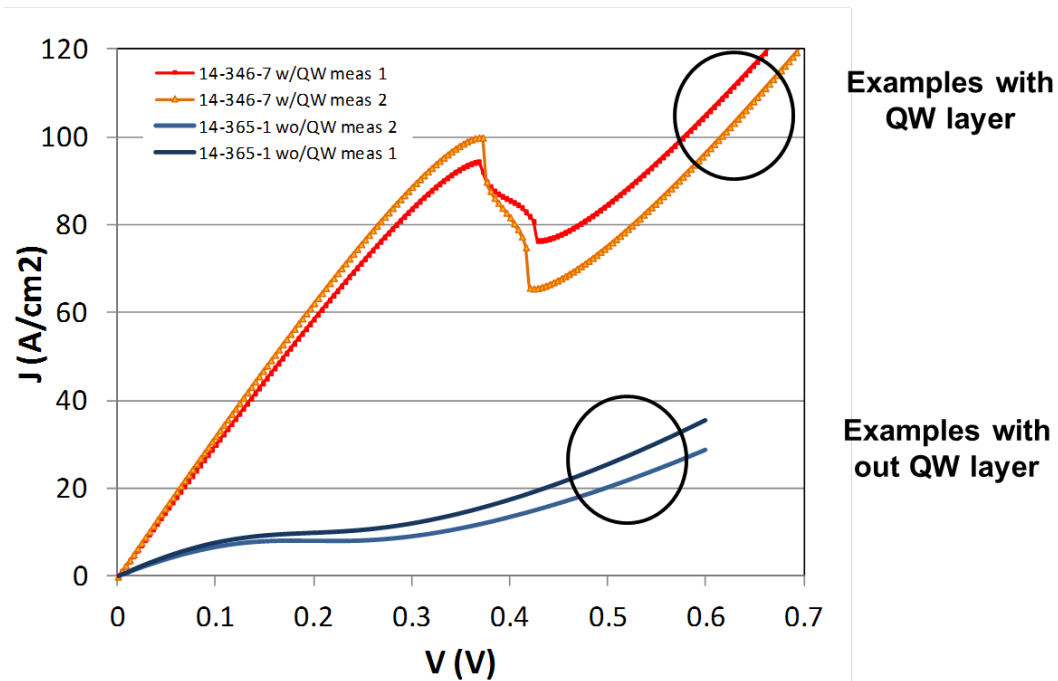


Figure 3-13 : Structures grown on GaAs at Spectrolab with and with-out the QW layer

The next step was to check if the results could be duplicated on Germanium substrates which are used for triple-junction cells (n-type Ge rather than production p-type Ge was used.).

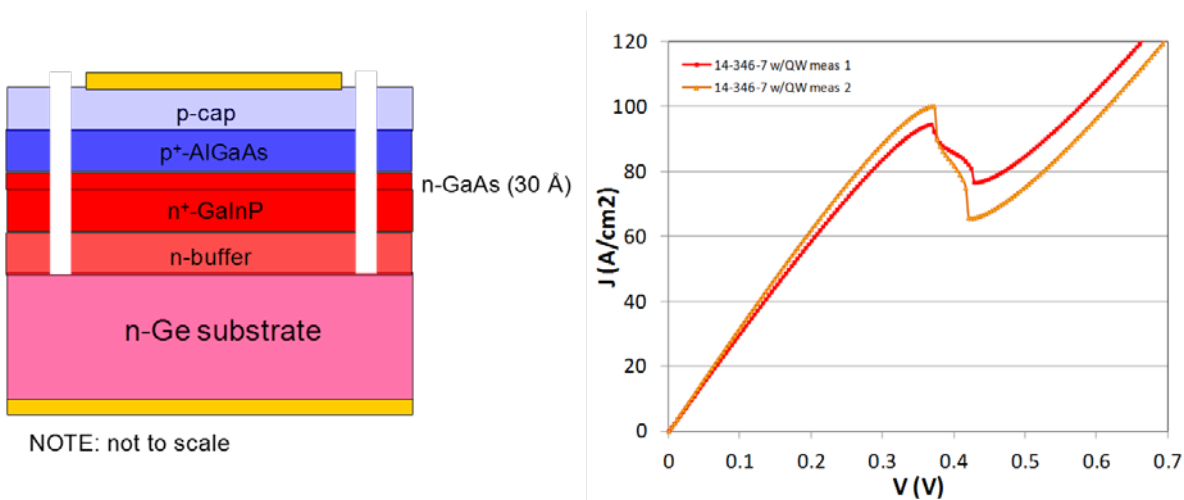


Figure 3-14: NCSU type tunnel junction grown on Ge substrate

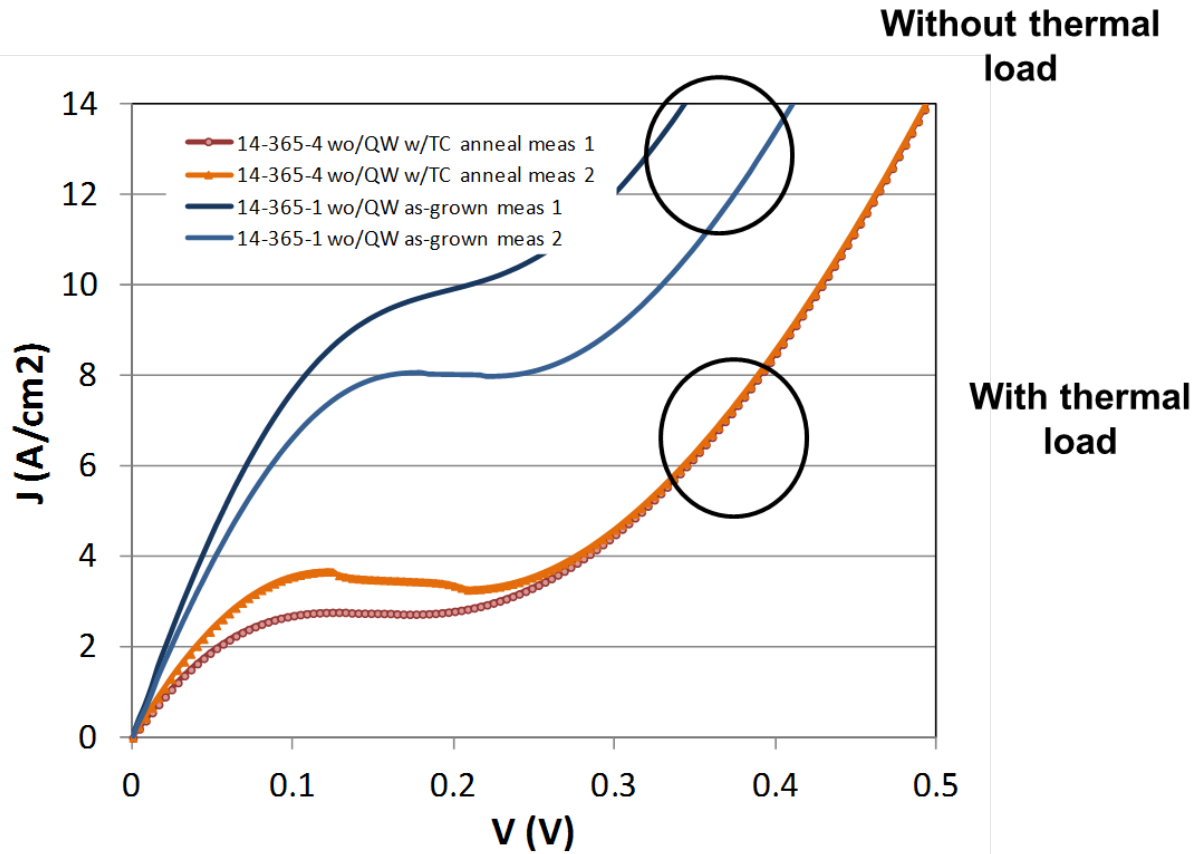


Figure 3-15: Effect of thermal load on tunnel junctions without QW layer

The other aspect of the tunnel junction growth which is absolutely vital to the completed multijunction cell is the stability of the tunnel junction performance during the growth of the top cell on it. Experiments on the baseline tunnel junction (without GaAs QW layer) showed a degradation of somewhat more than a factor of two when subjected to an appropriate thermal load as can be seen in figure 15.

Final experiments with integration of multi-junction cells

Table 4 shows a list of the configuration of the experiment matrix of concentrator cells. Cells were fully processed into concentrator cells based on CDO-030. CDO-030 stands for concentrator, dual ohmic (~30 mm²). Cell dimensions are roughly 5 mm x 6 mm with dual parallel ohmics. The CUTJ control is a standard terrestrial design solar cell. It should be noted that designs #2-4 are all initial growths for initial characterization under high concentration and are not fully optimized designs or growths.

Task 5.3&7 Multijunction cell fabrication and testing.

Table 4 – Experimental Matrix for Concentrator cell Designs

No.	Device	Description
1	CUTJ control	Baseline (no changes)
2	CUTJ + tunnel	w/variation of NCSU QW tunnel
3	CUTJ + sheet conduction	w/higher sheet conduction design
4	CUTJ + tunnel + sheet conduction	w/ variations #2 & #3 above

LIV was characterized using an IOFFE high concentration solar simulator. The measurements are used for screening and trends. Concentration was measured up to 5000X. Figure 16 shows example LIV curves for each design type and various concentrated light levels. The highest LIV curves (in light green) are approximately @ 5000X. It should be noted that there are no tunnel junction failures observed for any design.

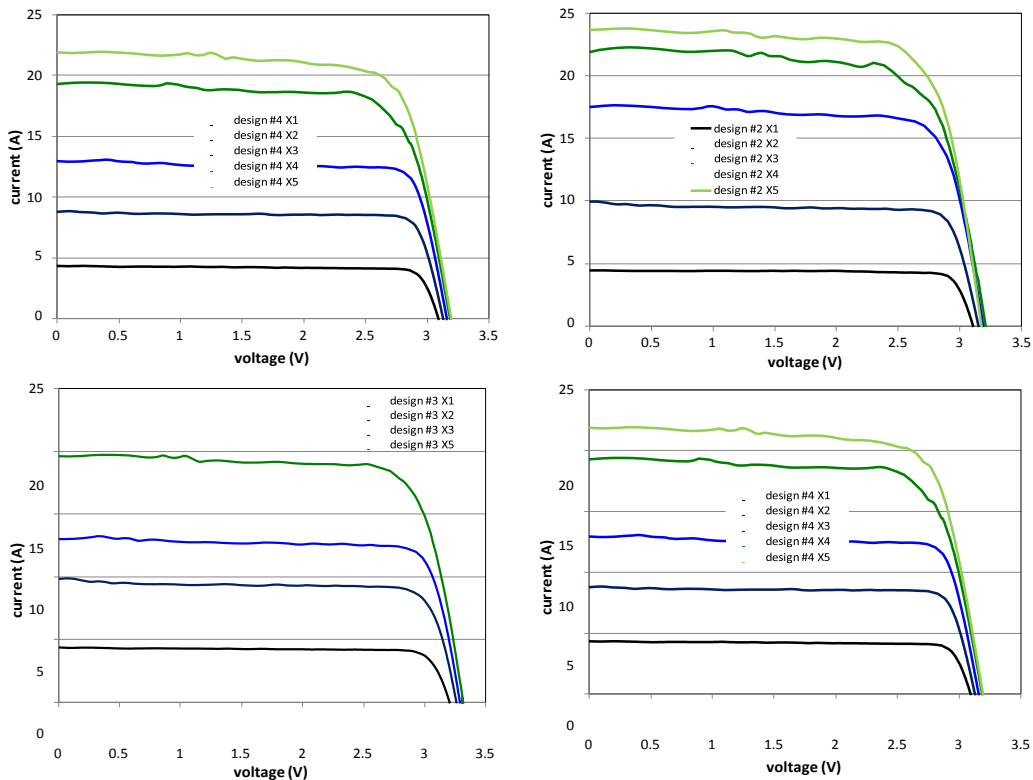


Figure 3-16 – Example LIV curves for Four Designs in Table 1 at concentrations from 1000-5000X.

For the following data sets, 1-2 cells per wafer per type were measured. The data sets are an average of 5 measurements per cell per condition. The statistics are limited at this point but aim to characterize preliminary performance of the four cell designs in Table 4.

Figure 17 shows I_{sc} vs. concentration for the control and 3 experimental variations. Concentration level is determined from spectral response measurements, using the current limiting J_{sc} and nominal aperture area. The charts shows that the cells are well behaved and linear in I_{sc} as expected.

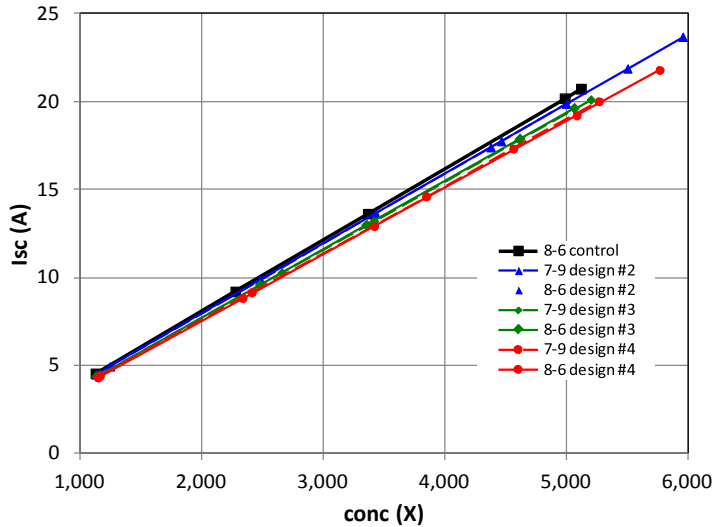


Figure 3-17 – I_{sc} vs. Concentration

Figure 18 shows V_{oc} vs. concentration level for the four designs. The dashed and solid lines indicate two different cells. Design #2 & #4 both contain a variation of NCSU QW tunnel junction. From the chart, there is 100-150 mV V_{oc} difference between the control and the QW tunnel junction. As mentioned previously, these designs are initial growths and are not optimized in term of growth conditions or design. Additional effort is required to understand the V_{oc} difference and recover. Design #3 has the same tunnel as the control and gives nominally the same V_{oc} under concentration. All the V_{oc} 's increase with concentration.

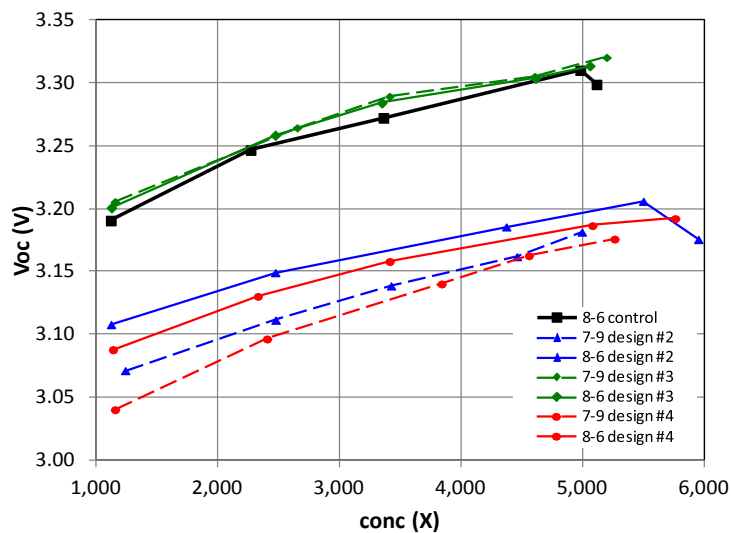


Figure 3-18 – V_{oc} vs. Concentration

LIV/SR Analysis

Figure 19 shows FF vs. concentration for the same cells under test. In general there is a reduction in FF at increasing concentration levels. The spread in some of the FF for the same cell type are potentially due to non-uniformities in the growth.

Additionally this cell size and grid pitch is not optimized for these high concentration levels. The cell size and pitch would need to be designed for >2000x operation to minimize the effects of series resistance. However, the FF shows good retention (see Figure 1) at high concentration. The figure shows design #4 with FF > 82% @ 2000X for the milestone 5.3.

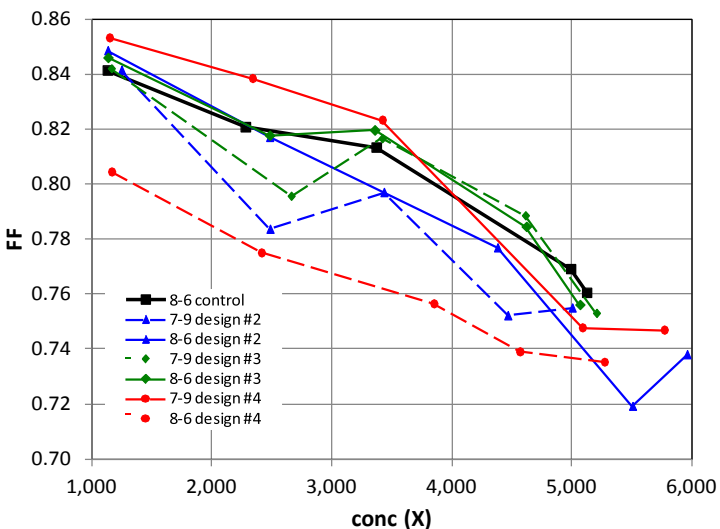


Figure 3-19 – FF vs. Concentration

Figure 20 shows the average top and middle cell J_{sc} determined from spectral response measurements for a small subset of cells. The first columns shows average top cell (blue) and middle cell (red) J_{sc} . The three additional columns show average top cell J_{sc} for the three experimental designs with corresponding increase in middle cell J_{sc} .

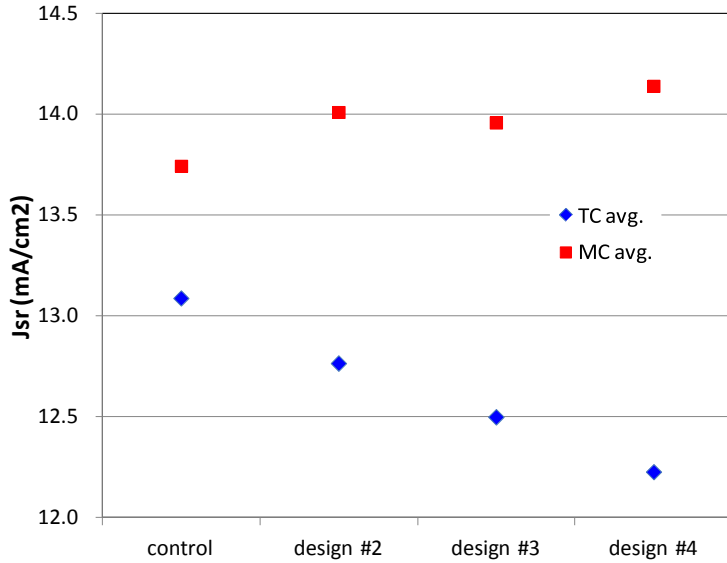


Figure 3-20 – Top and Middle Cell Jsc for Control and Experimental Designs

Figure 21 shows External Quantum Efficiency (EQE) of the top and middle subcells for a control and an experimental design. The solid line shows the control and the symbols show the experimental design. The experimental top cell does show some loss of collection near the back of the cell, the corresponding experimental middle subcell does show a slight increase in EQE. This indicates the tunnel is allowing more light through it into the middle cell. Optimization is required to improve experimental top cell performance.

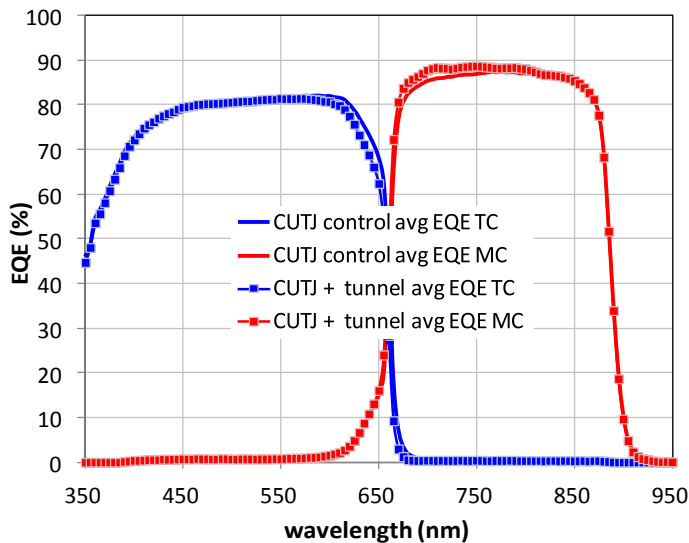


Figure 3-21 – Top and Middle Cell EQE for Control and Tunnel Design (example)

Summary

A concentrator control and three experimental designs investigating combinations of quantum well tunnel junction and conduction layer devices were grown and fabricated. A small subset of cells was measured for initial LIV characterization. All designs show good LIV behavior up to 5000X. **No tunnel junction failures were observed for any of these initial measurements.**

LIV for experimental designs show $FF > 82\%$ @ $> 2000X$. From EQE measurements, a higher middle cell response is observed in an experimental tunnel junction design indicating higher transmission into this subcell over the control. Vocloss is observed with experimental tunnel junction designs and may indicate a larger voltage drop across the tunnel. Special test structures would be needed to confirm this.

Overall, further characterization and optimization is needed pending additional resources to fully capture the benefit of the QW tunnel and high conduction sheet layer on new designs.

Overall, very promising results are achieved on these initial designs with the NCSU QW tunnel junction tested at very high concentration levels as well as a good example of academia and industry working together. Additional effort is needed to realize the final milestone of 40% @ $> 2000X$ in terms of device growth and design optimization and cell size and pitch optimization.

Section 5 --Task 3: Heat dissipation:

The heat dissipation task of this project was aimed at demonstration that there were reasonable technical solutions to the problem of dissipating the increased heat flux in a cell operated at 2000x. The chosen baseline was the substitution of a 5mmX5mm cell at 2000x for a 1cmX1cm cell at 500x, which was typically used at the time this project was begun, the goal was to show that the temperature increase of the higher concentration cell could be held to about 10C the specified goal was a 15C temperature rise from the heat sink (the baseline cell assemblies had a typical rise of 7C above the heat sink)

The basic problems to be solved concerning heat spreader design consists of providing adequate heat spreading conductivity and possibly electrical insulation. The electrical insulation problem involves cost considerations as well as technical possibilities. The baseline structures used in industry have generally used an aluminum oxide insulating substrate. The coefficient of thermal expansion is reasonably matched to the cells and the cost is relatively low. The thermal conductivity is, however, comparable to that of gallium arsenide, less than that of germanium.

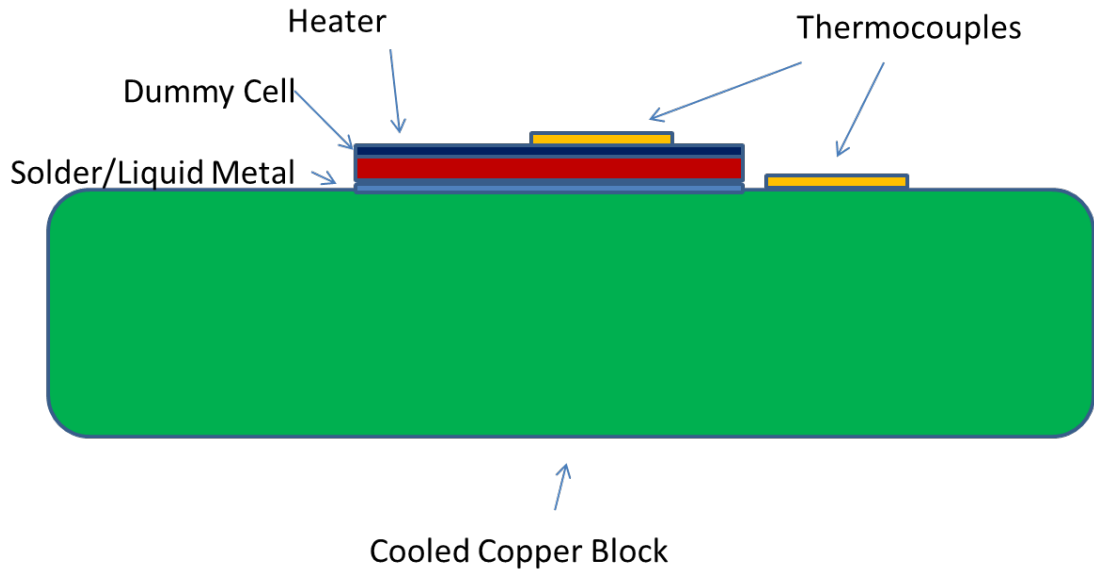
Typical mountings for CPV cells use a metallic conducting layer on an alumina substrate. In the case of baseline 500 X 1 cm² cells the heat spreading by the conducting layer and the alumina mount is negligible. However, with smaller cells operating at higher concentrations a spreading layer is necessary. Copper is the obvious choice due to its high thermal conductivity and is the material which is used for the program both experimentally and for the computer modeling of devices. One of the principal questions to be answered by the modeling is if alumina is satisfactory as an insulating material for higher concentrations. As a first approximation, the alumina should have the same temperature drop at the high concentrations as a 500 X if the heat spreading is accomplished between the cell and the alumina insulating layer. In this case, the additional temperature rise will be due to the rise in the cell and that in the heat spreader. If this rise is more than acceptable, the temperature rise can be reduced by substituting an insulator of higher thermal conductivity such as aluminum nitride for the alumina insulating layer. the Aluminum nitride is, however, much more expensive.

For MJC operating at 2000 and conversion efficiency of 35%, about 135 W/cm² will be generated. Based on NREL analysis a 2000x system is expected to operate at 20°C hotter than the heat sink. We have designed a heating system based on I²R heating of a thin GaAs film, where I is the current passing through the GaAs and R is the film resistance realized. The wafer and the heat sink copper block temperatures are measured by thermocouples. We have decided on a 5 mm square test structure since the overall approach of the program is to enable the substitution of cheaper cells into existing concentrator structure designs which most commonly use 1 cm² cells at 500x. An electrode structure has been designed to produce a resistive heating element suitable for providing the 130 W/cm² (for test structures: 5 mm square, providing 35 W) when used

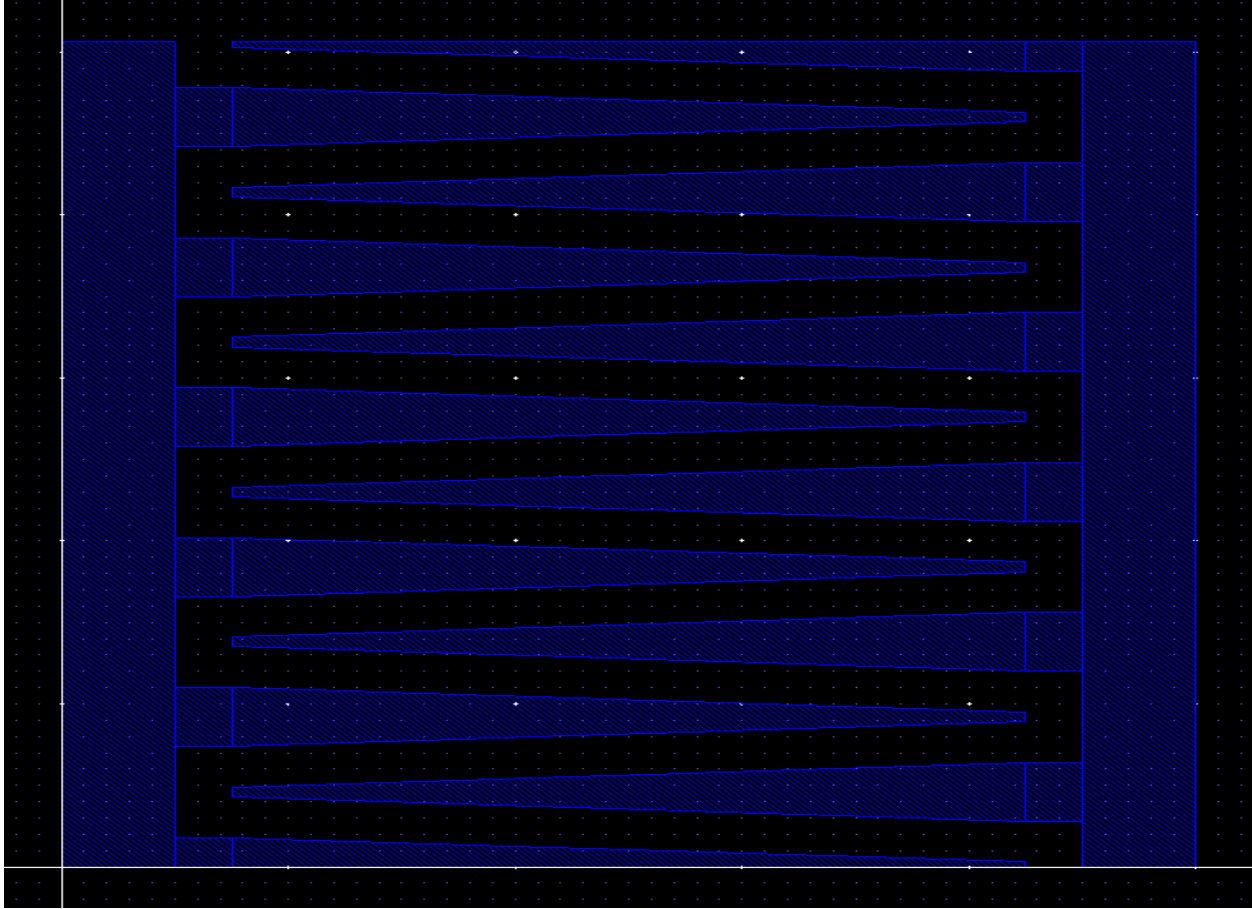
with an available 30 volt digitally controlled current supply. A layer of 0.1μ 1×10^{18} p-type material and an electrode structure providing 176 squares in parallel will achieve this result. A test block of copper $\frac{1}{4}$ in thick has been fabricated which will serve to spread the heat from the 5mm square cell. The most convenient wafer on which to fabricate the dummy cell was a 350 μ m thick GaAs wafer of the type routinely used for calibration samples.

A test structure was assembled using ohmic heating of a GaAs film grown on GaAs substrate attached to copper heat sinking block. The input electrical power, generated heat, can be adjusted, using constant current supply, up to 135 W/cm^2 representing the heat generated in a MJC at 2000 \times . The temperature difference between the wafer surface and the heat sink is measured by a pair of thermocouples. We have reviewed the data available on thermal interface materials and concluded that pure indium is worth trying for the interface material. Over the temperature range of most interest (50-100 $^{\circ}\text{C}$) indium may be superior due to higher thermal conductivity than the In-Ga liquid metal and its annealing characteristics may ameliorate any fatigue problems.

A test structure was assembled using ohmic heating of a GaAs film grown on GaAs substrate attached to copper heat sinking block. The input electrical power, generated heat, can be adjusted, using constant current supply, up to 135 W/cm^2 representing the heat generated in a MJC at 2000 \times . The temperature difference between the wafer surface and the heat sink is measured by a pair of thermocouples. We have reviewed the data available on thermal interface materials and concluded that pure indium is worth trying for the interface material. Over the temperature range of most interest (50- 100 $^{\circ}\text{C}$) indium may be superior due to higher thermal conductivity than the In-Ga liquid metal and its annealing characteristics may ameliorate any fatigue problems. .A schematic of the test structure is shown in figure [5-1]



Figure[5-1]: Schematic of test structure for heat dissipation



Figure[5-2]: Layout of the heating grid contacts for the heat dissipation test structure

Task 3: Heat dissipation

We first modeled the commercially available receiver unit of Spectrolab at 1000x and obtained the same thermal resistance as they quoted for MJC on an Al_2O_3 support block. When the Al_2O_3 support is replaced by copper block our estimate for the MJC at 2000x

is shown in table 3. Applying the same modeling method to the test structure containing a dummy sample fabricated from the 350 μ material indicates that we can expect the temperature difference to be about 6 °C greater than in the case of the final triple junction cell. Table 2 shows the contributions to the temperature rise ΔT from the MJC components

Table 3: Modeling of thermal properties of triple-junction cell on copper heat-spreader for a 130 W/cm² dissipation

Layer	Thickness (μ m)	Thermal Conductivity k (W/cm·K)	Thermal Resistance Rt (K/W·cm ²)	ΔT (K)
GaInP	1	0.05	0.002	0.26
GaAs	3	0.46	0.000652	0.084783
Ge	175	0.6	0.029167	3.791667
Solder	30	0.4	0.0075	0.975
Copper(edge)	3000	4	0.075	9.75
Total	3209		0.114319	14.86145

Task 6: Heat dissipation

For MJC operating at 2000 and conversion efficiency of 35%, about 135 W/cm² will be generated. Based on NREL analysis a 2000x system is expected to operate at 20 °C hotter than the heat sink, We have designed in phase I a heating system based on I^2R of a thin GaAs film, where I is the current passing through the GaAs and R is the film resistance. By varying the input current, the desired heat generated in the range from 0-150 W/cm² is realized. The temperature difference between the wafer surface and the heat sink is measured by a pair of thermocouples.

W/cm ²							2000x	130
		t μ		κ		Rt		ΔT
GaN/P		1		0.05		0.002		0.26
GaAs		3		0.46		0.00065217		0.08478261
Ge		175		0.6		0.02916667		3.79166667
Solder		30		0.4		0.0075		0.975
Copper		5000		4		0.125		16.25
Total		5209				0.16431884		21.3614493

W/cm ²							2000x	130
		t μ		κ		Rt		ΔT
GaN/P		1		0.05		0.002		0.26
GaAs		3		0.46		0.00065217		0.08478261
Ge		175		0.6		0.02916667		3.79166667
Solder		30		0.4		0.0075		0.975
Copper 5mm+edges		3000		4		0.075		9.75
Total		3209				0.11431884		14.8614493

**For 2000 suns, $\eta = 35\%$, Heat generation:
 $(100 \text{ mW/cm}^2)(2000)(1-0.35) = 130 \text{ W/cm}^2$**

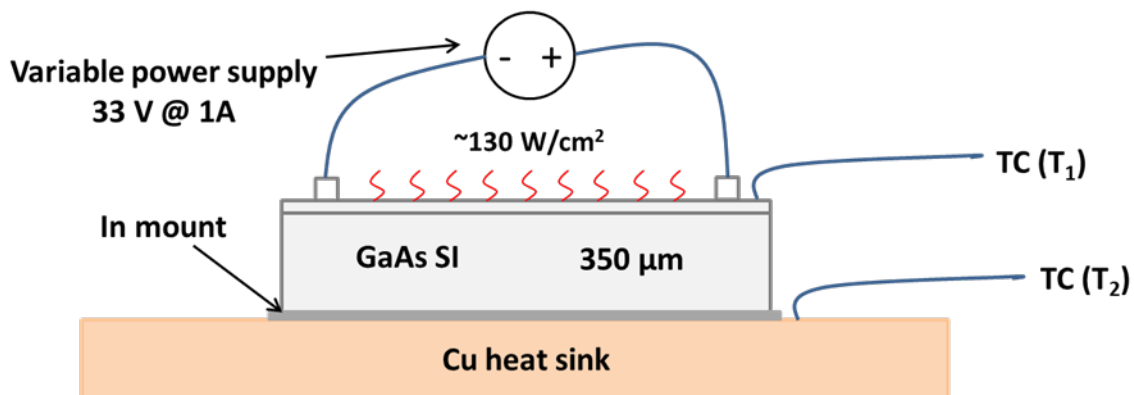


Figure 5-3 initial thermal test result

$T_1 - T_2 = 18^\circ\text{C}$ measured

$\Delta T = 20^\circ\text{C}$ interim goal

						Concentrat	W/cm2
						2000x	130
		Thickness μ	k W/cm K			Rt K/Wcm2	Delta T
GaNP		1	0.05			0.002	0.26
GaAs		350	0.46			0.076087	9.891304
Ge		1	0.6			0.000167	0.021667
Solder		30	0.4			0.0075	0.975
Copper(edge)		2100	4			0.0525	6.825
Total		2482				0.138254	17.97297

Work on action item 3 : During the recent fiscal period the activities in the heat spreading task have consisted of work along two tracks; track one has been experimental verification of acceptable heat drop using the basic dummy set up, track two has been modeling to verify that effective and reasonably obtainable heat dissipation hardware can be produced. Since the previous simple modeling had shown that there was about 10° C thermal rise in the 350 μ substrate used in the initial tests while about 4° C would be expected for production Ge substrates, we are working on a test setup which uses a GaAs substrate thinned to approximately 100 μ (this will have a thermal resistance comparable to the Ge substrate since the Ge (60.2 W/mK) has a higher thermal conductivity than GaAs(46W/mK). The electrical conductivity of Ge substrates would require that electrical isolation capable of holding off more than 30 volts would have to be incorporated in the heater structure if a Ge substrate were used in the test setup.

When undertaking the detailed modeling task the first decision to be made is the general type of mounting to consider. The heat dissipation problems of 2000x concentration systems varies with the type of system under consideration. In the case of systems using dense arrays the thermal resistance of the cell and of any electrical insulation required between the cell and heat sink are the prime considerations. Water cooled heatsinks developed for semiconductor electronics are capable of handling the heat dissipation. This has been demonstrated by work at IBM in Switzerland. The dense array type of receivers are basically required/preferred for systems recovering both thermal and photovoltaic energy; this approach is finding increased interest (for instance in recent ARPA-E request for proposals). The detailed design problem for these systems is the integration of heatsink and electrical isolation/ connections; however IBM seems to have solved these problems. For this reason our project has emphasized the solution of heatsink problems for systems using individual cells, The baseline considered is systems using 1 cm² at 500 X concentration. The problem considered here is the replacement of 1 cm² 500 X cells by 5 mm² 2000 X cells. The specific problem to be solved is that of achieving heat spreading such that the flux into the

heatsink would be the same as for the 500 X cell. The heat spreading problem is particularly important for the relatively larger cells.

We've obtained COMSOL multi-physics modeling software, which is available at North Carolina State University, and used it to model the thermal properties of a number of cell sizes and heat spreading configurations. As was projected by our earlier simplified thermal modeling, the temperature rise in the cell itself is dominated by the thermal resistance of the substrate for the normal vertically grown cells on Ge. The temperature rise of these cells and solder joint to the heat-spreader is about 5°C, this is twice the rise at 1000x, but is not a serious problem. Thus for conventional concentrations the heat dissipation challenge is within the heat sink itself, when moving to ultra-high concentration there is an additional challenge (which is the subject of our investigation) in the heat-spreader connecting the cell and baseline heatsink.

We've chosen to use a simplified model of the total structure in which the thermal resistance of the cell is modeled is that of a 200 μ thick germanium layer, this is a reasonable approximation of the germanium substrate and soldered joint to the heat spreader. The additional information which more sophisticated modeling provides is the thermal resistance of the heat spreader. This is important since the heatsinks that operate with 500 X cells are designed for a thermal flux of 33 W/cm² over 1 cm² area. If the heat flux of a 5x5 mm 2000X cell (130 W/cm² over a 5mm square area) was applied directly to this heatsink the thermal resistance, i. e. temperature rise, would be considerably greater than that with the baseline 500 X cell. We have used the COMSOL program to model a series of heat spreaders. The simplest, most efficient, relatively inexpensive spreader heat spreader is a solid copper block 1 cm² and 5 mm thick. The basic model programs in COMSOL consists of the 1 cm² block with a 200 μ germanium 5 mm² cell attached to the top of it. The boundary conditions put into the modeling program are doing the heat flux of 131 cm² on the top of the germanium block, and a boundary condition of the temperature of 298° K (25° C) at the bottom of the copper block.

The first figure (fig 4) shows the temperature gradients expected for the baseline (similar to those commercially available) 500 X receiver. The next figure shows the temperature distribution when a solid copper block is used as a heat spreader for a 5mm² cell with the same total power (2000x).

From figure(5-5) it can be seen that the heat flux is distributed reasonably uniformly across the 1cm² area as in the baseline case (this is evident from the reasonably flat profile of the isothermal plane

next to the heatsink). Thus a 5mm thick copper block will provide adequate heat spreading, and from a comparison of the figures the cell and heat spreader will have a temperature rise of about 5°C greater than the baseline receiver temperature rise (12°C).

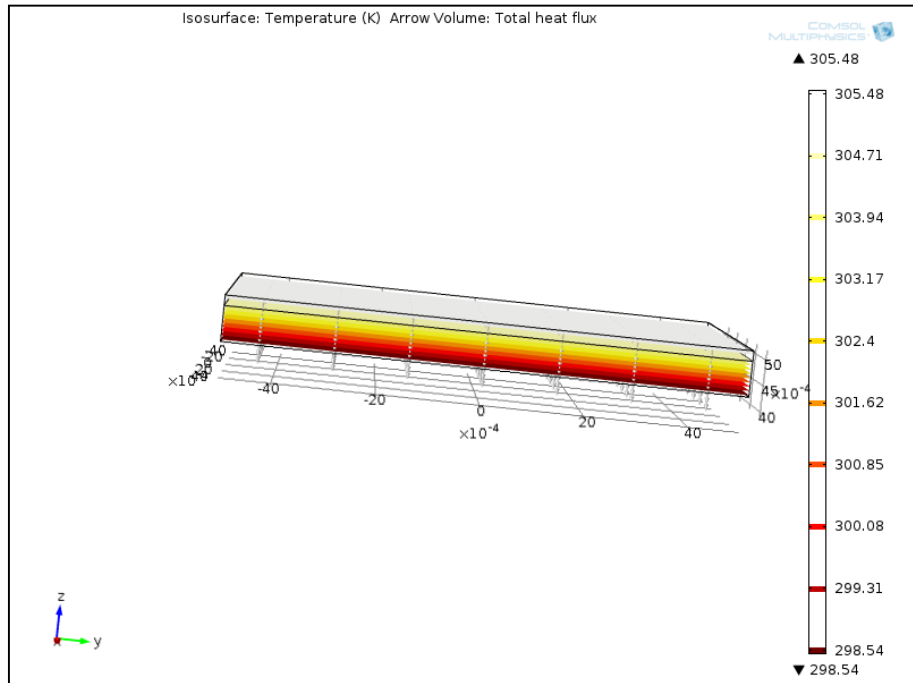


Figure5-4: Baseline = 500x 0.680 Al₂O₃ mount ~7°C rise

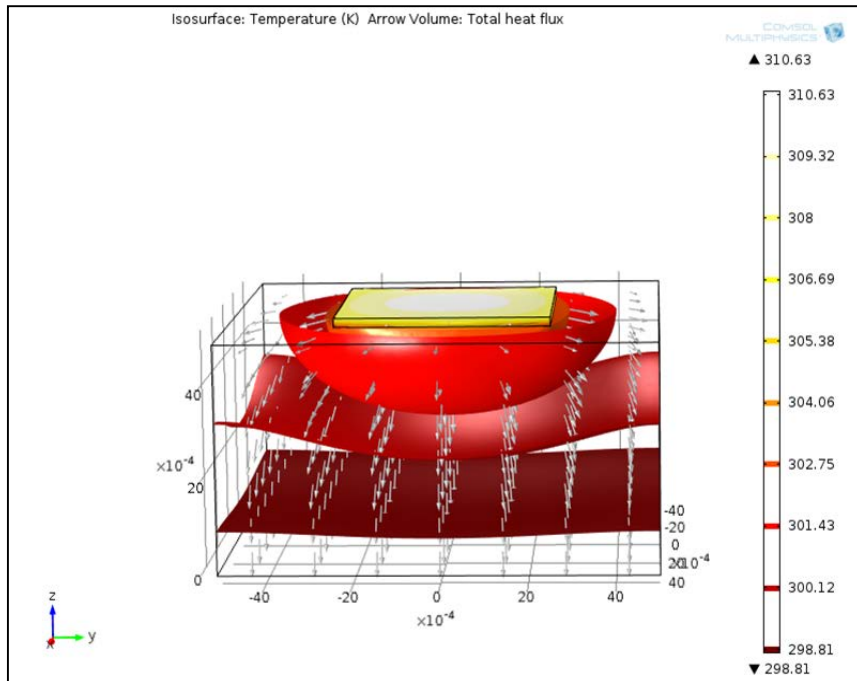


Figure 5-5: 2000x 5x5 cell Copper 10x10x5mm

temperature rise of about 5°C greater than the baseline receiver temperature rise (12°C). Since the fabrication of modules may require the cells to be electrically insulated from the heatsinks we have modeled several assemblies in which an insulating layer is substituted for part of the copper heat spreader. The first model shown in figure 5-6 uses a 500 μ alumina layer which is similar to the 680 μ alumina layer used in the commercial structure.

This assembly has a somewhat higher temperature drop (17°C vs. 12°C for the Cu block) than is considered desirable. However, it must be noted that this temperature drop is only about 10°C greater than the baseline which is our objective.

An

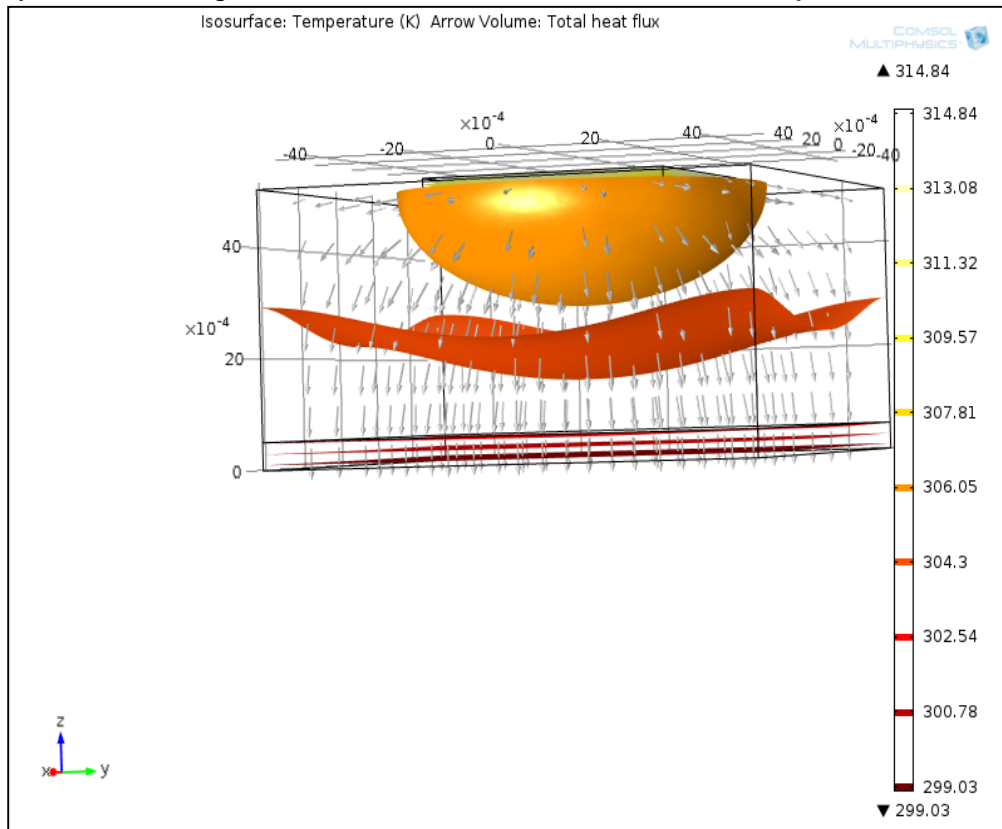


Figure 5-6: 2000x 5x5 cell Copper 10x10x4.5mm $0.5\text{Al}_2\text{O}_3$ 16 °C rise

improvement may be obtained by using an insulating layer of greater thermal conductivity such as aluminum nitride (or silicon with an insulating layer). The result is shown in figure 5-7. The expected temperature distribution for an assembly of this type is shown in the next figure. In this case the temperature distribution (13°C drop) will probably be satisfactory providing the thermal interfaces can be neglected.

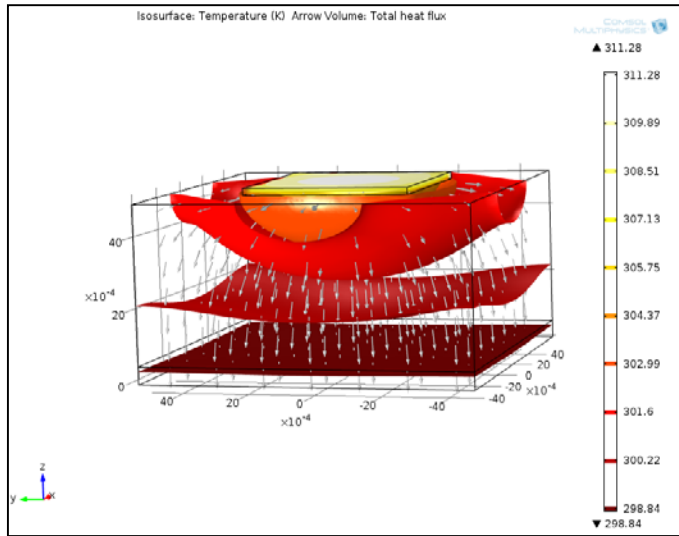


Figure 5-7: 2000x 5x5 cell Copper 10x10x4.5mm
0.5AlN 13 °C rise

This assumption is probably reasonable for the junctions between the insulator and copper block which have a heat flux equivalent to that the 500 X baseline. The thermal contact resistance at the junction between the germanium and copper has been taken into account by the thickness of the germanium used in the model. Actual germanium substrates would be somewhat thinner. The figures produced from the computer modeling program displays isothermal contours and it may be readily seen from these figures that the 5 mm total thickness of the heat spreader produces a reasonably uniform heat flux to the

heat sink. The next question is if this thickness is optimal since a thinner heat spreader might be cheaper and have a lower thermal resistance. The next figure (5-8)shows the

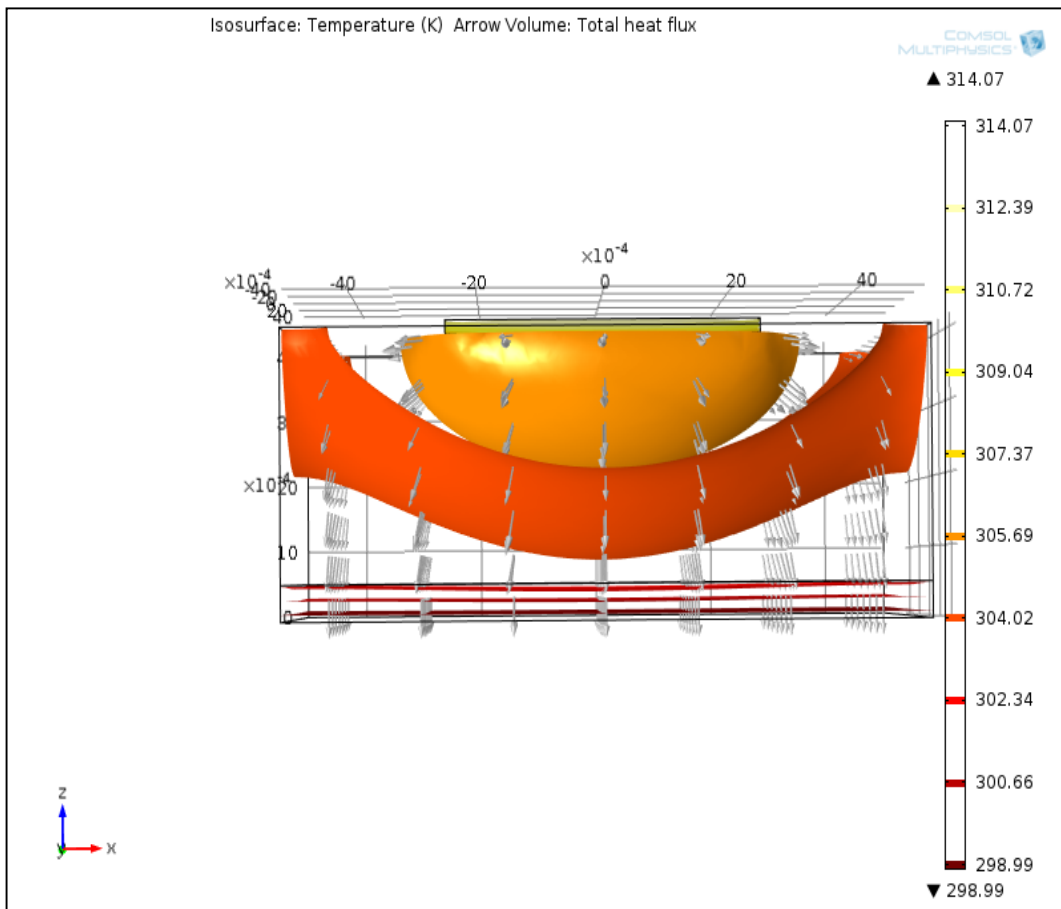


Figure 5-8: 2000x 5x5 cell Copper 10x10x3.5mm 0.5Al₂O₃ 16 °C rise

performance of a heatspreader with a 3.5 mm Cu block. This thinner structure produces a heat flux distribution at the low temperature boundary which is nonuniform and therefore would encounter higher thermal resistance from the module heat spreader. Thus the 4.5 mm block is fairly close to optimal for 1cm² cells.

Since some of the more recent module designs use considerably smaller cells it is interesting to see how the cell size affects the thermal resistance of the heat spreaders; to this end we modeled a series of cells of 1 mm² at 2000 X with various heat spreaders. We've also considered a 0.7 mm x 0.7 mm cell at 2000 X to compare with the 1000 X 1 mm² cell. It's clear from these figures that considerably thinner heat spreaders can be used with smaller cells and possibly less thermally conductive materials to produce comparable temperature rises.

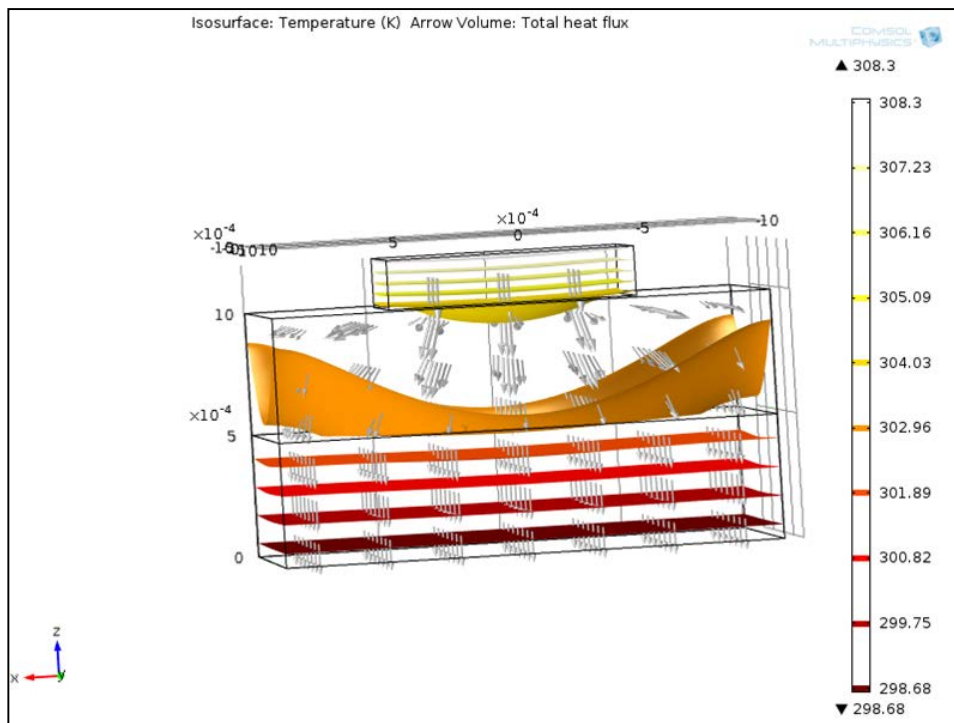


Figure 5-9: 2000x 1x1 cell Copper 2x2x0.5mm 0.5Al₂O₃ 10 °C rise

Figure(5-9) shows the temperature distribution of a 1mm² cell with a composite heat spreader. The temperature rise in this assembly is about 6°C less than that in the 5x5mm cell with the same Al₂O₃ insulating layer.. The temperature gradients in the cell itself and the alumina insulating layer are the same as in the larger cell assembly so the difference is in the heatspreader.

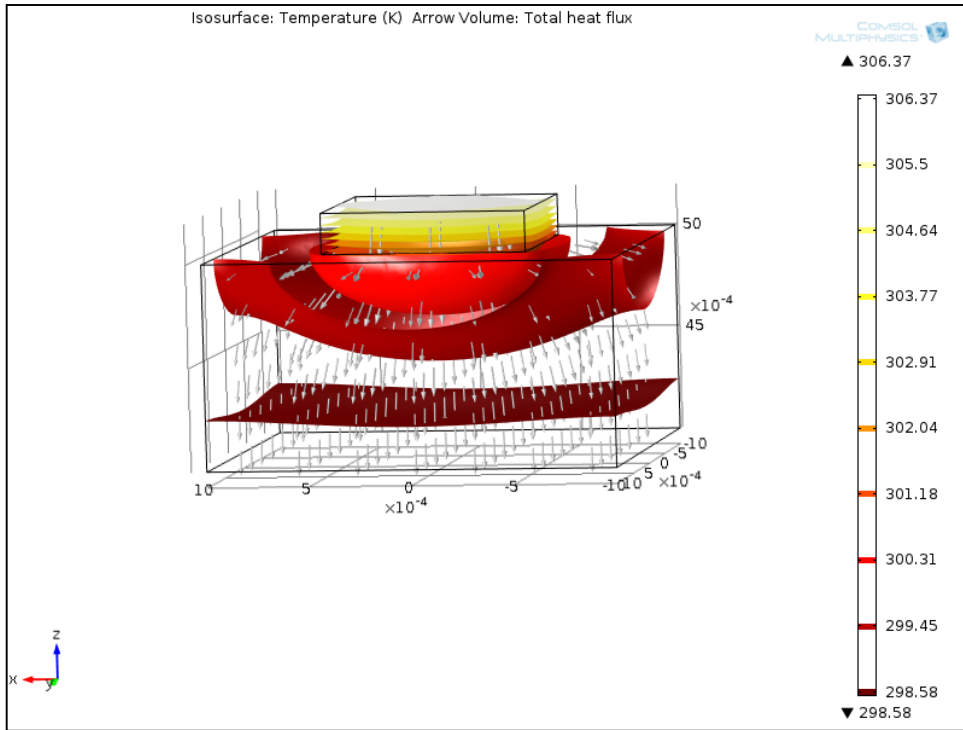


Figure 5-10: 2000x 1x1 cell 2x2x1mm AlN 8 °C rise

Interestingly the same thermal performance can be achieved by using a single piece of AlN for the heatspreader insulator as shown in figure(5-10) This is in contrast to the performance of a monolithic Al_2O_3 heatspreader/insulator shown in figure(5-11) which has a probably unacceptable 20°C rise.

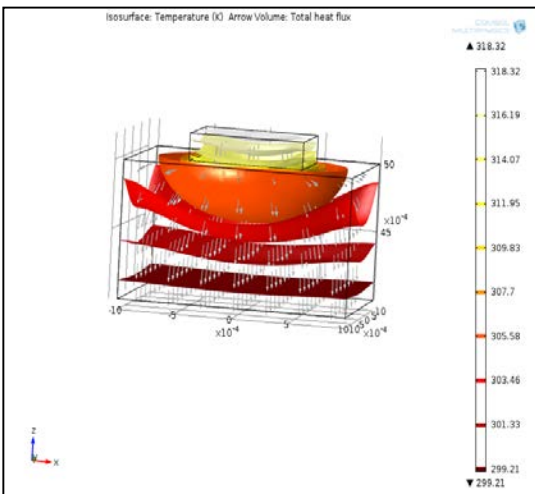


Figure5-11: 2000x 1x1 cell 2x2x1mm Al_2O_3 20 °C rise

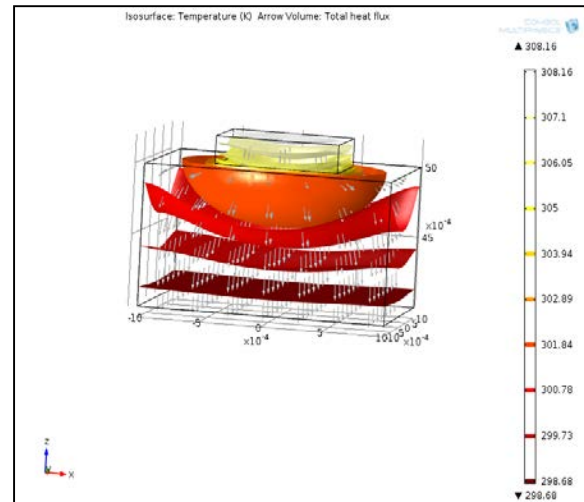


Figure 5-12: 1000x 1x1 cell 2x2x1mm Al_2O_3 10 °C rise

The calculations for the 1mm² show that smaller cells are easier to use at high concentrations since a geometrically similar heat spreader will be smaller and thus there will be proportionally less thermal resistance in the heat spreader. On further consideration the challenge of the heat-spreader is more accurately related to the total power of the individual cell. This may be explored in more detail by considering two additional cells, a 1mm² cell operated at 1000x (fig 5-12) and a 0.7mm² cell (fig 5-13) operated at 2000x

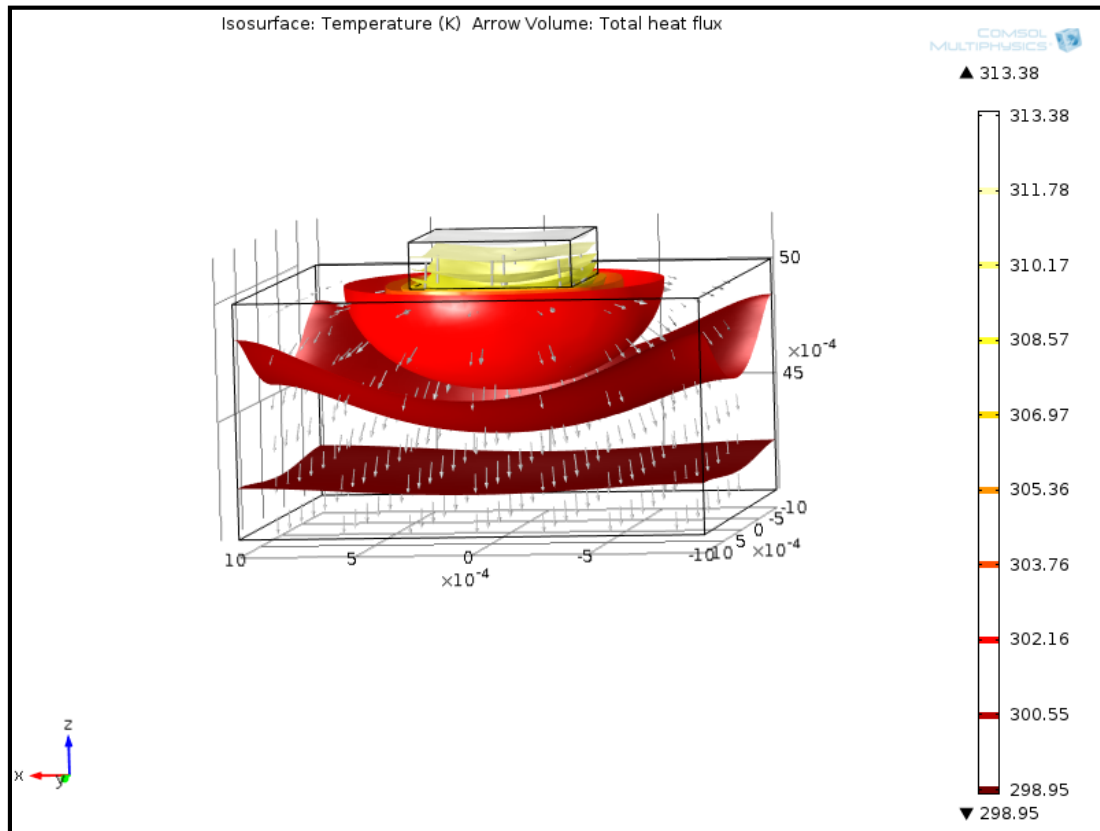


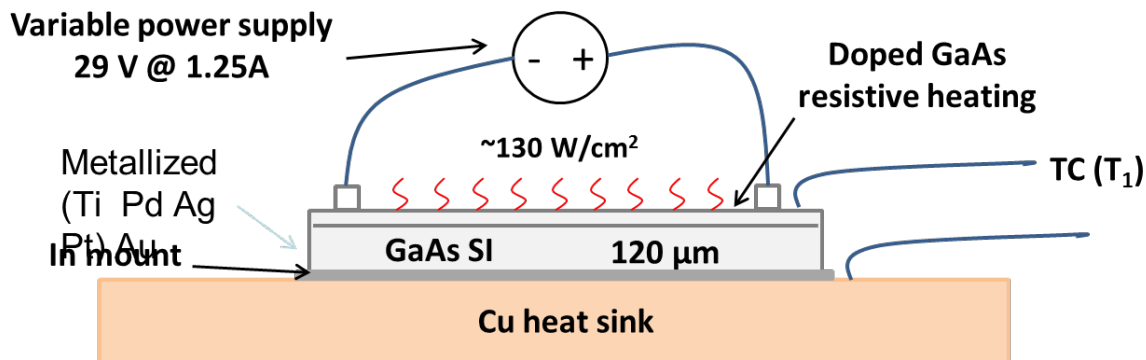
Figure 5-13: 2000x 0.7x0.7 cell 2x2x1mm Al₂O₃ 15 °C rise

Experimental Work: The experimental thermal conductivity measurements previously reported on used a dummy sample fabricated on a 350 μ thick semi-insulating gallium arsenide substrate. Simple calculations indicate that a significant part of the temperature drop (about 10°C) is expected to occur across the gallium arsenide (it has a relatively low thermal conductivity). The commercially available cells typically have a germanium substrate (which has a higher thermal conductivity) and is on the order of 175 μ thick (about 5°C drop). To simulate this, the next round of experiments uses samples on gallium arsenide substrates that are thinned to approximately 100 μ, which should have a thermal conduction similar to that of the commercially available cells. It might be noted that other cells which have been removed from their substrates in the fabrication process (inverted metamorphic, dilute nitride or other epitaxial lift –off

devices) would be expected to have even less thermal resistance if mounted in a comparable manner.

Two wafers containing the heater structure were grown and fabricated. Two structures have been thinned to about 100 μ and are in the process of being mounted in the test apparatus.

**For 2000 suns, $\eta = 35\%$, Heat generation:
 $(100 \text{ mW/cm}^2)(2000)(1-0.35) = 130 \text{ W/cm}^2$**



**• $T_1 - T_2 = 7^\circ\text{C}$
measured**

Figure 5-14 Final test Setup

Our modeling indicates that a receiver substrate of greater thermal conductivity than Al_2O_3 is needed for 2000x operation, however while the initial experiments will utilize copper (and indium solder) which appear to have adequate thermal conductivity, the mismatch of thermal expansion may provide a challenge to the desired cycle life (though the thermal fatigue resistance of indium may be adequate). After the required thermal drops have been achieved attentions will be devoted reliability issues. The thermal expansion coefficients of the projected heat sinks are not as greatly mismatched to those of the semiconductor as is the case in silicon power devices and indium solder may be satisfactory and convenient and has the advantage of having twice the thermal conductivity of gallium. However if it proves necessary adapting the test assembly to liquid metal heat sinking using low melting indium-gallium alloys developed by IBM and

available from Indium Corporation of America should be reasonably straightforward. After developing the thermal dissipation test set-up and if necessary adapting liquid metal contacting of III-V multijunction cells (i.e. Ge substrates) to heat sinks, and confirming performance expected from modeling, we will then concentrate efforts on longer term reliability aspects of the design. Ge has not typically been used for high dissipation devices so barrier layers may be needed (i.e. adapted from Si practices).

We also studied the alternative heat spreaders on heat dissipation and evaluate as to whether a more conductive but higher cost heat spreader is justified; and will investigate the effect of cell size on the temperature gradients.

In Summary

- **Goal : 2000× junction 10°C above 500× baseline or 15 °C above 500× heat sink**
- ***Milestone of 15 °C temperature rise has been met. (~12 °C) Indium solder provides adequate thermal contact. Copper is adequate for heat spreading***
- **Electrical isolation with Al₂O₃ will increase temperature rise(15 °C possible with thin Al₂O₃)**
- **Smaller cells → less temperature rise**
- **Thermal cycling of indium solder 100×**

Section 6: Tunnel junction fabrication and testing at NCSU tasks 1.2 & 4.2

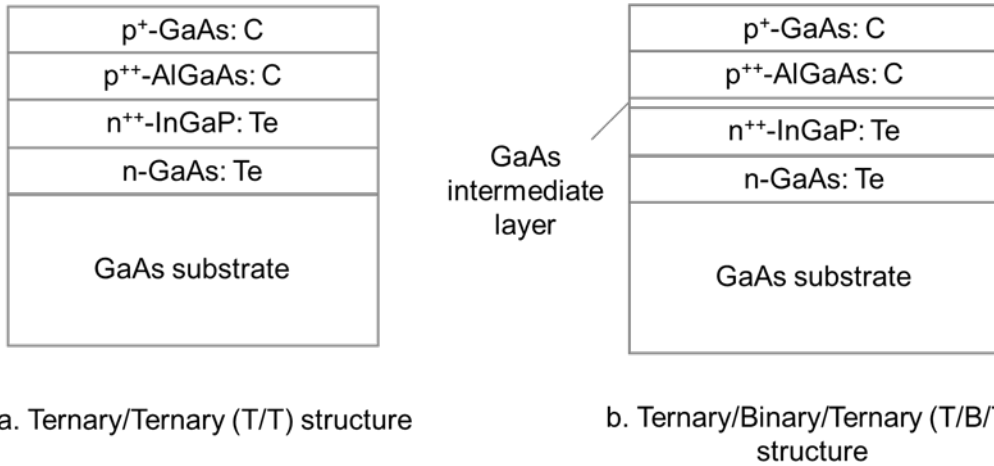


Figure 6-1: Tunnel junction structures a) without and b) with GaAs interfacial layer

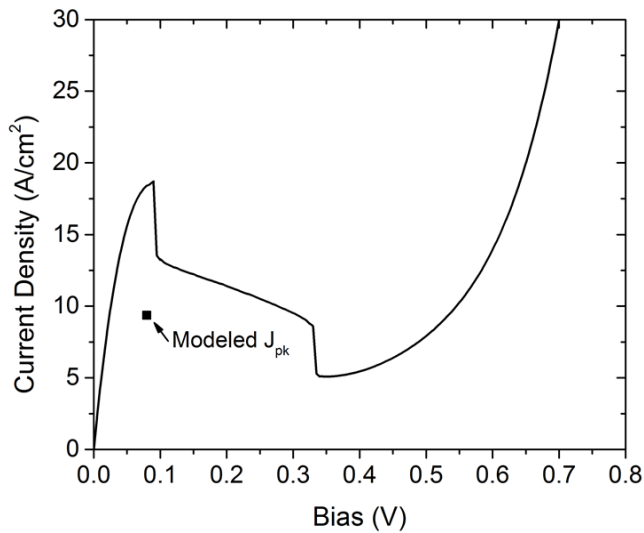


Figure 6-2: InGaP/AlGaAs (T/T) tunnel junction measured J-V characteristic.

While the tunneling current of ~10 amperes is adequate for low concentration it is not sufficient for high concentration 1000x would require 15 amperes plus a safety margin

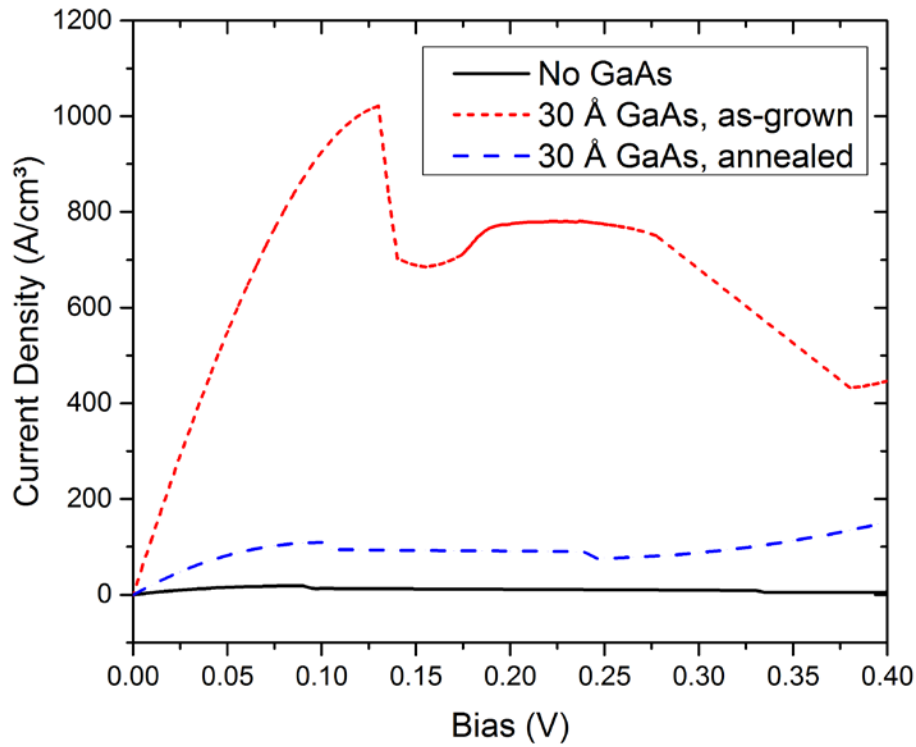


Figure 6-3: J-V characteristics of an InGaP/AlGaAs TJ of Structures A and B

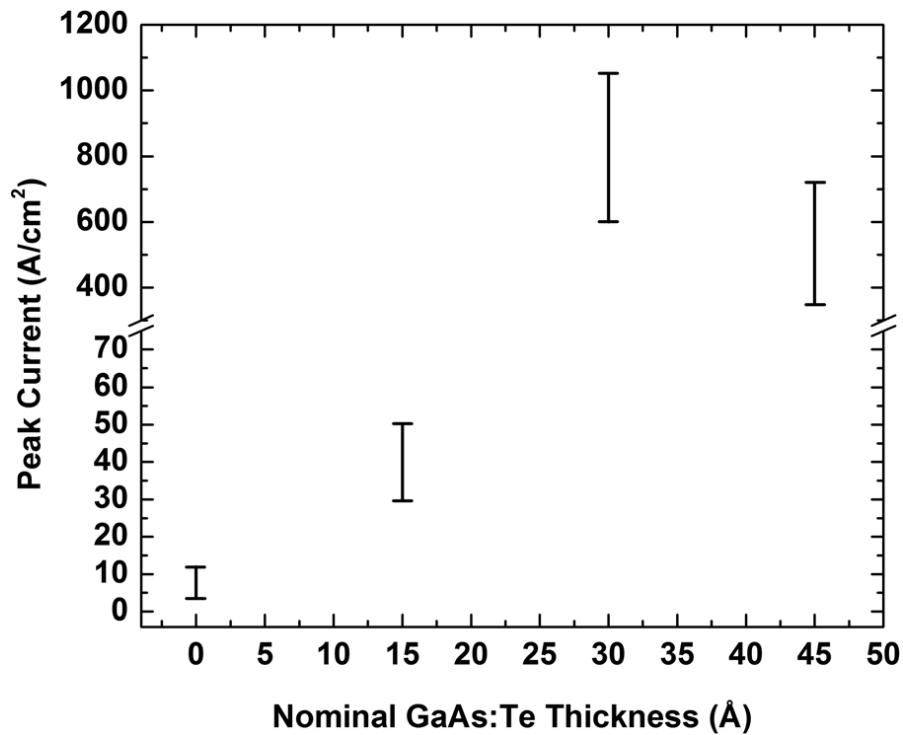


FIG. 6-4. Peak tunneling current range for various $\text{In}_x\text{Ga}_{1-x}\text{P}:\text{Te}/\text{GaAs}:\text{Te}/\text{Al}_{0.6}\text{Ga}_{0.4}\text{As}:\text{C}$ tunnel junction architectures with GaAs:Te interfacial layer thickness ranging from 0 Å to 45 Å

Light Absorption in the GaAs interfacial layer

The introduction of a lower bandgap layer in the tunnel junction structure naturally raises the question of whether there will be enough absorption to significantly compromise the benefits of using a high-bandgap tunnel junction. To answer this question optical the absorption integrated over the appropriate portion of the solar spectrum was calculated for varying thicknesses of GaAs, the results are shown in the following table.

- Table shows effect on J_{sc} and efficiency for a lattice-matched triple junction cell with a J_{sc} of 14.5 A/cm² and an efficiency of 40%
- 1% loss in J_{sc} for each 100 Å of GaAs

GaAs thickness (Å)	J_{sc} (A/cm ²)	Efficiency (%)
0	14.50	40
30	14.46	39.9
50	14.43	39.8
100	14.36	39.6

These calculations indicate that for a 200 Å GaAs layer in a B/T TJ as was used in the Spire record cells, a 40% efficiency cell would be reduced to 39.2% efficiency. This is consistent with previous estimates of the absorption of binary /ternary indicating that typical B/T tunnel junctions have about 1% absolute absorption above that of T/T tunnel junctions. The conclusion is that the thin GaAs will not contribute an unacceptable amount of absorption to the tunnel junction.

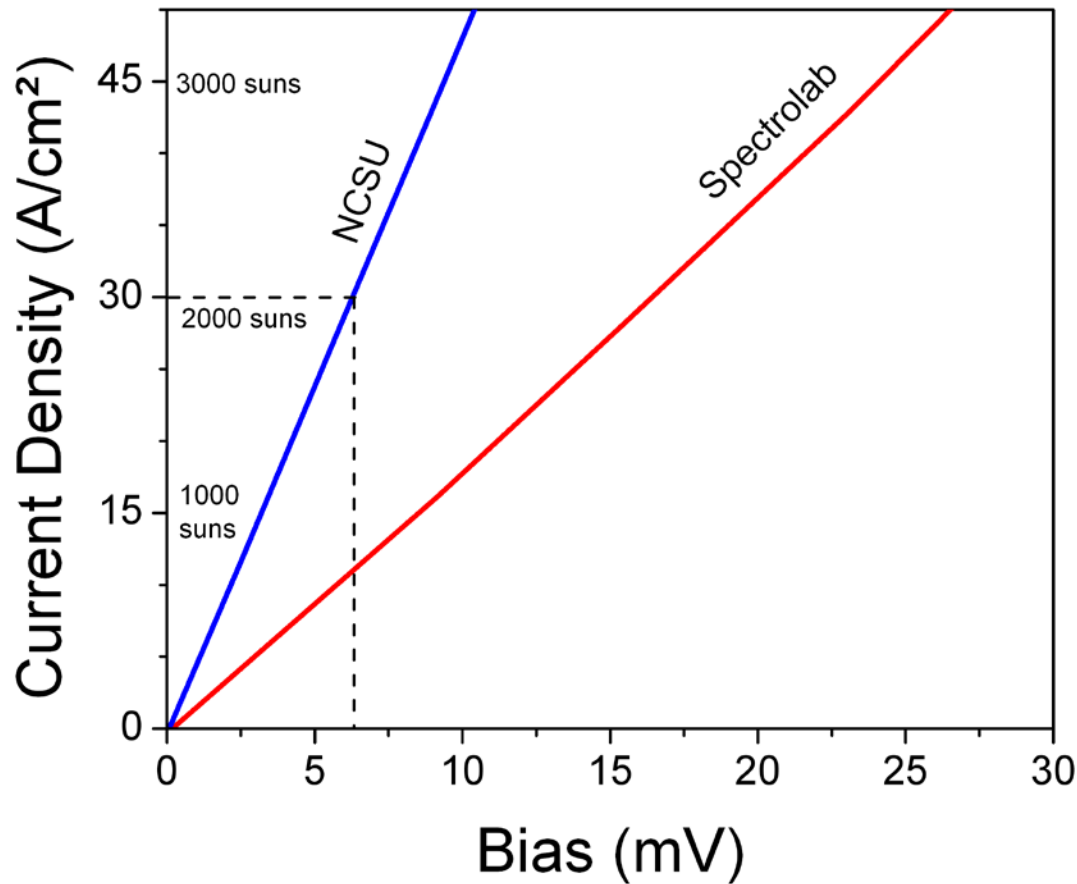


Figure 6-5: Zero bias resistance of NCSU tunnel junction and previous Spectrolab ternary/ternary tunnel junction

It is worth noting that a difference in voltage drop across the tunnel junction of 30 mV will also contribute a relative power loss of 1%, since the typical interlayer is about 1/3 of this, a gain of 10 mV in the resistive voltage drop will compensate for this.

In order to better understand the physics of the tunnel junctions with thin layers and explore further technological developments we have investigated both n and p type interlayers both experimentally and theoretically,

Tunnel junction devices have been grown by MOCVD at 580 °C on GaAs substrates. The TJ structure was composed of 0.2 μm of diethyltellurium (DETe) doped n-type InGaP, 0.2 μm carbon tetrabromide (CBr₄) doped p-type AlGaAs with 10 Å GaAs interfacial layers either n-type and p-type. Devices were made as 360 μm square mesas using standard fabrication techniques. Figure 2 shows that the TJ with the p-type layer has a significantly lower J_{pk} that that with the n-type layer. The reasons for this discrepancy will be discussed in more detail in the next section.

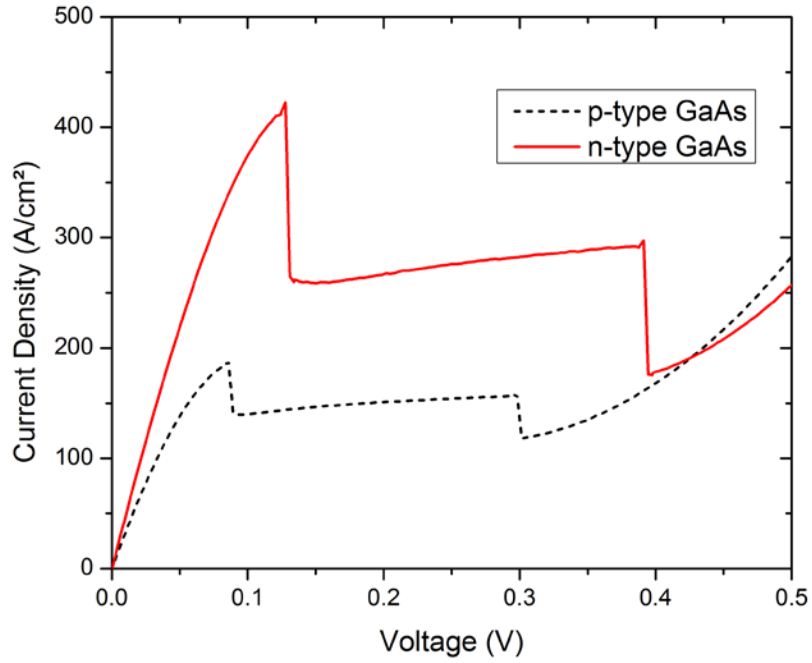


Figure6- 6: j-v of tunnel junctions with n-type and p-type GaAs interfacial layers

Impact of Tellurium doping in InGaP on tunnel junction J-V

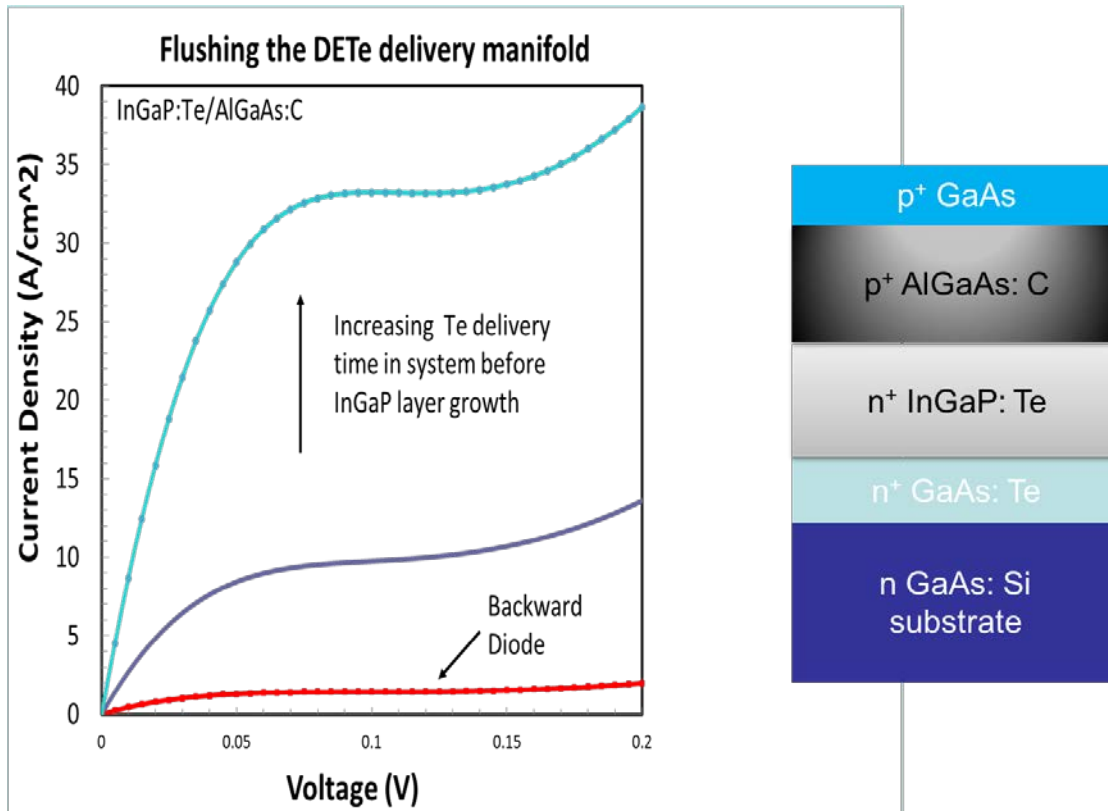


Figure 6-7: Impact of Te source pre-flow time on tunnel junction J-V characteristic.

Details of the tellurium (Te) doping procedure in crystal growth have been found to significantly impact tunnel junction characteristics. Shown in Figure 6, tunneling current density is proportional to the length of time for flushing Te through the delivery manifold prior to growth of the Te doped indium gallium phosphide (InGaP) layer. This feature may be caused in part by the custom design of our laboratory growth system. Notably, the Te source “bubbler” and delivery manifold components, added for expanded capacity to our reactor, are externally located. This configuration has a longer delivery line, and when combined with a relatively low molar flow rate required for the Te source, sets a finite time to fully reach steady state delivery conditions. For ensuring consistency, growth procedures include sufficient pre-flowing (more than three line-volume exchanges) of the Te source through the delivery lines at the beginning of each process run.

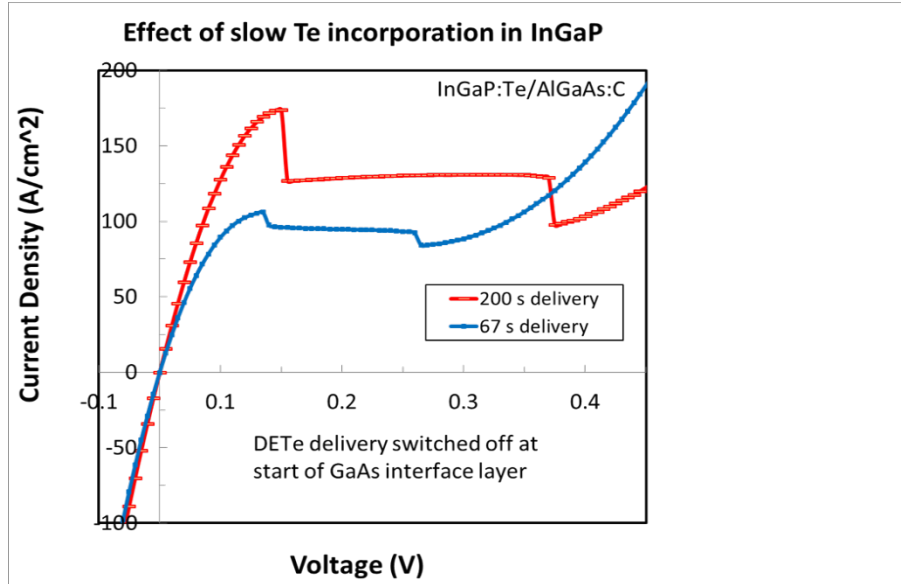


Figure 6-8: Impact of slow Te incorporation in InGaP.

While the flush time may be a peculiarity of the system there are other unique features in the Te doping of InGaP. For a given, consistent Te flow rate, there appears to be a time delay before achieving a full doping level in InGaP layers. This characteristic is distinct from the previously discussed effects for pre-flushing times of Te source into the system. In figure 7, the current density is plotted as a function of voltage for tunnel junction devices grown with different Te delivery times in the InGaP layer. For the 200 second delivery time sample, higher tunneling current density indicates a higher effective doping level at the junction. Note that the total time that Te flows into the system is identical for both samples; in the case of 67 second delivery sample, 133 seconds of doped gallium arsenide growth was added prior to growth of the InGaP layer. It thus appears that there is a surface segregation of Te in the growth of InGaP which is not present in the case of the growth of gallium arsenide. Since there is clearly a delay effect in Te doping (probably due to surface accumulation) it seemed advisable to explore the turn-off as well as the turn-on. When this was done we found a second strong effect (second to the introduction of the GaAs layer). We found that a judiciously chosen early cut-off of the Te doping dramatically increased the peak tunneling current, this is shown in figure 10.

Structure A:
an n-InGaP/p-AlGaAs TJ

Structure B:
an n-InGaP/GaAs/p-AlGaAs TJ

Structure C: Same as Structure B
with the DeTe shut-off earlier

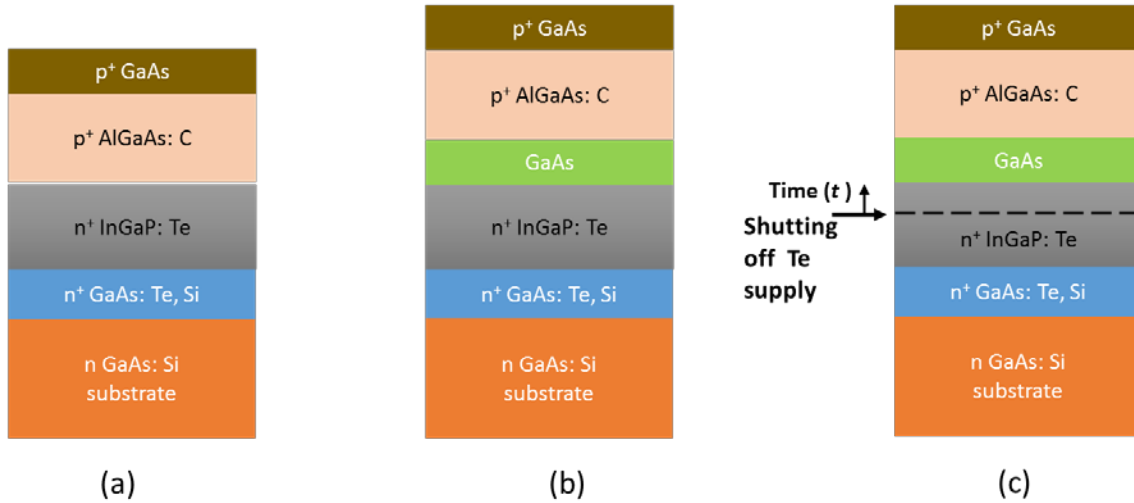


Figure 6-9: Sample Structures, Structures B&C are subject of rest of experiments

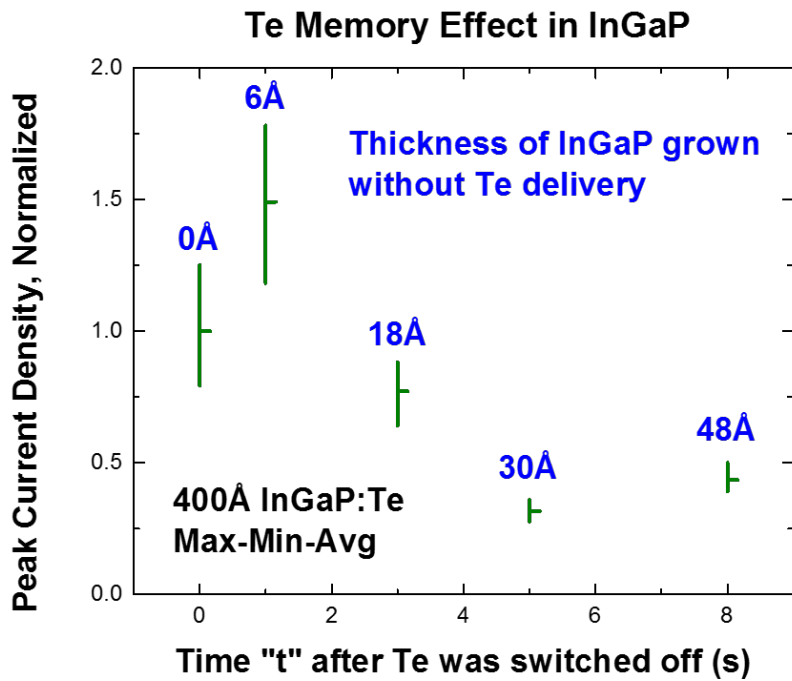


Figure 6-10; Effect of early Te cutoff on unannealed devices

High Growth rate structure

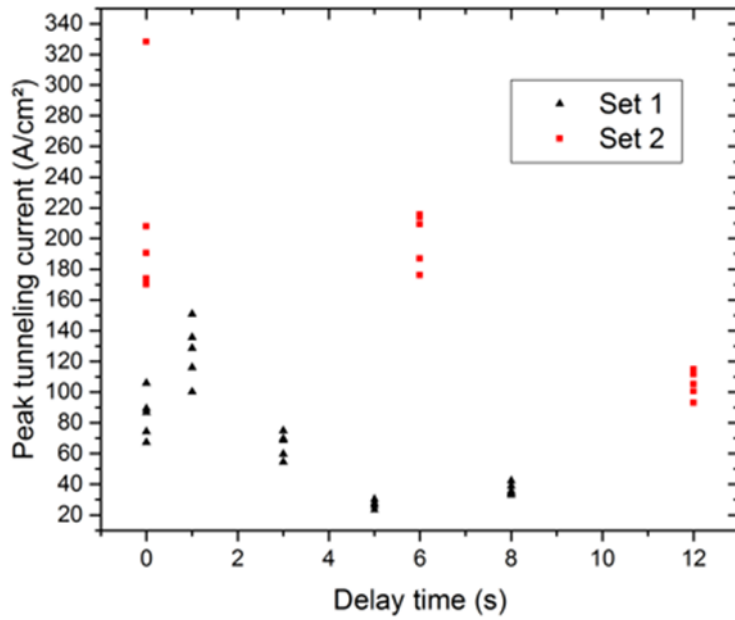


Figure 6-11; Effect of early Te cutoff on additional examples unannealed devices using the relatively high growth rate previously used

Low Growth rate structure

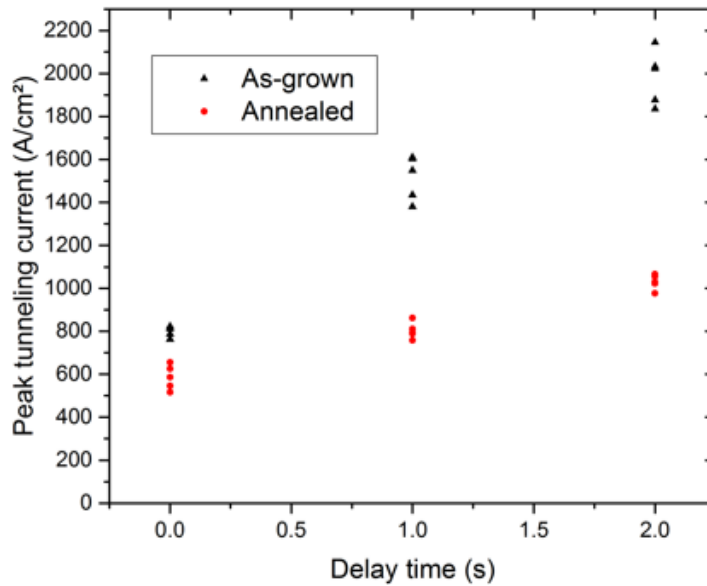


Figure 6-12: Structure C grown at a much lower growth rate annealed and unannealed samples

A summary of the individual experiments on various parts of the test structure is as follows:

- Previous work identified optimum AlGaAs growth conditions.
- Trend: improvement in active carrier concentration by annealing, except for high CBr₄ molar flow.
- Anneal Temp. of 550 °C has greater impact than 450 °C.
- Reduced growth rate for better control of Te to for better control of Te carryover
- Improve doping level in AlGaAs by annealing
- Thicker undoped GaAs 50 Å to reduce Te incorporation in P-AlGaAs
- Earlier shut off of Te source to consume Te hanging around at step edges

The final structure is to be used in a multijunction cell where the growth of the top cell subsequent to the tunnel junction growth means that the annealed tunnel junctions are ultimately the relevant ones. The degradation of the tunnel performance has been an important issue since these tunnel junctions were first developed, figure 11 which is taken from the pioneering work at NCSU illustrates this.

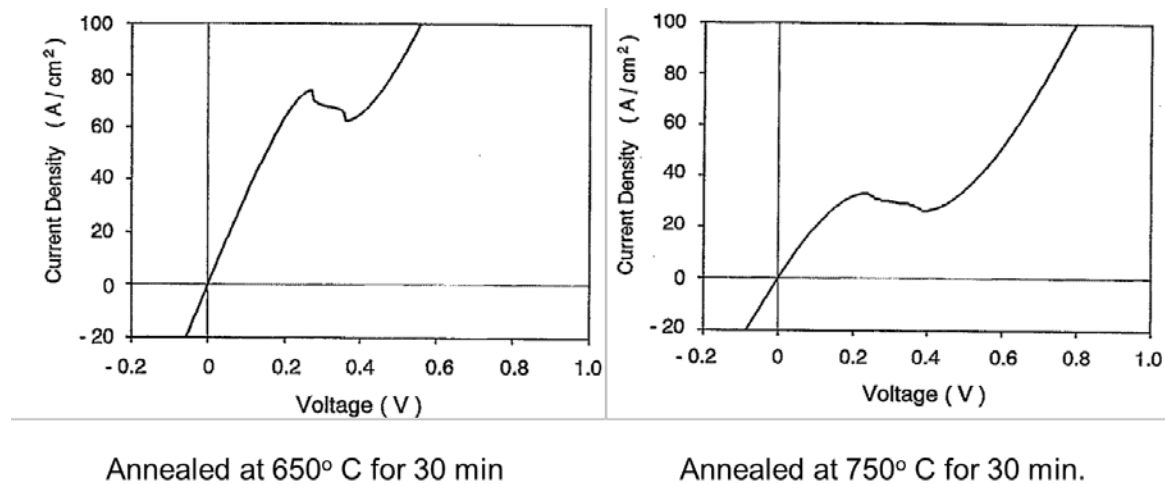


Figure 6-13: Data on early (ALE grown) NCSU tunnel junctions

Since perform of the unannealed structures has been brought to a more than adequate level the rest of the work is focused on the performance of annealed structures. It is fairly well known that extremely high doping concentrations can increase diffusion and thus deterioration when annealed, this is expected to be particularly important at the junction. For this reason *the test device structure for rest of study is 9(c)*

When the optimized modified growth scheme was applied to whole structure illustrated in figure 9(c).

The following characteristics were achieved:

- InGaP doping of $1.4 \times 10^{-19} \text{ cm}^{-3}$, AlGaAs doping of $7 \times 10^{-19} \text{ cm}^{-3}$.

The modified growth procedure was applied to samples grown with Te cutoff of one and two seconds before the end of the InGaP growth and the resulting devices were measured under two conditions.

- Unannealed sample grown under modified conditions
- Annealing at $650 \text{ }^\circ\text{C}$ to simulate the growth of the top cell

The results are shown in figures 14. While all the results are good, the results on the annealed samples with the two second delay are record setting. It is particularly noteworthy and encouraging that we had to modify our electrical test setup to accurately measure the high tunneling currents achieved

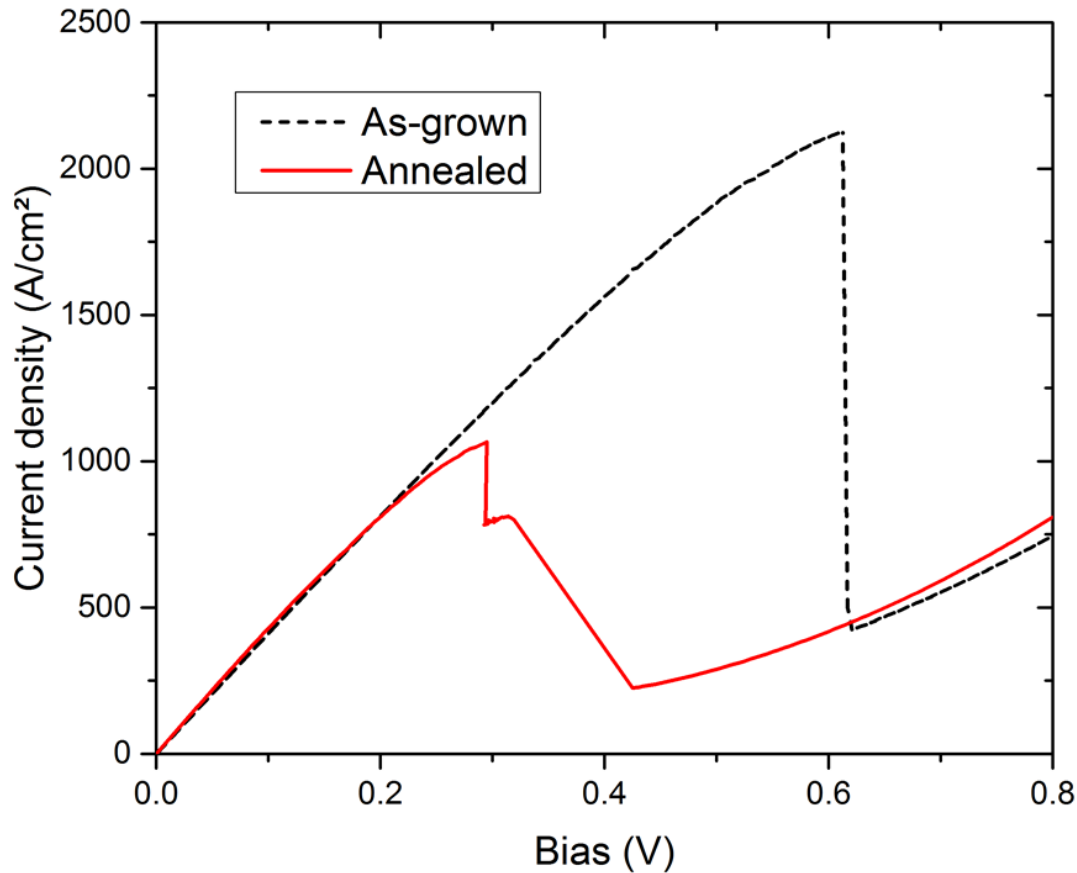


Figure 6-14: Tunnel junction with optimized conditions and Te cutoff two seconds early measured with improved setup

Explanation of effect of early Te cutoff on (structure C) devices

The best explanation for these results is the relatively large surface accumulation of Te during the growth of Te doped InGaP, this effect is illustrated in figure 15 Further work along this line showed variable results as shown in Figure 16

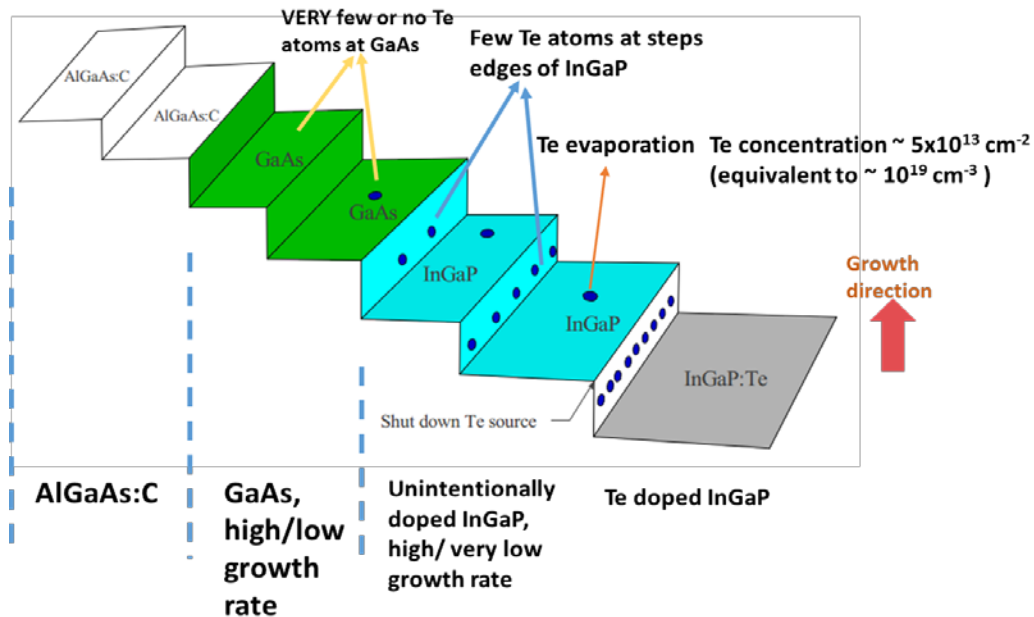


Figure 6-15: Model of tellurium incorporation

When it became that the Te carryover was important but difficult to control, the growth rate was reduced to get better control; additionally modeling of the effect of dopant concentration was in the interlayerundertaken. This took into consideration that Te incorporates into GaAs more easily than InGaP. The experimental results had shown that excessive Te concentration in the GaAs hurt performance the first suspicion was that the Te was getting into the AlGaAs, however the detailed modeling using a numerical solution of the Esaki equation showed that there were other effects related to possible 2-D electron gas effects in the GaAs well (illustrated schematically in figure 16&17, the modeled effect of the carrier concentration in the GaAs layer is shown in figure 18.

Structure C:
Same as Structure B with the DeTe shut-off earlier

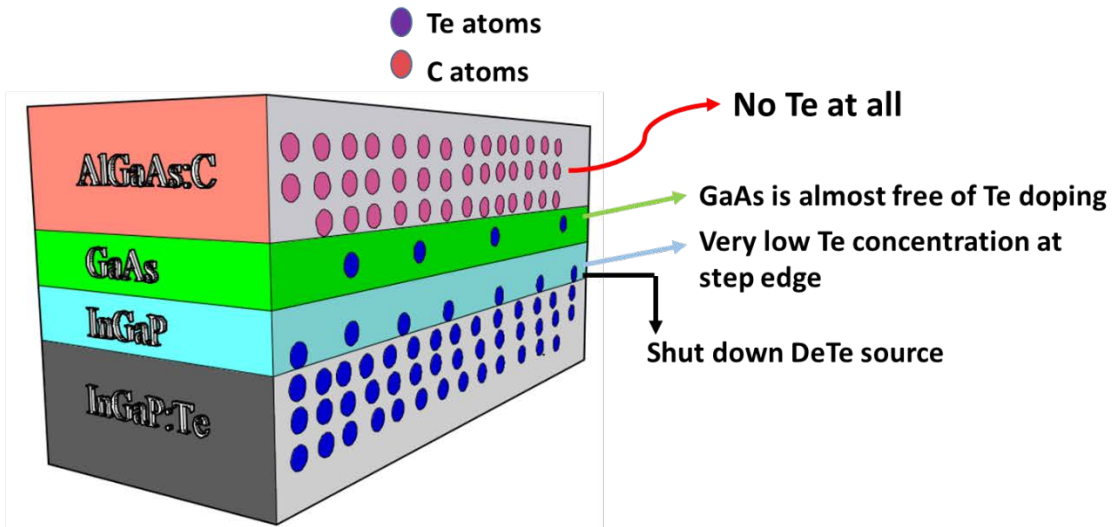


Figure 6-16: Schematic of resulting structure

2D Electron and holes Gas Model

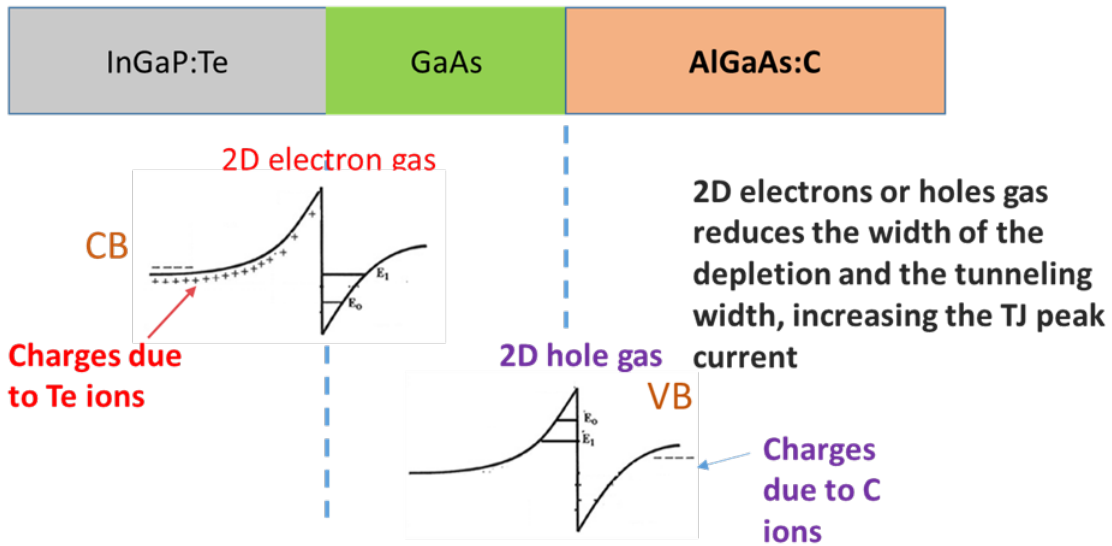


Figure 6-17: Two dimensional model

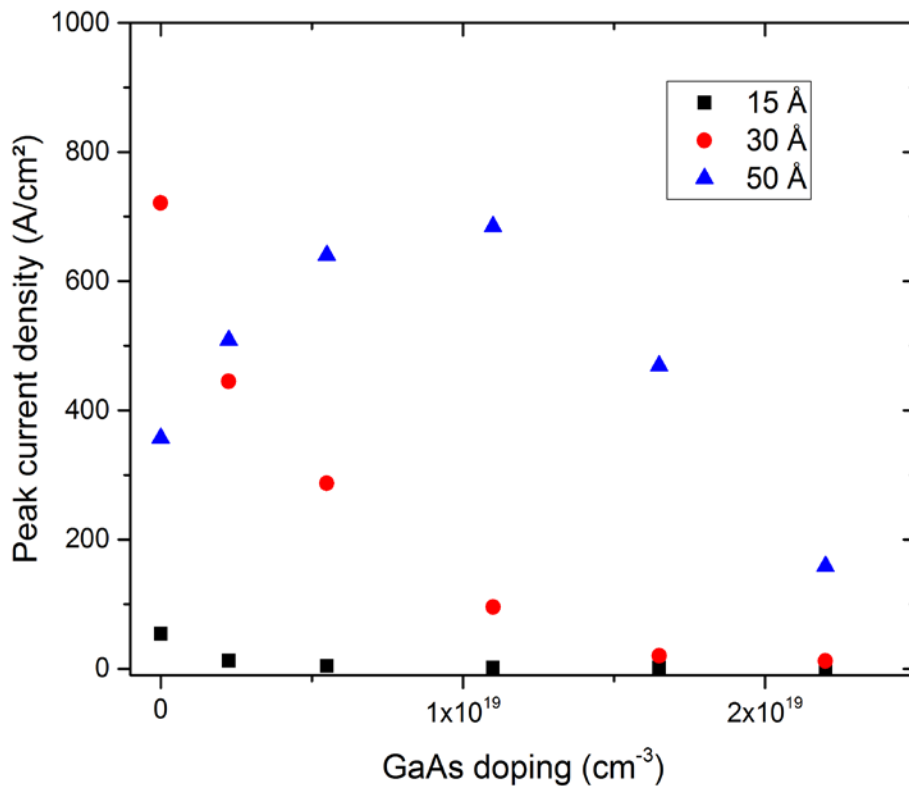


Figure 6-18: Modeled J_{pk} of an InGaP/GaAs/AlGaAs TJ as a function of GaAs doping level and thickness. Need to reduce the background doping in the GaAs QW, with thickness at least 50 Å.

To provide better control over the doping of the GaAs interface layer, structures were grown with a lower growth rate. When this was done the effect of the earlier Te cutoff became more stable.

Summary of Achievements – SOPO Technical Work Plan

Subtask 4.1: Model I-V characteristics of tunnel junctions and diffusion barriers

- Our modeling has elucidated the role of carried-over Te in the GaAs interface layer and we are preparing an additional publication on this

Subtask 4.2: Diffusion barriers for tunnel junctions annealed

Summarizing the accomplishments of the tunnel junction growth portion of this program

- Two world records were broken during this program

1) As grown Tunnel junction:

Promised peak current of 60 A/cm²

Achieved 2000 A/cm² (world record)

We beat our 2013 record of 1000 A/cm² [1] and SPL data of 637 A/cm²

2) Annealed Tunnel junction:

Promised 40 A/cm²

Achieved 1000 A/cm² (world record)

Compared with the Spanish group [2]: 225 A/cm²

This is due to our better understanding of the role of Te at the InGaP interface. Thus the results to date on the annealed tunnel junction show a J_{pk} after annealing that has been improved from 100 A/cm² for our record setting unannealed devices to 1000 A/cm². In comparison, the second best result is 225 A/cm² reported by Algora, et. al.

References:

[1] J. P. Samberg, C. Zachary Carlin, G. K. Bradshaw, P. C. Colter, J. L. Harmon, J. B. Allen, J. R. Hauser and S. M. Bedair. Effect of GaAs interfacial layer on the performance of high bandgap tunnel junctions for multijunction solar cells. *Appl. Phys. Lett.* 103(10), 2013. Available: <http://dx.doi.org/10.1063/1.4819917>. DOI: 10.1063/1.4819917

[2] I. García, I. Rey-Stolle, B. Galiana, C. Algora, "Analysis of tellurium as n-type dopant in GaInP: Doping, diffusion, memory effect and surfactant properties", *J. of Cryst. Growth*, **298**, 794, (2007).

7 Summary of Results achieved for planned tasks

Task	Objective	Goal	State of the Art	Achieved
4.1	As grown TJ	$>60 \text{ A/cm}^2$	637 A/cm^2 (SL)	$>2000 \text{ A/cm}^2$
4.2	Annealed TJ	40 A/cm^2	235 A/cm^2 (UPM)	1000 A/cm^2
5.1	Sheet Resistance	$250 \Omega/\square$	$400 \Omega/\square$ (SL)	$250 \Omega/\square$
5.2	Contact Resistance	$10^{-5} \Omega \cdot \text{cm}^2$	$2 \times 10^{-4} \Omega \cdot \text{cm}^2$ (SL)	$10^{-6} \Omega \cdot \text{cm}^2$
5.3	Fill Factor, Efficiency	ff >0.82 $\eta >40\%$	2000x not used	84% ff @ 2000x η best effort (SPL)
6.1	Head Dissipation	$15 \text{ }^\circ\text{C}$	$7 \text{ }^\circ\text{C}$ @500x (SL)	$12 \text{ }^\circ\text{C}$
7	MJC Structure	$\eta >40\%$	2000x not used	Best effort from SPL

Two world records were broken during this program

1)As grown Tunnel junction:

Promised peak current of 60 A/cm^2 :

Achieved 2000 A/cm^2 (world record)

2)Annealed Tunnel junction:

Promised 40 A/cm^2 :

Achieved 1000 A/cm^2 (world record)

Summary

- Target values for both sheet and contact resistance have been achieved.
- Goal for heat dissipation is met
- Modeling of TJ predicted the improved performance based on the formations of 2D electron/hole gases
- Record performance for :as grown and annealed TJ
- The new TJ technology is transferred and demonstrated at Spectrolab.
- Integrating the new developed technologies to MJ solar cell is achieved.

APPENDIX: EMC Abstract

Potential and issues in MJ solar cells operating at 2000x solar concentration

P .C. Colter, J. L. Harmon, J.R. Hauser and S. M. Bedair

pccolter@ncsu.edu North Carolina State University

The recently announced “Sunshot” initiative with a goal of reducing the cost of photovoltaic systems to \$1.00/W and modules to \$0.50/W has promoted an increased interest in concentrator systems. The higher efficiency of multijunction concentrator systems (~30%) will alleviate the cost pressures of area related material costs. Historically the costs of concentrator cells have been a minor part of the system cost. As the industry’s current trajectory takes it towards a \$ 1.00/W module cost, a move to 1000x suns solar concentration allows ~ \$0.20 /W cell cost to realized; this will keep the cells to a minor part of the system cost. However the “Sunshot” initiative has an objective of \$0.50/W module cost which will require a significantly cheaper cell.

Operating under ultrahigh solar concentration (2000x) is an attractive approach for meeting the challenge of roughly halving the cell cost, keeping it as the same fraction of the total photovoltaic system. Analysis of practical multijunction cells operating above 1000 sun concentrations shows specific resistance of the high bandgap interconnecting tunnel junction to become one of the critically limiting factors to acceptable conversion efficiencies.

I-V data previously reported for an as-grown high bandgap InGaP/AlGaAs tunnel junction device demonstrates super-satisfactory tunnel junction performance under ultrahigh solar concentration can be readily achieved (peak current density >80A/cm² and at ~30A/cm², a ~31mV bias for a specific resistivity of ~1mΩ.cm²). Unfortunately, annealing the tunnel junction, which occurs during subsequent cell growth for completing the multijunction cell structure, degrades tunnel junction performance characteristics significantly.

Analysis of device I-V data for high bandgap tunnel junctions is reported providing estimates of contributions to the total current for operating conditions near-zero bias (i.e. normal operation for multijunction solar cell interconnecting diodes). Impurity diffusion, carrier tunneling, and carrier diffusion are theoretically modeled to qualify annealing impacts on the relative contributions to total current by band-to-band tunneling current (the classical tunnel diode mechanism), thermal diffusion current, and excess current. The excess current (trap related) is shown to be relatively more important in InGaP/AlGaAs structures than in GaAs-GaAs tunnel junctions.

Impurity diffusion during annealing has been well known to significantly reduce junction abruptness and dominate degradation of performance for band-to-band tunneling in high bandgap tunnel junctions, thus potentially contributing currents (i.e. due to tunneling through trap states) were neglected during previous studies. In this analysis, excess current is shown to be a significant portion of the total current in as-grown structures, and important in the performance degradation during annealing. The implications for multijunction cell fabrication will be discussed.

Effect of GaAs interfacial layer on the performance of high bandgap tunnel junctions for multijunction solar cells

Joshua P. Samberg,¹ C. Zachary Carlin,² Geoff K. Bradshaw,² Peter C. Colter,² Jeffrey L. Harmon,² J. B. Allen,¹ John R. Hauser,² and S. M. Bedair²

¹Materials Science and Engineering, North Carolina State University, Raleigh, North Carolina, 27695, USA

²Electrical and Computer Engineering, North Carolina State University, Raleigh, North Carolina, 27695, USA

(Received 1 August 2013; accepted 16 August 2013; published online 5 September 2013)

The effect of the heterojunction interface on the performance of high bandgap $\text{In}_x\text{Ga}_{1-x}\text{P:Te}/\text{Al}_{0.6}\text{Ga}_{0.4}\text{As:C}$ tunnel junctions (TJs) was investigated. The insertion of 30 Å of GaAs:Te at the junction interface resulted in a peak current of 1000 A/cm² and a voltage drop of ~3 mV for 30 A/cm² (2000× concentration). The presence of this GaAs interfacial layer also improved the uniformity across the wafer. Modeling results are consistent with experimental data and were used to explain the observed enhancement in TJ performance. This architecture could be used within multijunction solar cells to extend the range of usable solar concentration with minimal voltage drop. © 2013 AIP Publishing LLC. [<http://dx.doi.org/10.1063/1.4819917>]

Concentrator photovoltaics (CPV) have generated considerable interest as a means of achieving high efficiency, potentially reducing the levelized cost of PV generated energy. Both open-circuit voltage and short-circuit current increase under increasing solar concentration. However, the fill factor (FF) decreases at very high solar concentrations, leading to a reduction in efficiency. The deleterious reduction in FF is caused by an increase in voltage drop across the sheet and contact resistance (R_C) in addition to the voltage drop across the tunnel junction (TJ). For solar concentrations above 1000×, there are several requirements for optimal TJ operation. First, series resistance must be minimized for a low voltage drop; this requires, at the very least, the TJ must have a peak current density (J_p) higher than that generated by the cells at high solar concentration. Second, for optimum efficiency, the TJ must consist of materials with bandgaps at least as high as the active subcell material above it. Third, the dopants used for highly doped layers of the TJ should have very low diffusion coefficients to prevent deterioration of the junction during subsequent growth steps.

The AlGaAs:C/InGaP:(Se or Te) ternary/ternary (T/T) TJ structure for the GaAs/InGaP based multijunction solar cell (MJSC) was first reported in the 1990s.^{1,2} The voltage drop across this TJ at a current density corresponding to a solar concentration of 2000× was approximately 40 mV. For triple junction MJSC structures, the voltage drop across two TJs will be approximately 100 mV. This voltage drop results in a MJSC efficiency reduction of approximately 4% and is a target for further improvements.

The quality of the TJ depends critically on the metallurgical interface quality. For T/T TJs grown by metalorganic chemical vapor deposition (MOCVD), there are several issues that must be addressed to achieve both abrupt compositional and doping transitions at the interface. Because a substantial overpressure of group V precursors is required during growth, compositional abruptness is fairly difficult to achieve in MOCVD when column V precursors need to be switched on and off. For example, it has been recently demonstrated through STEM energy dispersive spectroscopy that switching In off in an InGaAs/GaAsP multiple quantum well

(MQW) structure is fairly abrupt, while switching P off is not.³ This results in P carry-over into the subsequent growth for approximately 30 Å. Thus, it is expected for an abrupt $\text{In}_x\text{Ga}_{1-x}\text{P:Te}/\text{Al}_{0.6}\text{Ga}_{0.4}\text{As:C}$ TJ that P will be present in the $\text{Al}_{0.6}\text{Ga}_{0.4}\text{As:C}$, resulting in a graded alloy composition at the tunnel junction interface. In addition to P carry-over, the termination of the Te doping for the $\text{In}_x\text{Ga}_{1-x}\text{P:Te}$ at the onset of the $\text{Al}_{0.6}\text{Ga}_{0.4}\text{As:C}$ growth is not abrupt due to the memory effect, or surface segregation, of Te, as well as its solubility limit in InGaP.⁴ Thus, grading of both alloy composition and doping are expected in T/T tunnel junctions. This leads to variations in the depletion and tunneling thickness for carriers and will impact both the peak tunneling current (J_p) and the TJ R_S . TJ characteristics across wafers and from wafer-to-wafer show spreads that would affect solar cell efficiencies.⁵ Other researchers have resorted to using the GaAs:n⁺⁺/AlGaAs:p⁺⁺ binary/ternary (B/T) TJ^{5,6} where problems such as column V switching are avoided, yielding better reliability and reproducibility; however, this B/T TJ suffers from the absorption of photons by the low bandgap GaAs:n⁺⁺ layer that reduces the efficiency of the MJSC.^{7,8}

This paper addresses the interface properties of T/T TJs. The effect of an interfacial GaAs layer, which forms a ternary/binary/ternary (T/B/T) structure as shown in Fig. 1, on peak current and voltage drop across the junction has been investigated. We show methods to achieve a very high, more reproducible peak TJ current with properties suitable for solar applications with concentration $\geq 2000\times$. Recently, it has been reported that the addition of a MQW structure at the interface of a TJ lattice matched to InP resulted in the enhancement of J_p . However, it is also accompanied by a 1.7% absorption of the photons in the spectral band of interest.⁹

The TJ structures were grown using a Thomas Swan MOCVD system with a custom built, vertical reaction chamber. (100) GaAs:Si 2°→(110) substrates were utilized for all growth. Metalorganic precursors employed included trimethylgallium (TMGa), trimethylindium, trimethylaluminum, tert-butylarsine, tert-butylphosphine (TBP), carbon tetrabromide (CBr₄), diethyltelluride (DETe), and dimethylzinc. The

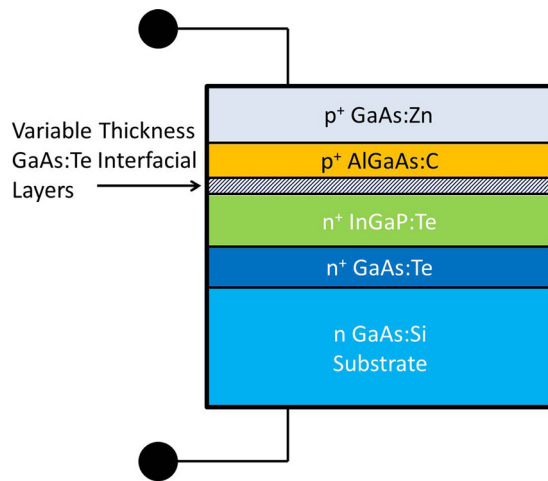


FIG. 1. Schematic of the $\text{In}_x\text{Ga}_{1-x}\text{P:Te}/\text{Al}_{0.6}\text{Ga}_{0.4}\text{As:C}$ tunnel junction.

growth temperature for the $\text{In}_x\text{Ga}_{1-x}\text{P:Te}/\text{Al}_{0.6}\text{Ga}_{0.4}\text{As:C}$ TJ was chosen to produce both high quality material and adequate doping levels for both sides of the junction. Utilizing CBr_4 , we found that the $\text{Al}_{0.6}\text{Ga}_{0.4}\text{As:C}$ doping decreased with an increase in growth temperature. The growth optimization for the $\text{Al}_{0.6}\text{Ga}_{0.4}\text{As:C}$ was achieved at 580°C , resulting in a hole doping concentration of $8 \times 10^{19} \text{cm}^{-3}$. The growth of nearly lattice matched $\text{In}_x\text{Ga}_{1-x}\text{P:Te}$, slightly compressive with respect to GaAs, was optimized at 580°C . Doping levels of approximately $1.15 \times 10^{19} \text{cm}^{-3}$ were achieved, which is believed to be the saturation limit for Te incorporation in InGaP.⁴ Interfacial layers of GaAs:Te grown at the same DETe and TMGa flow rates produced doping levels of $2 \times 10^{19} \text{cm}^{-3}$.

The TJs were capped with 2200 \AA of GaAs:Zn utilizing doping levels of $\sim 3 \times 10^{19} \text{cm}^{-3}$ to achieve ohmic contacts with low R_C . The composition of the $\text{In}_x\text{Ga}_{1-x}\text{P:Te}$ was adjusted such that the tensile stress in $\text{Al}_{0.6}\text{Ga}_{0.4}\text{As:C}$, due to the carbon doping, was compensated by the compressive stress of the $\text{In}_x\text{Ga}_{1-x}\text{P:Te}$ to achieve an overall slightly compressive TJ pseudomorphic to the GaAs substrate as demonstrated by the XRD image presented in Fig. 2. For convenience, the XRD peaks have been labeled with the layers responsible for them. The thicknesses of the $\text{In}_x\text{Ga}_{1-x}\text{P:Te}$ and $\text{Al}_{0.6}\text{Ga}_{0.4}\text{As:C}$ layers were 1800 \AA and 1200 \AA , respectively, as determined by scanning electron microscopy.

Devices were processed into 0.09 mm^2 mesas using standard lithography processes. Prior to metallization, the

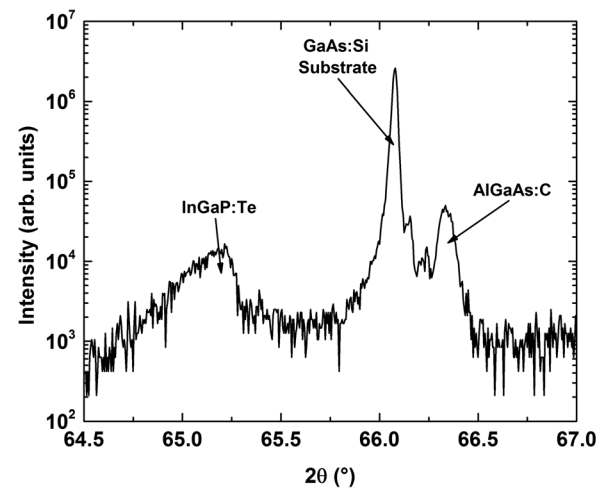


FIG. 2. Typical $\text{In}_x\text{Ga}_{1-x}\text{P:Te}/\text{Al}_{0.6}\text{Ga}_{0.4}\text{As:C}$ tunnel junction XRD showing the compressive and tensile strain of the $\text{In}_x\text{Ga}_{1-x}\text{P:Te}$ and $\text{Al}_{0.6}\text{Ga}_{0.4}\text{As:C}$ layers, respectively.

mesas were adequately etched using the following sequence. After a 30 s HCl dip, the GaAs cap and AlGaAs layers were removed using 3:1:50 $\text{H}_3\text{PO}_4:\text{H}_2\text{O}_2:\text{H}_2\text{O}$ etch with GaInP acting as an etch stop. HCl (30% by vol.) was used to etch InGaP and finally a 1:1:3 $\text{H}_3\text{PO}_4:\text{H}_2\text{O}_2:\text{H}_2\text{O}$ etch was used to etch slightly below the growth. The p-type contacts used consisted of Ti/Pd/Ag/Au annealed at 450°C for 60 s and n-type contacts of Pd/Ge/Ti/Pt/Ag/Au annealed at 300°C for 15 s. The specific contact resistances, measured using transmission line method, for these metallization schemes were $5 \times 10^{-7} \Omega \text{ cm}^2$ and $2 \times 10^{-6} \Omega \text{ cm}^2$ for the p- and n-type contacts, respectively.

We studied the effect of a GaAs:Te interfacial layer at the metallurgical junction of the TJ. Fig. 3 shows the J-V characteristics of (a) an abrupt T/T TJ structure and (b) a T/B/T TJ architecture with a 30 \AA GaAs:Te interfacial layer. The J_p obtained strongly depends on the thickness of the GaAs intermediate layer and ranges from 12 A/cm^2 for the direct interface to over 1000 A/cm^2 for the thicker GaAs interfacial layer TJs. These results indicate that an abrupt T/T structure is barely suitable for solar concentrations of $1000\times$, whereas the T/B/T structure with a 30 \AA GaAs:Te interfacial layer can accommodate solar concentrations as high as $70\,000\times$, with negligible optical absorption in the 30 \AA GaAs:Te interfacial layer.

The range of peak current (J_p) obtained from three different T/B/T TJs, in addition to the standard T/T TJ, is

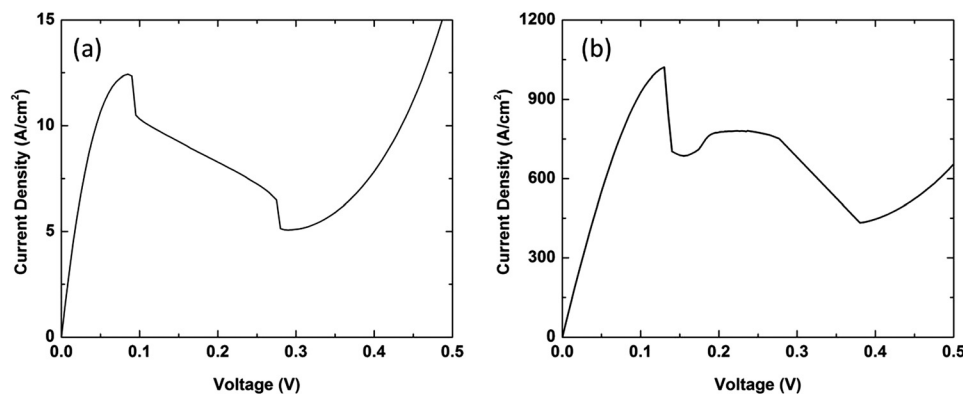


FIG. 3. J-V for (a) $\text{In}_x\text{Ga}_{1-x}\text{P:Te}/\text{Al}_{0.6}\text{Ga}_{0.4}\text{As:C}$ T/T tunnel junction and (b) $\text{In}_x\text{Ga}_{1-x}\text{P:Te}/\text{GaAs:Te}/\text{Al}_{0.6}\text{Ga}_{0.4}\text{As:C}$ T/B/T tunnel junction utilizing a 30 \AA GaAs:Te interfacial layer.

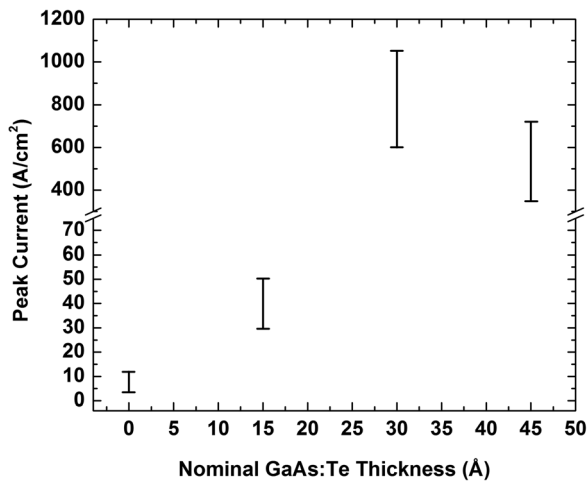


FIG. 4. Peak tunneling current range for various $\text{In}_x\text{Ga}_{1-x}\text{P}:\text{Te}/\text{GaAs}:\text{Te}/\text{Al}_{0.6}\text{Ga}_{0.4}\text{As}:\text{C}$ tunnel junction architectures with GaAs:Te interfacial layer thickness ranging from 0 Å to 45 Å.

presented in Fig. 4. The spread of the data shown in Fig. 4 is due to spatial variation in the J_p across the wafer. For the direct T/T architecture, J_p varies by a factor of three, while J_p of the T/B/T structures with 30 Å GaAs:Te interfacial layers varies by less than a factor two. The primary conclusion of Fig. 4 is the vast improvement of the TJ J_p due to the GaAs:Te interfacial layer.

The achievement of a TJ with J_p of $\sim 1000 \text{ A/cm}^2$ ($\sim 70000\times$) should be viewed purely as an academic achievement. It is not expected that a MJSC will ever operate at such large solar concentrations due to practical limitations such as heat dissipation issues. The practical impact of the current work is to demonstrate that a high bandgap TJ with a thin GaAs:Te intermediate layer will reproducibly achieve a low voltage drop at more reasonable 30 A/cm^2 ($2000\times$ solar concentration). The addition of 30 Å and 45 Å GaAs:Te interfacial layers results in a voltage drop in the range of 2.5–6 mV, respectively, as shown in Figs. 5(a) and 5(b). Additionally, the spread in the voltage drop across a given

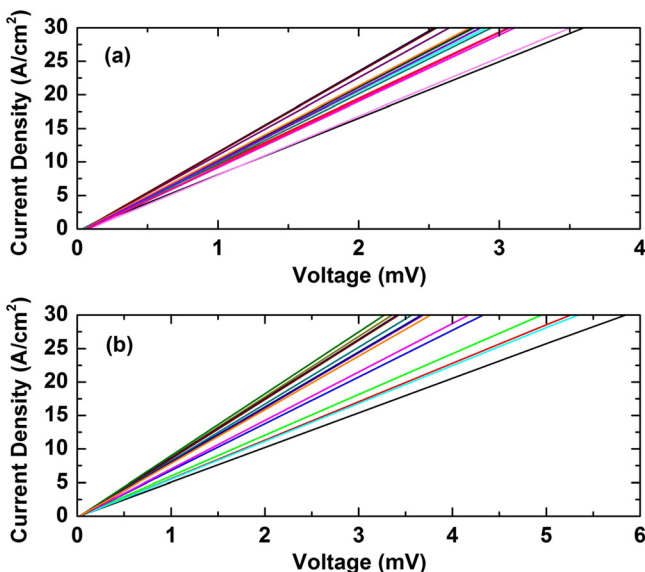


FIG. 5. Voltage drop across the T/B/T TJs at a solar concentration of $2000\times$ for (a) 30 Å GaAs:Te interfacial layers and (b) 45 Å GaAs:Te interfacial layers.

sample for both the 30 Å and 45 Å GaAs:Te interfacial layers is very narrow, on the order of a few mV. Thus, the insertion of the GaAs:Te interfacial layer can allow the MJSC to achieve more reproducible results with variation in efficiency less than 0.2% while retaining the efficiency gains ($\sim 1\%$ absolute) due to the increased transparency of the T/T TJ compared to the B/T TJ. Results shown in Figs. 3(b)–5(b) are superior to the best reported data for high bandgap TJs. For example, Spectrolab reported J_p of 637 A/cm^2 with a voltage drop of 400 mV across the junction.¹⁰

We modeled the behavior of the $\text{In}_x\text{Ga}_{1-x}\text{P}:\text{Te}/\text{Al}_{0.6}\text{Ga}_{0.4}\text{As}:\text{C}$ TJ with and without the GaAs:Te interfacial layer. The peak tunneling current density (J_p) was calculated for both abrupt T/T and T/B/T structures. For modeling purposes, the GaAs:Te interfacial layer thickness was treated as a quantum well with thicknesses of 0–22 Å. The results for thicker GaAs layers are not given because similar results are found for thicknesses above 20 Å. The band structure was determined by obtaining a numerical solution to Poisson's equation while the J_p was predicted using the local tunneling model of Kane,¹¹ which has been previously described.¹² Peak current density was plotted as a function of effective doping density, which is defined as $N_{\text{eff}} = N_a N_d / (N_a + N_d)$, for values ranging from $1 \times 10^{19} \text{ cm}^{-3}$ to $4 \times 10^{19} \text{ cm}^{-3}$, as shown in Fig. 6. The $\text{Al}_{0.6}\text{Ga}_{0.4}\text{As}:\text{C}$ doping level is five times that of the $\text{In}_x\text{Ga}_{1-x}\text{P}:\text{Te}$ doping at each point, which is consistent with the experimentally determined carrier concentrations.

The modeling and experimental results presented in Fig. 6 confirm that the T/B/T TJs have larger J_p than those of the T/T. Because the depletion region of the TJ is only a few nanometers thick, the composition of the interface will have a significant impact on the tunneling characteristics. The presence of GaAs:Te at the interface resulted in a higher J_p due to a lower electron effective mass, and the higher n-type doping in the GaAs relative to the InGaP:Te resulted in thinner depletion regions and a shorter tunneling width. The lower bandgap of the GaAs:Te also resulted in a quantum well structure which reduced the tunneling width. The J_p for the T/B/T TJs was found to be much smaller when the thickness of the GaAs was less than 30 Å, as shown in Fig. 6. This is likely the result of some unintended behavior at the interface. For instance, P carry-over likely occurred when the

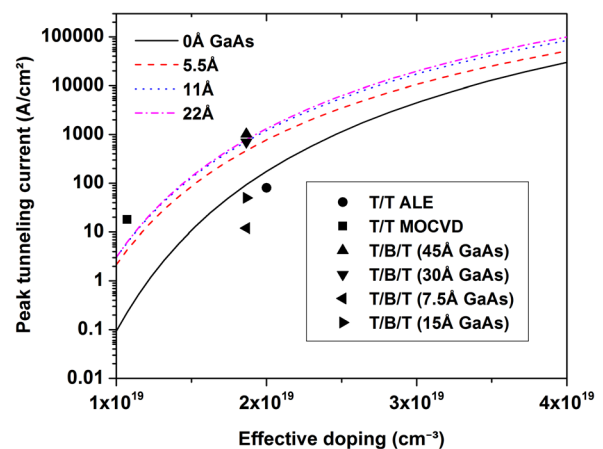


FIG. 6. Modeled peak tunneling current for T/T and T/B/T structures as a function of N_{eff} for different GaAs:Te thicknesses. The results are from the current work shown along with the ALE grown device in Ref. 2.

TBP source was shut off at the end of the $\text{In}_x\text{Ga}_{1-x}\text{P}:\text{Te}$ growth. Thus, an insufficiently thick GaAs:Te interfacial layer in the T/B/T structure may have failed to prevent P carry-over into the AlGaAs:C. Additionally, it is known that GaAs is etched by the CBr_4 precursor used in p-type layers. While the GaAs in the T/B/T structure is doped with Te, the CBr_4 is switched on in the subsequent step, which may have resulted in etching that reduced the thickness of this layer.

Fig. 6 shows that the J_p for the T/T device was higher than the calculated value. This may be due to the InGaP:Te being doped to saturation; the solubility limit for Te in InGaP may have been exceeded in this graded transition region. This could have resulted in the formation of Te based secondary phases. Defect states due to these inclusions in this layer can assist the tunneling process.¹³ Because a local tunneling model was used to calculate J_p , it could not account for potential contributions to the tunneling current through these defects. However, the above model shown in Fig. 6 predicted reasonably well the previously reported J_p for a T/T TJ grown by atomic layer epitaxy (ALE), which gave a J_p of 80 A/cm^2 with effective doping of $2 \times 10^{19} \text{ cm}^{-3}$.^{2,14} In this process, a single atomic layer of InP followed one atomic layer of GaP, grown in a self-limiting process to form InGaP:Se, resulting in an interface between the InGaP and the ALE grown AlGaAs that is atomically abrupt. Because J_p for the ALE grown devices is accurately predicted by the model, it indicates that the discrepancy with the MOCVD grown devices is likely due to some uncharacterized behavior of the interface. It is extremely difficult to find the appropriate analytical tools to investigate the composition, doping, and presence of defects in these MOCVD grown alloy layers, which are only few atomic layers thick. Further investigations of the interface will be necessary to describe its effect on the T/T TJ.

We studied the impact of GaAs:Te interfacial layers on high bandgap InGaP:n⁺⁺/AlGaAs:p⁺⁺ TJ peak current and voltage drop at current densities associated with high solar concentration ($\times \geq 2000$). MOCVD-grown abrupt T/T tunnel junctions are barely suitable for $2000\times$, 30 A/cm^2 applications, and values of J_p vary across and between wafers. Uniformity and J_p are improved when the T/T is replaced by a T/B/T structure. The addition of a GaAs:n⁺⁺ layer with a thickness of about 30 \AA achieved a J_p of 1000 A/cm^2 with only a $\sim 3 \text{ mV}$ voltage drop across the junction at 30 A/cm^2 . This improvement can be explained by the lower electron

effective mass and higher doping in the GaAs. Experimental results compare reasonably with the modeling results. The high tunneling current achieved in these TJ with a voltage drop of only a few mV across the junction can allow MJ solar cells to operate at higher concentrations with little deterioration in fill factor for concentrations up to 2000 suns while retaining the high current provided by the low absorption high bandgap TJ.

We would like to thank the Department of Energy SunShot Initiative (DE-EE0005403) and the National Science Foundation GOALI program (1102060) for financial support of this research.

¹D. Jung, C. A. Parker, J. Ramdani, and S. M. Bedair, *AIP Conf. Proc.* **268**, 338 (1992).

²D. Jung, C. A. Parker, J. Ramdani, and S. M. Bedair, *J. Appl. Phys.* **74**, 2090 (1993).

³J. P. Samberg, H. M. Alipour, G. K. Bradshaw, C. Z. Carlin, P. C. Colter, J. M. LeBeau, N. A. El-Masry, and S. M. Bedair, *Appl. Phys. Lett.* **103**, 071605 (2013).

⁴C. Ebert, Z. Pulwin, D. Byrnes, A. Paranjpe, and W. Zhang, *J. Cryst. Growth* **315**, 61 (2011).

⁵S. Wojtczuk, P. Chiu, X. Zhang, D. Derkacs, C. Harris, D. Pulver, and M. Timmons, in *Proceedings of the 35th IEEE Photovoltaic Specialist Conference* (2010), Vol. 35, p. 1259.

⁶P. Chiu, S. Wojtczuk, X. Zhang, C. Harris, D. Pulver, and M. Timmons, in *Proceedings of the 36th IEEE Photovoltaic Specialist Conference* (2011), Vol. 36, p. 771.

⁷N. H. Karam, R. R. King, M. Haddad, J. H. Ermer, H. Yoon, H. L. Cotal, R. Sudharsanan, J. W. Eldredge, K. Edmondson, D. E. Joslin, D. D. Krut, M. Takahashi, W. Nishikawa, M. Gillanders, J. Granata, P. Herbert, B. T. Cavicchi, and D. R. Lillington, *Sol. Energy Mater. Sol. Cells* **66**, 453 (2001).

⁸R. R. King, N. H. Karam, J. H. Ermer, M. Haddad, P. Colter, T. Isshiki, H. Yoon, H. L. Cotal, D. E. Joslin, D. D. Krut, R. Sudharsanan, K. Edmondson, B. T. Cavicchi, and D. R. Lillington, in *Proceedings of the 25th IEEE Photovoltaic Specialist Conference* (2000), Vol. 25, p. 998.

⁹M. P. Lumb, M. K. Yakes, M. Gonzalez, I. Vurgaftman, C. G. Bailey, R. Hoheisel, and R. J. Walters, *Appl. Phys. Lett.* **100**, 213907 (2012).

¹⁰R. R. King, C. M. Fetzer, P. C. Colter, K. M. Edmondson, J. H. Ermer, H. L. Cotal, H. Yoon, A. P. Stavrides, G. Kinsey, D. D. Krut, and N. H. Karam, in *Proceedings of the 27th IEEE Photovoltaic Specialist Conference* (2002), Vol. 27, p. 776.

¹¹E. O. Kane, *J. Phys. Chem. Solids* **12**, 181 (1960).

¹²J. R. Hauser, Z. Carlin, and S. M. Bedair, *Appl. Phys. Lett.* **97**, 042111 (2010).

¹³J. M. O. Zide, A. Kleinman-Shwarscstein, N. C. Strandwitz, J. D. Zimmerman, T. Steenblock-Smith, A. C. Gossard, A. Forman, A. Ivanovskaya, and G. D. Stucky, *Appl. Phys. Lett.* **88**, 162103 (2006).

¹⁴M. A. Tischler and S. M. Bedair, *J. Cryst. Growth* **77**, 89 (1986).

Modeling an InGaP/AlGaAs tunnel junction containing an AlAs diffusion barrier

John Hauser, Zachary Carlin, Jeff Harmon, Geoffrey Bradshaw, Joshua Samberg, Peter Colter and Salah Bedair

North Carolina State University, Raleigh, North Carolina, 27695, United States

Abstract — Cost improvements in concentrated photovoltaic (CPV) systems can be achieved by operating at increased solar concentration. Current multijunction CPV systems are limited to about 1000× concentration by the performance of the tunnel junctions (TJ) which connect the subcells. The TJ requires materials which are doped in excess of 10^{19} cm⁻³ in order to operate effectively, and so are susceptible to diffusion during the growth of subsequent layers. This paper considers a tunnel junction comprised of tellurium doped n⁺-InGaP and carbon doped p⁺-AlGaAs with a several monolayers of AlAs at the interface. The diffusion profile of the dopants was found and used to calculate the tunneling current through a junction. Due to uncertainty in the diffusion constants of C and Te in the three layers, the tunneling current was calculated for several values of Dt. The diffusion constant ratio in the AlAs was taken as a fraction of the diffusion constant in the other two layers. A significant increase in peak tunneling current was seen for Dt > 1×10^{-14} cm² when a three monolayer thick AlAs barrier was present.

Index Terms — tunneling, semiconductor device modeling, photovoltaic systems

I. INTRODUCTION

Solar cell driven cost reduction in concentrated photovoltaic (CPV) systems can be achieved by a combination of three efforts: 1) the improvement of cell efficiency 2) the reduction of cell cost per unit area (\$/cm²) and 3) reduction in cell cost (\$/W) by increased concentration. Terrestrial systems equipped with multijunction (MJ) solar cells typically limited solar concentrations between 500× and 1000× [1]. For a given MJ structure an increase in solar concentration will result in both cost reduction and an improvement in conversion efficiency

Solar cell efficiency is a function of short circuit current (I_{sc}), open circuit voltage (V_{oc}) and fill factor (FF). I_{sc} scales linearly with concentration, while V_{oc} increases logarithmically with optical current. The FF of an ideal solar cell also increases with solar concentration; however, parasitic effects cause the FF to become the limiting parameter at very high concentrations. The two primary factors that limit the maximum concentration in MJ cells are increased losses due to series resistance and degradation in electrical characteristics of the tunnel junctions (TJ) connecting each subcell. The second limitation is the most critical since the cell efficiency will decrease rapidly when peak tunneling current (J_p) is exceeded, while losses due to series resistance increase more gradually at higher concentrations.

For effective tunneling, the TJ must be doped in excess of 10^{19} cm⁻³. As a result, the peak current density of a triple junction photovoltaic cell is limited by the high bandgap p⁺-AlGaAs/n⁺-InGaP TJ between the top and middle cells, since it is more difficult to achieve high doping levels in these materials, particularly n-type InGaP [2]. It is possible to use a p⁺-AlGaAs/n⁺-GaAs junction, but this will result in efficiency losses due to absorption in the GaAs layer. Additionally, the performance of TJ can be degraded by a decrease in net doping due to compensation from diffused dopants from the adjacent layer. When the top cell is grown at temperatures between 650 °C and 700 °C, dopants will diffuse between layers, as seen in figure 1, creating a non-abrupt interface at the junction, which lowers the net doping at the junction and

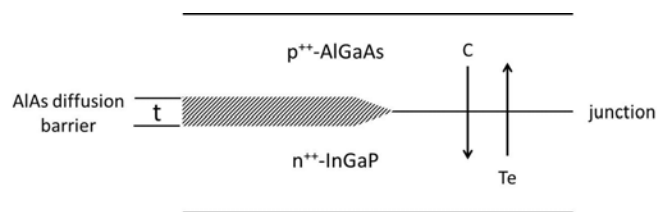


Fig. 1: Schematic of an InGaP/AlGaAs TJ showing the addition of an AlAs diffusion barriers.

leads to a reduction in J_p . For very thin AlGaAs and InGaP layers a decrease in J_p can also occur when carriers diffuse outwards from the highly doped regions. The as-grown (p⁺-AlGaAs/n⁺-InGaP) TJs offer a 20 meV voltage drop at 1000×, as was previously reported [2]. However, exposing this TJ to high temperatures during the growth of high bandgap cells causes the voltage to increase to ~60 meV. In the worst case scenario, a four junction cell, the total drop across three TJ can reach 200 mV which results in an 8-12% drop in efficiency. It is necessary to limit this diffusion in order to maximize the potential of the AlGaAs/n⁺-InGaP TJ. This paper will discuss the use of AlAs at the p⁺-n⁺ junction boundary, which has been found to reduce the diffusion of Zn [3].

In this work, we will build upon previous work [4] with the InGaP/AlGaAs TJ and apply the tunneling model to a much broader range of applications. We will report on the modeling of tunnel junction structures with carbon doped n-type In_{0.49}Ga_{0.51}P and tellurium doped p-type Al_{0.36}Ga_{0.64}As. The effect of diffusion barriers made of AlAs at the junction and outside the InGaP/AlGaAs layers will be modeled in order design device structures that will maximize J_p . The AlAs is

expected lower the diffusion constant of Te and C at the junction boundary for two reasons. First, diffusion is generally lower in high melting point materials. Second, diffusion is lower in compressively strained materials, which would include moderately doped AIAs [5]. The result of this lower diffusion is a higher J_p for annealed TJs with a barrier relative to devices without a barrier.

III. MODELING

The model for heterojunction tunnel junctions has been previously described in detail [4]. A numerical solution was found for the diffusion of both dopants by solving the nonlinear diffusion equation with a non-uniform diffusion constant. The initial dopant concentrations before diffusion were taken to be $N_a=1.2 \times 10^{20} \text{ cm}^{-3}$ in the AlGaAs and $N_d=2.4 \times 10^{19} \text{ cm}^{-3}$ in the InGaP. Both materials have a band gap of 1.91 eV at the given compositions with the AlGaAs band being offset 0.2 eV higher. Poisson's equation was used to find the band structure, taking into account the degenerate doping, band gap narrowing due to the high doping levels and the band offset at the InGaP-AlGaAs interface. This band offset had been previously shown to give an improvement in J_p compared to junctions with the same band gap but without the offset. The tunneling current was then calculated at forward bias using the tunneling theory of Keldysh and Kane.

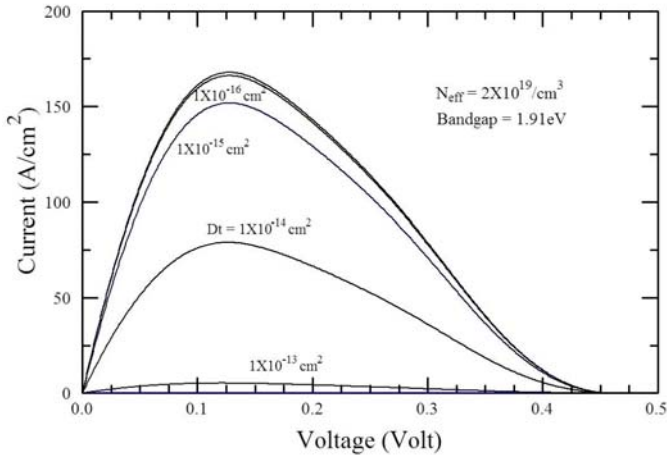


Fig. 2: Peak current density dependence for different heating condition values represented by Dt.

Due to the exponential dependence of tunneling current on tunneling length, small changes in the band structure can have a large impact on the tunneling current. Since a decrease in TJ performance is observed after annealing, it is important to include the impact of dopant diffusion for any model of the TJ performance. Typically, the magnitude of diffusion is stated in terms of Dt, where D is the temperature dependent diffusion constant for a particular atom in a material and t is the time that the diffusion takes place. The effect of higher values of Dt can be seen in figure 2 which shows a

large decrease in peak current with increasing values of Dt due to diffusion at the junctions. The diffusion constant of Te and C in GaAs at 700 °C are $1.3 \times 10^{-17} \text{ cm}^2 \cdot \text{s}$ and $8.2 \times 10^{-17} \text{ cm}^2 \cdot \text{s}$, which for a one hour growth corresponds to a Dt of $4.5 \times 10^{-14} \text{ cm}^2$ and $2.9 \times 10^{-13} \text{ cm}^2$ respectively [6]. Unfortunately, to the authors' knowledge the diffusion constants for Te and Si in AlGaAs and InGaP have not been published. Consequently, the approach used in this discussion is to parameterize Dt from 10^{-18} cm^2 to 10^{-12} cm^2 with the expectation that the actual value will be of the same order of magnitude in the TJ materials as in GaAs. To simplify the calculations the same value of Dt

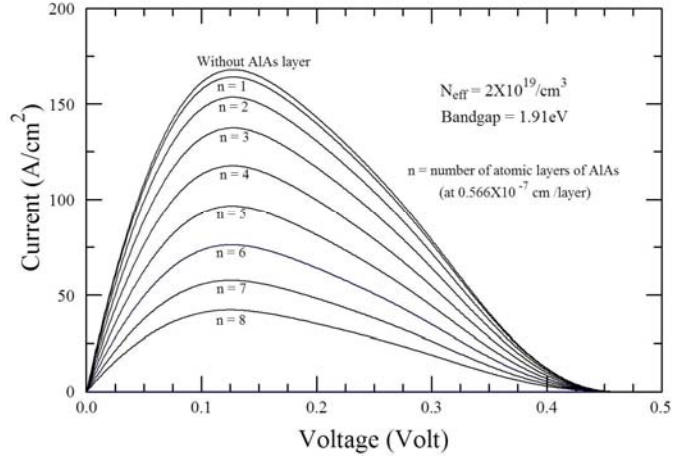


Fig. 3: Tunneling current dependence on AIAs barrier thickness, ignoring the effect of diffusion. AIAs thickness is given in number of monolayers.

was used for InGaP and AlGaAs in each step. Another parameter was the diffusion constant ratio in the AIAs barrier, which was taken as a fraction of the value in the junction layers. This is necessary since it is believed that AIAs will reduce the diffusion constant, but the magnitude of this reduction is unknown.

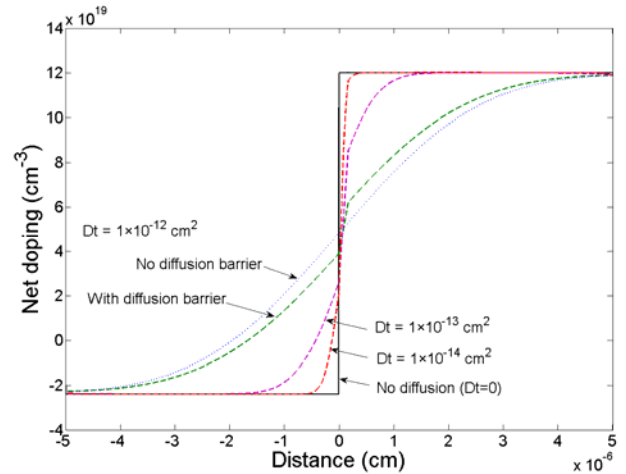


Fig. 4: Diffusion profile with and without AIAs barrier for several values of Dt and a diffusion constant ratio of 0.2.

There were three steps to the modeling process for the junction diffusion barrier. 1) The tunneling current was found for junctions containing AlAs barriers of several thicknesses for abruptly doped junctions. 2) The diffusion profile of the junction was found for one particular barrier thickness and diffusion constant ratio and was compared to the diffused profile of a junction without a barrier and 3) J_p was found for several values of Dt and diffusion constant ratios in order to determine the magnitude of diffusion required to benefit from the diffusion blocking layer.

The first step was to determine the effect of the AlAs thickness on the tunneling current for an abruptly doped junction. For this the tunneling current is found for a structure containing the AlAs barrier while ignoring the effect of dopant diffusion. Figure 3 shows a decrease in J_p with increasing AlAs thickness, given in 1 atomic layer intervals, which is expected since the tunneling thickness increases with increasing barrier thickness. While this AlAs layer is undesirable for the as grown TJ, the thicker barrier devices will show relative improvement once diffusion has been taken into account. However, it is not immediately clear what the ideal thickness for AlAs layer is since the diffusion constant in the junction layers and the diffusion blocking in the barrier are not well quantified. For subsequent calculations the AlAs barrier thickness was assumed to be three monolayers (ML). This thickness was chosen to demonstrate the effect of adding the diffusion barrier; for actual devices this thickness will have to be optimized for the particular growth conditions of the InGaP top cell.

The diffusion profile of both dopants was modeled for three values of Dt , 10^{-12} , 10^{-13} and 10^{-14} cm^2 . Figure 4 shows the dopant profile for these values of Dt and without a diffusion barrier and with a diffusion barrier for a Dt of 10^{-12} cm^2 . The barrier was assumed to give a 5 fold reduction in the diffusion constant relative to the AlGaAs and InGaP layers. It can be seen that the barrier has a significant effect on the diffusion of dopants, especially for the large values of Dt shown in fig. 2.

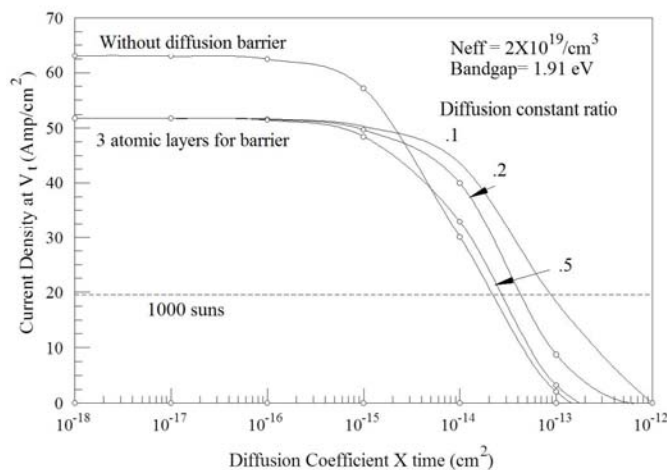


Fig. 5: Peak tunneling current dependence on diffusion constant with and without AlAs layer.

Figure 5 gives the calculated J_p at several values of Dt and a 2, 5 and 10 fold reduction in diffusion through the AlAs layer. When Dt is small the AlAs layer actually reduces performance due to the increased tunneling width. This is consistent with the previous results shown in figure 3. The junction with the diffusion barrier gives a higher J_p when Dt exceeds 10^{-14} cm^2 . For instance, in the case of $Dt=3 \times 10^{-14}$ cm^2 the device without a diffusion barrier will not be adequate for a multijunction cell at 1000 suns, but if the diffusion barrier can provide a reduction in Dt of 0.1 or 0.2, it would perform well enough 1000 sun cell. A similar plot can be made for thicker diffusion barriers. If a thinner barrier were to be used the initial J_p would be closer to that of the barrierless device and it would show superior performance at lower values of Dt . This might be desirable for devices with top cells grown at a lower temperature.

IV. CONCLUSION

The J-V response for an InGaP:Te/AlGaAs:C TJ with $N_d=2.4 \times 10^{19}$ cm^{-3} and $N_a=1.2 \times 10^{20}$ cm^{-3} was modeled to account for the diffusion of dopants at the junction. The parameterization of the diffusion constant was necessary due to the unavailability of diffusion data on Te and C in InGaAs and AlGaAs. An AlAs diffusion barrier of three ML has been found to increase the J_p of an InGaP/AlGaAs when Dt was 10^{-14} cm^2 or higher. Due to the lack of diffusion constants for the junction materials and the barrier, it may be necessary to investigate several barrier thicknesses experimentally. The choice of barrier thickness will also depend upon the growth conditions of subsequent layers. It would be useful to extend these results to tunnel junctions with outer diffusion barriers, especially for a GaAs/AlGaAs structure where thin GaAs layers are desirable.

ACKNOWLEDGEMENTS

The authors would like to thank the U. S. Department of Energy and the National Science Foundation for their financial assistance

REFERENCES

- [1] N. H. Karam, R. A. Sherif, and R. R. S. King, *Concentrator Photovoltaics*, A. Luque and V. Andrejev, Eds., Berlin, Springer 2007.
- [2] D. Jung, C. A. Parker, J. Ramdani, and S. M. Bedair, "AlGaAs/GaInP heterojunction tunnel diode for cascade solar cell application", *J. Appl. Phys.*, vol. 74, pp. 2090, 1993.
- [3] H. Sugiura, C. Amano, A. Yamamoto, and M. Yamaguchi, "Double Heterostructure GaAs Tunnel Junction for a AlGaAs/GaAs Tandem Solar Cell", *Japan. J. Appl. Phys.* vol. 27, pp.269-272, 1988.
- [4] J. R. Hauser, C. Z. Carlin and S. M. Bedair, "Modeling of tunnel junctions for high efficiency solar cells", *Appl. Phys. Lett.*, vol. 97, pp. 04211-04213, 2010.

- [5] 19. H. Sugiura, C. Amano, A. Yamamoto and M. Yamaguchi, "Double Heterostructure GaAs Tunnel Junction for a AlGaAs/GaAs Tandem Solar Cell", *Japan. J. Appl. Phys.* vol. 27, pp. 269-272, 1988.
- [6] B. T. Cunningham, L. J. Guido, J. E. Baker, J. S. Major, N. Holonyak, and G. E. Stillman "Carbon diffusion in undoped, n-type, and p-type GaAs" *Appl. Phys. Lett.* vol. 55, pp. 687-689, 1989.